Impacts of Surface Waves on Turbulence in Ocean Surface Boundary Layers: Observations and Scaling

Zhihua Zheng

A dissertation
submitted in partial fulfillment of the
requirements for the degree of

Doctor of Philosophy

University of Washington

2023

Reading Committee:

Ramsey R. Harcourt, Chair

Eric A. D'Asaro

Andrey Shcherbina

Program Authorized to Offer Degree:
School of Oceanography

University of Washington

Abstract

Impacts of Surface Waves on Turbulence in Ocean Surface Boundary Layers: Observations and Scaling

Zhihua Zheng

Chair of the Supervisory Committee:
Dr. Ramsey R. Harcourt
Applied Physics Laboratory, and School of Oceanography

Turbulence in the ocean surface boundary layer (OSBL) drives mixing, brings nutrients from depth, and mediates the air-sea exchange of heat, momentum, and gases and is thus a key player in the weather and climate system. The current generation of global climate models typically have large errors in the predictions of surface ocean properties, such as the mixed layer depth and the sea surface temperature. These errors are potentially caused by an implicit, or incomplete representation of surface wave effects in the OSBL mixing parameterization that is largely based on turbulence scaling relations for the atmospheric boundary layer (ABL) over land. Turbulence driven by the breaking surface waves and Langmuir circulations arising from the interaction between current and surface wave Stokes drift are the two major mechanisms by which the surface waves contribute to vertical mixing. Although progress has been made in quantifying some of their effects on vertical mixing under certain forcing conditions, our understanding of their roles in the vertical mixing process is still far from complete. To address knowledge gaps about the surface wave impacts on turbulence and vertical mixing, this study makes use of measurements collected from a number of locations with distinct forcing conditions and examines them from a scaling perspective. The research is presented in two parts. Part I takes measurements of temperature profile to infer the vertical mixing of heat while part

II concentrates on vertical velocity measurements to diagnose the turbulence intensity.

The first research component of this dissertation (Chapter 2) evaluates the conventional Monin-Obukhov scaling for the mean vertical temperature gradient in surface layers under destabilizing surface buoyancy fluxes and investigates the modifications of the Monin-Obukhov scaling by wave breaking and Langmuir turbulence. Measurements from two mooring sites are compared with predictions from the Monin-Obukhov scaling. The observational data consistently show smaller unstable thermal gradients under weakly destabilizing conditions, indicating stronger vertical mixing of heat. These deviations are discussed in the context of a simplified theoretical framework for boundary layer turbulence to understand the influence of surface wave breaking and Langmuir turbulence on the mean temperature gradient scaling.

The second research component of this dissertation focuses on the scaling of turbulent vertical velocity in both the surface layer (Chapter 3) and the boundary layer (Chapter 4). In both chapters, a large collection of archived Lagrangian float data are used to compare the vertical turbulence kinetic energy (TKE) from a wide variety of aquatic environments to the conventional scaling relations in the ABL. The observational data exhibits substantial variations under similar conditions of wind stress and surface buoyancy flux. These variations cannot be explained by conventional ABL scaling relations and are shown to depend on the surface wave Stokes drift forcing. Additionally, Chapter 3 details the data processing and extends the surface layer scaling of vertical TKE to incorporate the Langmuir turbulence effect. Chapter 4 combines the effect of wind stress, surface buoyancy flux, and Stokes drift to give a generalized scaling of the boundary layer averaged vertical TKE. Chapter 4 also discusses the depth-dependent scaling of vertical TKE and vertical velocity skewness to highlight the importance of Langmuir turbulence in enhancing the vertical turbulence intensity, modifying the vertical mixing length scale, and promoting the vertical transport of TKE.

TABLE OF CONTENTS

LIST OF FIGURES

LIST OF TABLES

ACKNOWLEDGMENTS

This research was funded by the NSF Grants OCE-1558459, OCE-1657676, and the NASA grant 80NSSC18K1499. Additionally, this work would not be possible without the mooring data provided by the Ocean Climate Stations group at the NOAA Pacific Marine Environmental Laboratory and the Upper Ocean Processes group at the Woods Hole Oceanographic Institution, the surface wave data collected by Jim Thomson's group and the Lagrangian float data collected by Eric D'Asaro's group, both at the UW Applied Physics Laboratory.

Many people from the University of Washington have supported me throughout the years. In particular, I thank my advisors Ramsey Harcourt and Eric D'Asaro for their guidance, mentorship, and numerous stimulating conversations. My committee, Mark Warner, Nirnimesh Kumar, and Andrey Shcherbina, all have been excellent in offering advice and encouragement along my path to this point. LuAnne Thompson welcomed me into her group, and this significantly enhanced my experience as a graduate student. I also appreciate the many helpful views and discussions with a number of friends and collaborators in the wider oceanography community.

Chapter 1
INTRODUCTION

1.1 Background

The ocean surface boundary layers (OSBL), in definition, refer to the buffering layers across which the properties of the ocean interior make a transition to satisfy various surface boundary conditions, e.g., stress, heat flux, and freshwater flux. Globally, they are the link between the ocean interior and the atmosphere. Regionally, they also connect to the hydrosphere and cryosphere through rivers; sea ice, and ice shelves (*Fox-Kemper et al.*, 2022). The boundary layers are dynamically active, mediating the exchange of momentum, heat, and biogeochemical tracers (e.g., carbon and oxygen) with the atmosphere. They usually extend over a vertical scale of about $\mathcal{O}(50\text{ m})$, with a characteristic turnover time of minutes to days, yet their variabilities influence a wide range of oceanic motions, including the global thermohaline circulation, and have broader implications for the Earth's climate over long timescales.

The motion of seawater in the OSBL is almost always turbulent. In fact, they probably host the most energetic turbulence in the ocean driven by winds, waves, and buoyancy loss, therefore are an essential component in the global kinetic energy budget (*Ferrari and Wunsch*, 2009). Throughout the layer, vertical fluxes associated with the turbulent flow shape the mean profiles of momentum, temperature, salinity, and other tracers. Conversely, information about the mean profiles offers valuable insights into the vertical mixing process through surface layer similarity relations (*Monin and Obukhov*, 1954) and metrics like the gradient Richardson number and Thorpe scale (*Thorpe*, 2005).

In practice, nearly all ocean general circulation models use a boundary layer parameterization to calculate upper ocean currents and tracer distributions. A variety of boundary

layer parameterizations exist and most of them are based on the principle assumption that the turbulent fluxes are solely determined by the surface fluxes and subsurface profiles of shear and stratification, through similarity scaling relations.

1.2 *Theoretical framework*

1.2.1 *Surface layer scaling*

Immediately abutting the sea surface, viscous forces and the surface details define the roughness sublayer with a typical roughness length z_0 up to $\mathcal{O}(1\text{ m})$, while the large eddies with length scale about the thickness h of the boundary layer dominate the turbulent transport throughout. As h and z_0 are usually sufficiently separated, there exists an intermediate surface layer where $|z|$, the distance from the mean surface, is the only relevant length scale for turbulence, usually evidenced by the peak around wavenumbers of $\mathcal{O}(1/|z|)$ in the horizontal wavenumber spectrum of vertical velocity w (*Wyngaard*, 2010). In practice, this surface layer is traditionally defined as the upper 10∼20% of the OSBL. The stress in the surface layer is almost entirely carried by the turbulence initiated by the surface stress $\boldsymbol{\tau}_w$, hence the friction velocity $u_* = (|\boldsymbol{\tau}_w|/\rho_0)^{\frac{1}{2}}$, where ρ_0 is a reference seawater density, becomes the dimensional forcing that scales turbulent velocity. Because vertical gradients of turbulent fluxes and stress are negligible when expressed in the surface-layer scales (u_*, $|z|$), the surface layer has been termed as the constant-flux layer as well.

The Monin-Obukhov Similarity Theory (MOST) is a generalization of the earlier logarithmic "law of the wall" (*von Kármán*, 1931) that describes the vertical structure of the average near-wall velocity in wall-bounded neutral boundary layers. With the inclusion of buoyancy effects, MOST is better suited for geophysical applications. In the simplest form, it hypothesizes that 3 parameters govern the vertical structure of a quasi-steady, horizontally homogeneous surface layer bounded by a flat surface: the turbulent length scale $|z|$; the turbulent velocity scale u_*; the scale for buoyancy fluctuations b_*, formed

from the surface buoyancy flux $\mathcal{B}_0$ divided by $-u_*$. If the mean horizontal (streamwise) velocity shear $\partial\overline{u}/\partial z$ is the dependent variable of interest, then we have 4 physically relevant parameters with 2 fundamental dimensions (length and time). Applying the Buckingham Pi theorem (*Buckingham*, 1914) gives 2 dimensionless quantities that are functionally related. One is the non-dimensional variable of interest; the other is $|z|/L$, where $L = u_*^2/\kappa b_* = -u_*^3/\kappa\mathcal{B}_0$ is the Obukhov length ($\kappa \simeq 0.4$ is the von Kármán constant). Therefore we have

$$\frac{\partial\overline{u}/\partial z}{u_*/\kappa|z|} = \phi_m\left(\frac{|z|}{L}\right). \tag{1.1}$$

A similar dimensional analysis with explicit buoyancy effects, using surface heat flux $\mathcal{Q}_0$ and salinity flux $\mathcal{S}_0$, renders similar relations for gradients of potential temperature θ and salinity S,

$$\frac{\partial\overline{\theta}/\partial z}{\theta_*/\kappa|z|} = \phi_h\left(\frac{|z|}{L}\right), \tag{1.2a}$$

$$\frac{\partial\overline{S}/\partial z}{S_*/\kappa|z|} = \phi_h\left(\frac{|z|}{L}\right). \tag{1.2b}$$

The surface-layer scale for temperature and salinity fluctuations (θ_* and S_*) are defined in a manner analogous to b_*. Note that the relations ϕ_m and ϕ_h are universal and have to be determined through measurements. A multitude of studies in boundary layer meteorology have examined and tested these relations, and the MOST can be considered a great success within the range of validity. Figure 1.1 shows the results from the Kansas experiment (1968) conducted above a flat wheat field. The collapse of data taken over several weeks and a wide range of stability greatly demonstrated the ability of this scaling and justified their applications in large-scale atmospheric circulation models. The mean gradients scaling implies an expression for the surface layer eddy momentum (K_m) and eddy heat (K_h) diffusivity that solely depends on surface fluxes and depth:

$$K_m = \frac{-\overline{w'u'}}{\partial\overline{u}/\partial z} = \frac{u_*\kappa|z|}{\phi_m}, \tag{1.3a}$$

$$K_h = \frac{-\overline{w'\theta'}}{\partial\overline{\theta}/\partial z} = \frac{u_*\kappa|z|}{\phi_h}, \tag{1.3b}$$

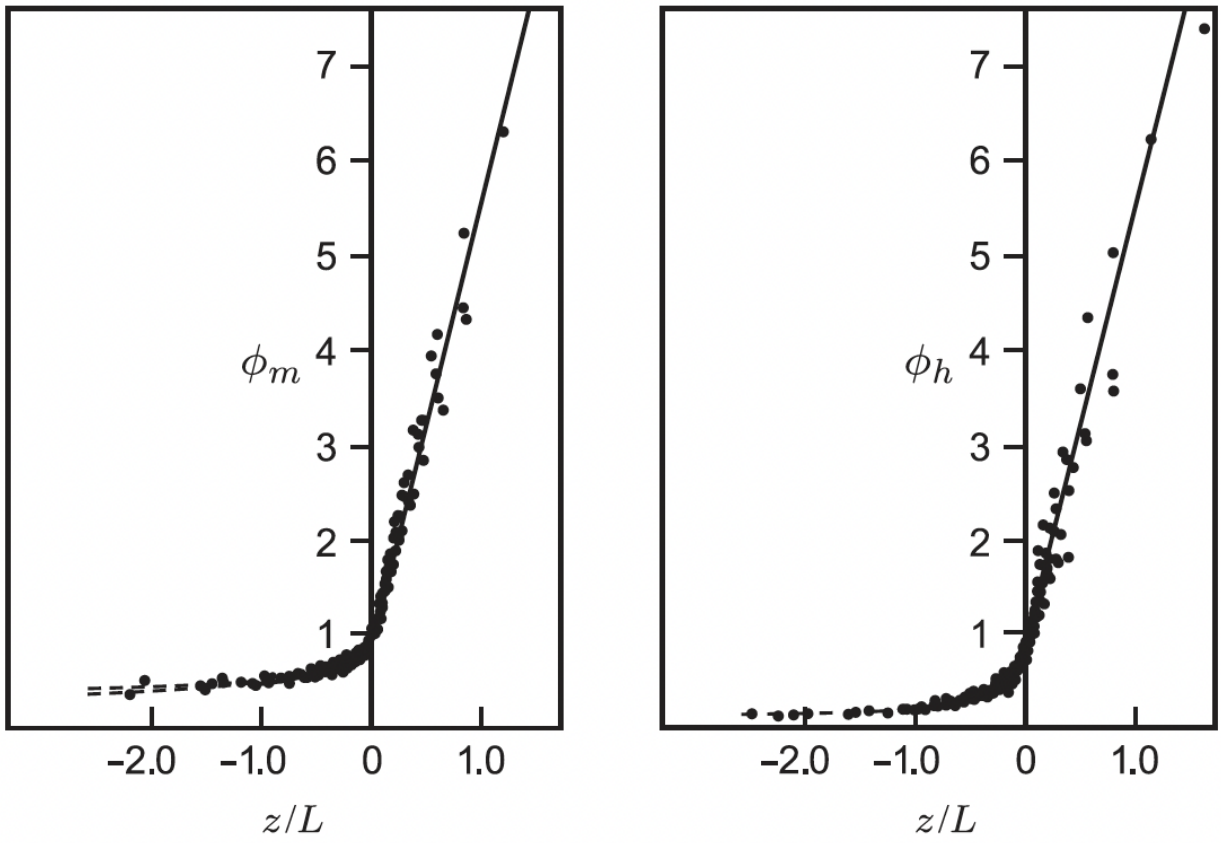

Figure 1.1: Kansas observations of the mean horizontal (streamwise) velocity shear [left, Eq. (1.1)] and mean potential temperature gradient [right, Eq. (1.2a)]. The height from the surface z in the atmosphere is equivalent to the distance from the surface $|z|$ in the oceanic coordinate. From *Businger et al.* (1971).

with $\overline{w'u'}$ and $\overline{w'\theta'}$ denoting the vertical kinematic stress and heat flux.

MOST also applies to high-order turbulence moments, such as the variance of vertical velocity fluctuations $\overline{w'w'}$ (or w_{rms}^2)

$$\frac{\overline{w'w'}}{u_*^2} = \phi_{ww}\left(\frac{|z|}{L}\right), \tag{1.4a}$$

the turbulent kinetic energy dissipation rate ϵ, the variance of temperature fluctuations $\overline{\theta'\theta'}$, etc.

A special asymptote for the Monin-Obukhov scaling is the local free convection limit

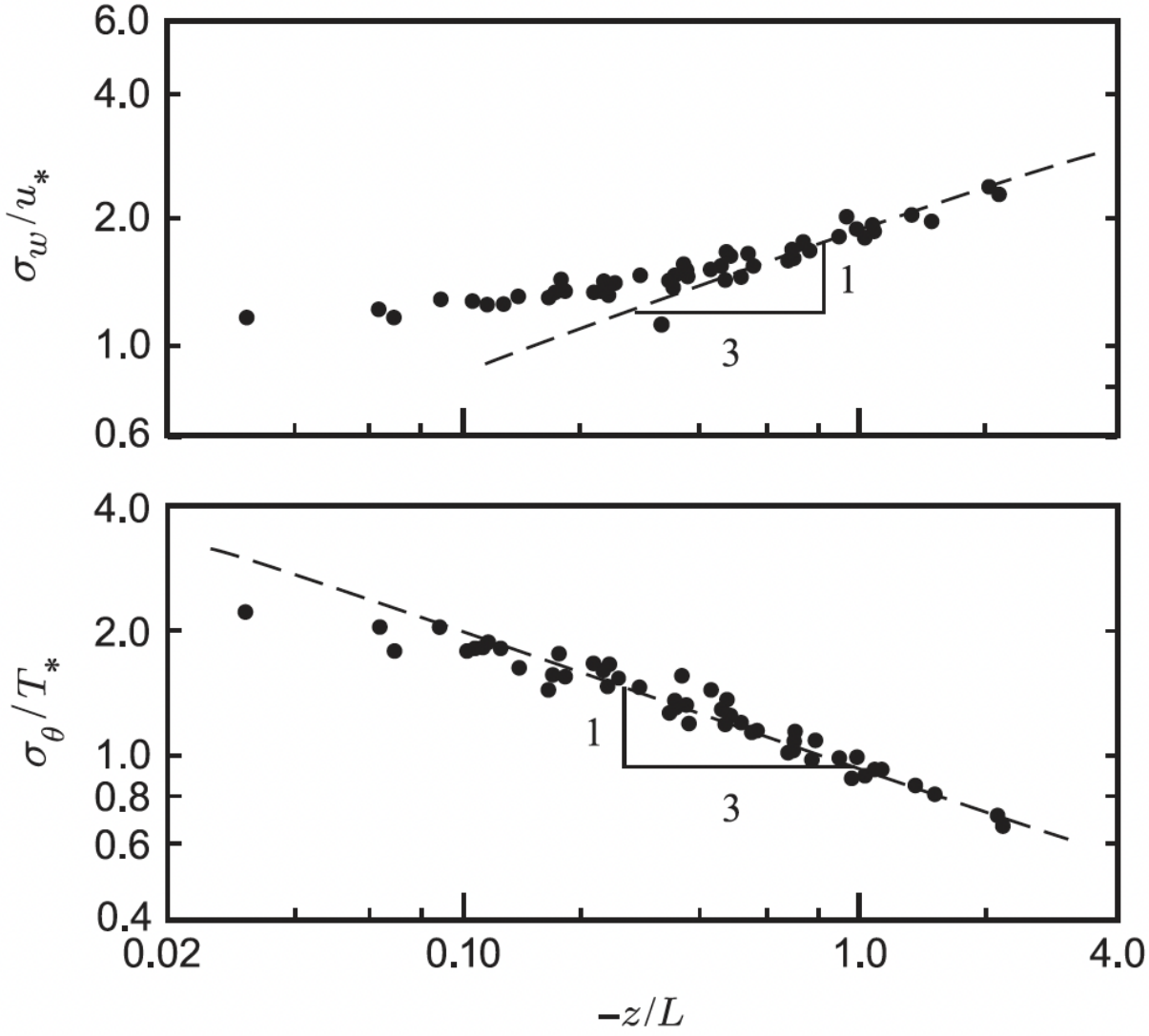

Figure 1.2: Kansas observations of the root mean square (*rms*) vertical velocity (upper) and *rms* temperature (lower) for unstable conditions. T_* is the same as the θ_* used in the text. The dashed lines indicate the expected asymptotic slope for very unstable conditions, Eq. (1.6). From *Wyngaard et al.* (1971).

under strong surface destabilizing fluxes ($|z|/L \to -\infty$). During such conditions, we expect that the mechanical turbulence driven by the shear production and characterized by u_* will be negligible at some depths (note the shear production decreases with $|z|$), but still within the surface layer. Given the fact that u_* is no longer a relevant parameter in the asymptotic unstable state, we end up with only 1 dimensionless quantity according to the Buckingham Pi theorem and it has to be a constant. Therefore, the only available scaling for the vertical velocity variance and the mean gradients are,

$$\frac{\overline{w'w'}}{(\mathcal{B}_0|z|)^{\frac{2}{3}}} = \frac{\overline{w'w'}}{u_f^2} = C_{ww}, \tag{1.5a}$$

$$\frac{\partial\overline{\theta}/\partial z}{\theta_f/\kappa|z|} = C_h. \tag{1.5b}$$

where C_{ww}, C_h are universal constants, u_f and $\theta_f = \mathcal{Q}_0/u_f$ is the velocity and temperature scale for local free convection conditions. Written in terms of the Monin-Obukhov scaling, equations (1.5) suggest the asymptotic behaviors of Monin-Obukhov universal functions when $-L \ll |z| \ll h$,

$$\phi_{ww} = \frac{\overline{w'w'}}{u_*^2} = C_{ww}\frac{u_f^2}{u_*^2} \sim \left(-\frac{|z|}{L}\right)^{\frac{2}{3}}, \tag{1.6a}$$

$$\phi_h = \frac{\partial\overline{\theta}/\partial z}{\theta_*/\kappa|z|} = C_h\frac{\theta_f}{\theta_*} \sim \left(-\frac{|z|}{L}\right)^{-\frac{1}{3}}. \tag{1.6b}$$

Again, atmospheric measurements are consistent with these predictions in very unstable conditions (Figure 1.2). The asymptotic slope of ϕ_m at large $-|z|/L$ values is still a subject of debate (*Businger*, 1973; *Maronga and Reuder*, 2017).

1.2.2 *Boundary layer scaling*

For the entire boundary layer, similarity scaling relationships are less well-defined. With an additional governing parameter, the boundary layer depth h, the dimensional analysis (Section 1.2.1) suggests that there are 3 independent dimensionless quantities for scaling

the boundary layer vertical structure. One is the non-dimensional variable of interest; it is conventional to take the other two as $|z|/h$ and h/L. The latter parameter describes the relative strength of wind stress and buoyancy forcing for the boundary layer as a whole, since the convective velocity scale

$$w_* = (h\mathcal{B}_0)^{\frac{1}{3}} = \frac{u_*}{\kappa^{\frac{1}{3}}} \cdot (-h/L)^{\frac{1}{3}}. \tag{1.7}$$

A general scaling that depends on both $|z|/h$ and h/L is challenging and often complicated by other factors like entrainment and horizontal density gradient. But the asymptotic state in strongly destabilizing conditions with $-h/L > 5$ is relatively well characterized by the mixed-layer similarity. For strongly destabilizing boundary layers, u_* is no longer a governing parameter and the vertical structure only depends on one dimensionless quantity $|z|/h$. This convective scaling and another similar scaling in neutral conditions are reviewed in detail in Section 4.2.

1.3 Motivation

While the Monin-Obukhov scaling has been proven valid and useful in atmospheric surface layers (ASL), its application in the oceanic surface layer is not warranted. Central to the development of the Monin-Obukhov scaling is the assumption that the surface layer is bounded by a flat wall, and the dynamics are merely controlled by surface fluxes. However, as every sailor knows, the ocean surface is far from being flat. Instead, it is dynamically shaped or violently restructured by surface gravity waves. These waves are dissipated by wave breaking, which injects and stirs momentum, energy, and bubbles into the near-surface layer. Their Lagrangian mean velocity, the Stokes drift, tilts vorticity and causes instability to form Langmuir turbulence that can penetrate deep into the boundary layer. In the past few decades, we have become more aware of their importance in the coupled air-sea system, and their dynamic effects on both atmospheric and oceanic boundary layers are thoroughly reviewed in *Sullivan and McWilliams* (2010).

With the consideration of surface waves in OSBL, it is natural to ask if the Monin-Obukhov scaling still works. In fact, recent detailed oceanic measurements and numerical studies have found significant influences of surface waves on the vertical mixing processes in OSBL [*D'Asaro* (2014) and references therein], suggesting that traditional parameterization approaches (including the Monin-Obukhov scaling) that ignore surface waves may not be a good representation of the turbulence in OSBL. From a modeling point of view, it is important to examine the effects of surface waves on the vertical structures of various boundary layer properties through scaling approaches, as they are essential to the predictions of sea surface temperature and salinity, lateral transport of material, estimates of turbulence, etc.

1.4 Outline

The overarching objective of this thesis is to advance our understanding of turbulence and mixing in the OSBL with the presence of surface waves. In particular, I will seek to better understand how surface wave-driven turbulence modifies the scaling of mean and turbulence quantities in the OSBL, and address the following two sets of scientific questions:

Question #1 Does the mean temperature gradient in the oceanic surface layer agree with the Monin-Obukhov scaling? If there are discrepancies, what are the contributions of Langmuir turbulence and surface wave breaking in setting these differences?

Question #2 Does the vertical velocity in the OSBL agree with the conventional scaling relations for ABL? How do we incorporate the effect of Langmuir turbulence into the scaling relations for vertical velocity variance?

While these questions will be investigated by using observational data from a few sampling sites, the physical processes involved in the scaling relations are relevant to

nearly all parts of the global ocean. The remainder of this thesis is organized into three chapters:

- Chapter 2 addresses ***Question #1*** by comparing observations of surface layer temperature gradient to predictions of the Monin-Obukhov scaling, and to predictions of simplified turbulence models that include either wave breaking or Langmuir turbulence. This chapter is reproduced from:

  > Zheng, Z., Harcourt, R. and D'Asaro, E., Evaluating Monin–Obukhov Scaling in the Unstable Oceanic Surface Layer, *J. Phys. Oceanogr.*, 51(3), 911-930, doi:10.1175/JPO-D-20-0201.1, 2021.

- Chapter 3 addresses the surface layer part of ***Question #2*** by comparing Lagrangian float measurements of vertical velocity variance to predictions of the Monin-Obukhov scaling. Additional scaling approaches are proposed to include the effect of Langmuir turbulence. This chapter is soon to be submitted as:

  > Zheng, Z., Harcourt, R., D'Asaro, E., and Shcherbina, A., Scaling Near-Surface Observations of Turbulent Vertical Velocity in the Ocean, Part I: Surface Layer

- Chapter 4 addresses the boundary layer part of ***Question #2*** by comparing the observation-based profiles of vertical velocity variance and skewness to predictions of conventional ABL scaling relations. A generalizing scaling for the boundary layer averaged vertical velocity variance is proposed to combine the effect of wind stress, surface buoyancy flux, and Stokes drift. This chapter is soon to be submitted as:

  > Zheng, Z., Harcourt, R., D'Asaro, E., and Shcherbina, A., Scaling Near-Surface Observations of Turbulent Vertical Velocity in the Ocean, Part II: Boundary Layer

In the end, Chapter 5 summarizes the major conclusions of this study, discusses the impacts of these results, and provides some ideas on future research directions.

Chapter 2

EVALUATING MONIN-OBUKHOV SCALING IN THE UNSTABLE OCEANIC SURFACE LAYER

Abstract

Monin-Obukhov Similarity Theory (MOST) provides important scaling laws for flow properties in the surface layer of the atmosphere and has contributed to most of our understanding of the near-surface turbulence. The prediction of near-surface vertical mixing in most operational ocean models is largely built upon this theory. However, the validity of MOST in the upper ocean is questionable due to the demonstrated importance of surface waves in the region. Here we examine the validity of MOST in the statically unstable oceanic surface layer, using data collected from two open ocean sites with different wave conditions. The observed vertical temperature gradients are found to be about half of those predicted by MOST. We hypothesize this is attributable to either the breaking of surface waves or Langmuir turbulence generated by the wave-current interaction. Existing turbulence closure models for surface wave breaking and for Langmuir turbulence are simplified to test these two hypotheses. Although both models predict reduced temperature gradients, the simplified Langmuir turbulence model matches observations more closely, when appropriately tuned.

2.1 Introduction

Two major components of the Earth system, the ocean and the atmosphere, interact with each other through their own planetary boundary layers (PBLs), where the motions of fluids directly respond to the surface stress and buoyancy flux across the air-sea interface on time scales less than a day (*Garratt*, 1992). Boundary-layer processes are naturally relevant

in many air-sea interaction problems [e.g., hurricanes (*Emanuel*, 2003), Madden-Julian Oscillation (*Zhang*, 2005), El Niño (*Dijkstra and Burgers*, 2002), etc.] and have great implications for accurate predictions of weather and climate. A comprehensive assessment of the role of the ocean and atmosphere in these problems requires a quantitative understanding of PBL dynamics, especially in terms of the vertical transports of momentum, heat and mass. These transports are largely carried by small-scale turbulent motions that must be parameterized in circulation models, due to limitations in computational capacity. The parameterization typically involves building approximations for turbulent fluxes, and using turbulence closure to estimate the effects of unresolved fluctuations upon the evolution of resolved mean fields. Informed by theories of molecular diffusion, early pioneers recognized that turbulent fluxes can be cast as functions of local mean gradients (*Taylor*, 1915; *Prandtl*, 1925; *von Kármán*, 1931), and developing flux-gradient relationships has thus become an important approach in modeling boundary layer flows (*Monin and Yaglom*, 1971).

Over the past 100 years, great progress has been made in the field of boundary layer meteorology (*LeMone et al.*, 2019), and several similarity theories have been developed to provide scaling laws for statistical flow characteristics in the atmospheric boundary layer (ABL). In particular, the near-surface portion of the ABL, the surface layer, is the best understood, in part because measurements are easiest to make there, but also because its dynamics are relatively simpler, as a result of large turbulent Rossby number Ro ($\sim U/f|z|$, where U and $|z|$ are characteristic velocity and length scales, f is the Coriolis parameter) and nearly constant turbulent fluxes (*Wyngaard*, 2010). Intrigued by such a well-defined problem, *Monin and Obukhov* (1954) proposed a similarity theory to delineate the vertical structure of an idealized atmospheric surface layer (ASL). Monin-Obukhov similarity theory (MOST) states that, under horizontally homogeneous and stationary conditions, every dimensionless scaling "group" in the surface layer is a universal function of the dimensionless height $\zeta = |z|/L$, the ratio of height —z— to the Obukhov length

(*Obukhov*, 1946)

$$L = u_*^3/\kappa B_0, \tag{2.1}$$

where u_* is the friction velocity, $\kappa = 0.4$ is the von Kármán constant and $B_0 = -\overline{w'b'}|_0$ is the near-surface buoyancy flux. The Obukhov length is negative (positive) in unstable (stable) conditions, and its magnitude is a rough estimate of the distance at which buoyancy production becomes dynamically important in the turbulent kinetic energy (TKE) budget relative to surface shear production.

Specifically, in the interest of the mean vertical structure of potential temperature (θ), or horizontal velocity (u), the dimensionless "group" for its vertical gradient is exclusively determined by ζ in the framework of MOST:

$$\frac{\partial \overline{\chi}/\partial z}{\chi_*/\kappa|z|} = \phi_\chi(\zeta), \quad \chi = \theta, u. \tag{2.2}$$

Here the overbar and prime denote time averaging and fluctuation, respectively; z is the upward vertical coordinate; $\chi_* = -\overline{w'\chi'}|_0/u_*$ is the fluctuation scale of flow variable χ with $\overline{w'\chi'}|_0$ being the near-surface kinematic flux of χ. For instance, the friction velocity $u_* = \sqrt{-\overline{w'u'}|_0} = \sqrt{\tau_w/\rho_0}$ is the fluctuation scale of horizontal velocity u, where the reference seawater density $\rho_0 = 1025$ kg m^{-3}, w is the vertical velocity, and the x-axis is chosen to align with the surface wind stress τ_w. The dimensionless gradient, or universal function ϕ_χ represents the effects of buoyancy on turbulence, relative to the law-of-the-wall scaling (*von Kármán*, 1931) for an unstratified surface layer ($\zeta = 0$). Numerous experimental efforts, both over land (*Businger et al.*, 1971, etc.) and sea surface (*Edson et al.*, 2004, etc.), have gone into determining the functional form of ϕ_χ for practical application. Many different analytic forms have been suggested in a voluminous body of literature (reviewed in *Högström*, 1996; *Foken*, 2006). Almost all empirical curves are similar in unstable conditions, while some disparities are common for expressions in stable conditions, presumably as a consequence of the intermittent and weak turbulence under stable stratification (*Mahrt*, 2014). The widely accepted set of universal functions for momentum (ϕ_m) and heat (ϕ_h) is based on the Kansas experiment (*Businger et al.*,

1971), from which particularly homogeneous and steady conditions and well-measured data were optimized to give:

$$\phi_m = 1 + 4.7\zeta, \qquad \phi_h = 0.74 + 4.7\zeta, \qquad 0 < \zeta < 1; \tag{2.3a}$$

$$\phi_m = (1 - 15\zeta)^{-\frac{1}{4}}, \phi_h = 0.74 \cdot (1 - 9\zeta)^{-\frac{1}{2}}, \ -2 < \zeta < 0. \tag{2.3b}$$

MOST has been generally successful in describing the flux-profile relationships in the ASL over a moderate range of ζ [as shown in Eqs. (2.3)]. It also laid a solid foundation for the later establishment of bulk transfer relations (the COARE algorithm, *Fairall et al.*, 1996, 2003), since its formulation implicitly suggests a parameterization for turbulent fluxes:

$$\overline{w'\chi'}|_0 = \frac{-u_*\kappa|z|}{\phi_\chi(\zeta)}\frac{\partial\overline{\chi}}{\partial z} = -K_\chi\frac{\partial\overline{\chi}}{\partial z}. \tag{2.4}$$

In this case, the turbulent flux and the gradient are related via a simple, stability-dependent eddy diffusivity $K_\chi = u_*\kappa|z|/\phi_\chi$. Thus far, many atmospheric models still rely on this method to deduce surface fluxes from near-surface mean profiles.

The ocean surface boundary layer (OSBL) mirrors its atmospheric counterpart in many ways, and its representation in circulation models also shares many features with the ABL. By analogy to the atmosphere, vertical mixing schemes for the OSBL also draw on knowledge from MOST. For example, the widely used K-profile parameterization (KPP, *Large et al.*, 1994) employs the universal function ϕ_χ to account for buoyancy effects in formulating a "turbulent velocity scale w_χ", and judiciously extends the surface layer scaling to the rest of the OSBL. Although not explicitly related to MOST, other higher order schemes (e.g., *Mellor and Yamada*, 1982; *Kantha and Clayson*, 1994; *Rodi*, 1987) were also tuned to match the surface layer similarity relations [Eqs. (2.3)] in a simplified framework (see Appendix 2.C). The incorporation of MOST in ocean models did improve their predictive capacity to some extent, however, considerable model errors still occur in many cases (e.g., too shallow mixed layer in the Southern Ocean, *Sallée et al.*, 2013). Some of these errors are potentially related to the assumption that the surface layer of the ocean can be characterized by the same scaling law as the ASL.

Not surprisingly, as the community becomes more aware of the dynamical impacts of surface gravity waves, suspicion arises about the validity of Monin-Obukhov scaling in the OSBL (*Sullivan and McWilliams*, 2010). Meanwhile, measurements of fluxes and gradients reported from coastal waters near Martha's Vineyard (*Gerbi et al.*, 2008) have already shown signs of invalidation.

In fact, the turbulence in the upper layers of the ocean and the consequent vertical mixing are inevitably affected by surface waves. Close to the surface, waves break intermittently as they propagate rapidly. One important effect of wave breaking is the downward injection of kinetic energy as turbulence. The classical law-of-the-wall scaling predicts the turbulence dissipation rate $\varepsilon \sim u_*^3/\kappa|z|$ in a neutral surface layer. However, near-surface measurements of ε in the ocean under strong wind and weak buoyancy forcings (*Agrawal et al.*, 1992; *Drennan et al.*, 1996; *Terray et al.*, 1996) repeatedly give much higher magnitude of ε than the classical prediction, and exhibit a more complicated, three-layer structure of ε: Within about one significant wave height (H_s) of the surface, ε is large and more or less constant; Below that, ε decays much faster than the -1 power-law before eventually resuming the classical scaling at deeper depths.

A second effect results as the Lagrangian-mean wave velocity, the Stokes drift, induces the Craik–Leibovich (CL) vortex force (*Craik and Leibovich*, 1976) and additional material transport to generate Langmuir circulations, cells, or turbulence that fill the entire OSBL. Conceptually, they can be viewed as arrays of counter-rotating vortices with elongated major axes oriented roughly downwind (*Sullivan and McWilliams*, 2010). Oftentimes, one can identify them by streaks of buoyant debris on the surface (*Langmuir*, 1938), and by bubble clouds trapped beneath these streaks using side-scan sonar (*Thorpe*, 1984; *Zedel and Farmer*, 1991, etc.). Although turbulence measurements in strongly convective OSBL have generally supported Monin-Obukhov scaling (*Shay and Gregg*, 1986), available field observations under strong wind conditions did show some deviations from the ABL (*D'Asaro*, 2014). First, the bulk average of the vertical TKE $\overline{w'w'}$ (*D'Asaro et al.*, 2014a), and dissipation rate (*Lombardo and Gregg*, 1989; *Carniel et al.*, 2012) all seem to be higher

than expected from classical scaling. Second, the ordering of turbulent velocity variances observed in shallow-water environment (*Gargett and Wells*, 2007) shows much stronger crosswind and vertical components than typical shear-driven turbulence, in which the velocity fluctuations are dominantly downwind. These differences are likely due to Langmuir turbulence, as large eddy simulation (LES) techniques can consistently predict these distinct features when the CL vortex force is included (*Skyllingstad and Denbo*, 1995; *McWilliams et al.*, 1997; *Tejada-Martínez and Grosch*, 2007; *Harcourt and D'Asaro*, 2008; *Kukulka et al.*, 2012, etc.). In stabilizing forcing conditions, Langmuir turbulence has also been found to inhibit the restratification and hence invalidates Monin-Obukhov scaling (*Kukulka et al.*, 2013; *Pearson et al.*, 2015).

As extra physics is introduced by processes related to surface waves, the surface layer of the ocean is expected to be dynamically different from the ASL. The canonical similarity theory with scaling parameters $|z|$, L, u_* and χ_* may become inadequate to encapsulate the relevant dynamics. Thus, it is incumbent upon us to examine the applicability of such flux-gradient relationships in the oceanic surface layer.

In this paper, we evaluate the validity of MOST in a surface wave-affected oceanic surface layer, using data collected from two open ocean sites. The rest of this manuscript is organized as follows. In Section 2.2, we introduce the in-situ measurements and data analysis, and compare observations to the predictions by MOST. In Section 2.3, we consider two hypotheses for the theory-observation discrepancies: one attributes the differences to surface wave breaking, and the other, to Langmuir turbulence. Each hypothesis is tested using a simplified turbulence closure model, and the model results are also compared to observations. Finally, a brief summary is presented in Section 2.4.

2.2 *Observations*

The evaluation of MOST flux-gradient relationships requires accurate measurements of surface fluxes and mean profiles in a quasi-steady surface layer. Datasets considered in this study are from two open ocean taut-line moorings (Figure 2.1). The subsurface sensors

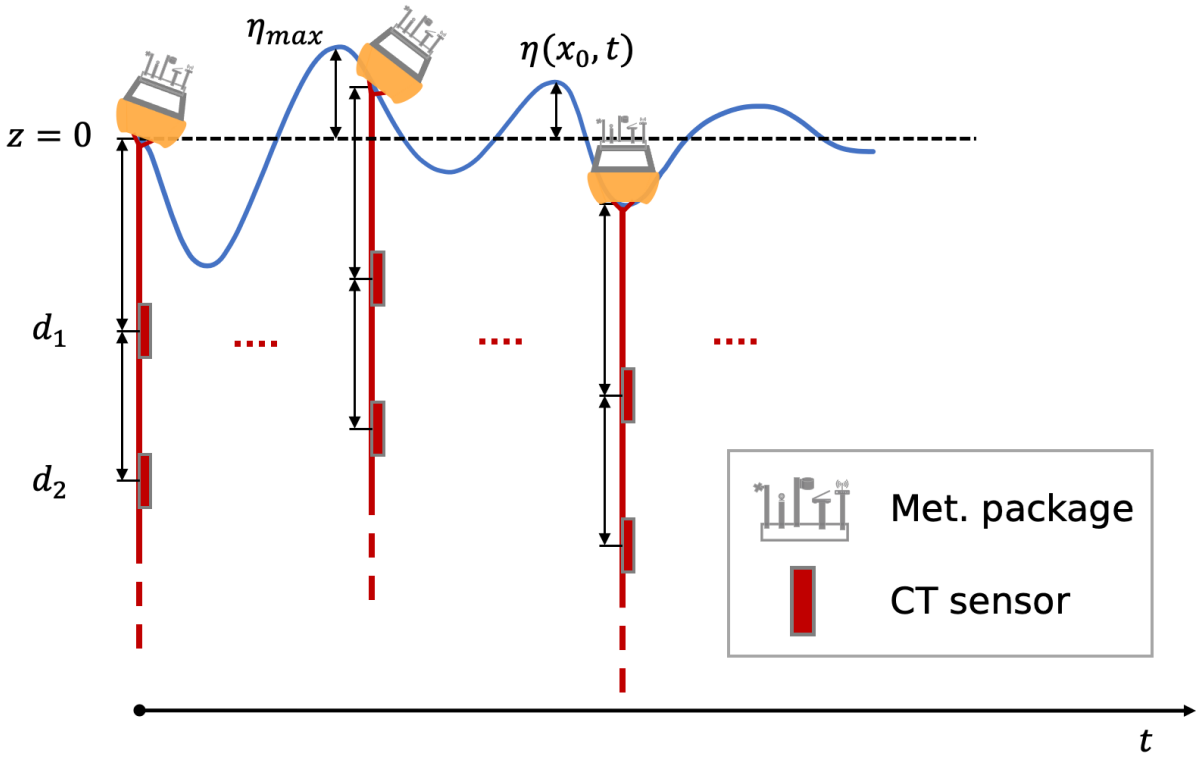

Figure 2.1: A sketch for typical taut-line mooring setup that measures oceanic conductivity-temperature (CT) and meteorological conditions over the sea surface. Hourly averaged data are used to investigate the response of the oceanic surface layer to surface forcing. The sensor's nominal depth along the mooring line, referenced to the mean sea surface ($z = 0$), is treated as the measurement distance from the surface.

are assumed to have been sampling upper ocean properties at their nominal depths. At both mooring sites, oceanic conductivity-temperature measurements are complemented by concurrent recordings of surface waves and a variety of surface observations for estimating air-sea fluxes, including winds, incoming solar and longwave radiation, rain, air temperature, relative humidity, and barometric pressure.

The first dataset (*Cronin*, 2007, updated daily) is from a long-term time series site, the Ocean Climate Station Papa (OCSP, nominally at 50.1°N, 144.9°W) in the northeastern Pacific. It has long been an attractive natural laboratory for boundary layer studies

because of the weak lateral processes there. During active periods, the OCSP mooring is instrumented with sensors to measure subsurface temperature and conductivity once every 10 minutes. The meteorological sensors mounted above the buoy have higher sampling rates, usually 1 or 2 Hz, but the recorded resolutions vary from 1 to 10 minutes. Hourly data were created by applying Hanning filters to the original records (*Anderson et al.*, 2018). Since 2010, a Datawell Waverider buoy has also been deployed near the OCSP mooring to report directional surface wave spectrum every 30 minutes (*Thomson*, 2019). In order to have simultaneous hydrographic, meteorological and surface wave measurements, data from OCSP are truncated to a time period from June 2010 to November 2019.

The second dataset (*Farrar*, 2015) was collected during the field campaign of the first Salinity Processes in the Upper-ocean Regional Study (SPURS-I, *Lindstrom et al.*, 2015; *Farrar et al.*, 2015). As part of the monitoring array in the subtropical North Atlantic (approximately 24.5°N, 38°W), a surface buoy was deployed in September 2012 and recovered in September 2013. The SPURS-I mooring carried similar meteorological sensors to measure meteorological conditions once per minute and transmit hourly averages via satellite. Below the surface, the mooring line was equipped with a denser array of sensors ($\sim$1 m spacing in upper 10 m) for temperature and conductivity measurements in every 5 minutes. In addition, the buoy also had an instrument to measure the height and direction of surface waves by recording the angular accelerations of pitch, roll, and yaw, as well as the vertical heave (*Bouchard and Farrar*, 2008). These raw data were later processed by J. T. Farrar (2014, unpublished data) to produce hourly records of directional surface wave spectrum.

For both datasets, the profile of Stokes drift velocity ($\boldsymbol{u}^s$) and its vertical shear are estimated from the directional wave spectrum, following the method described in Appendix 2.A. Surface wind stress, surface heat, and salt fluxes were estimated using the TOGA COARE 3.0 algorithm (*Fairall et al.*, 2003) from measured meteorological variables (see details about the flux calculations at OCSP on https://pmel.noaa.gov/ocs/flux-documentation). Considering the penetrative effect of shortwave radiation I, the buoyancy

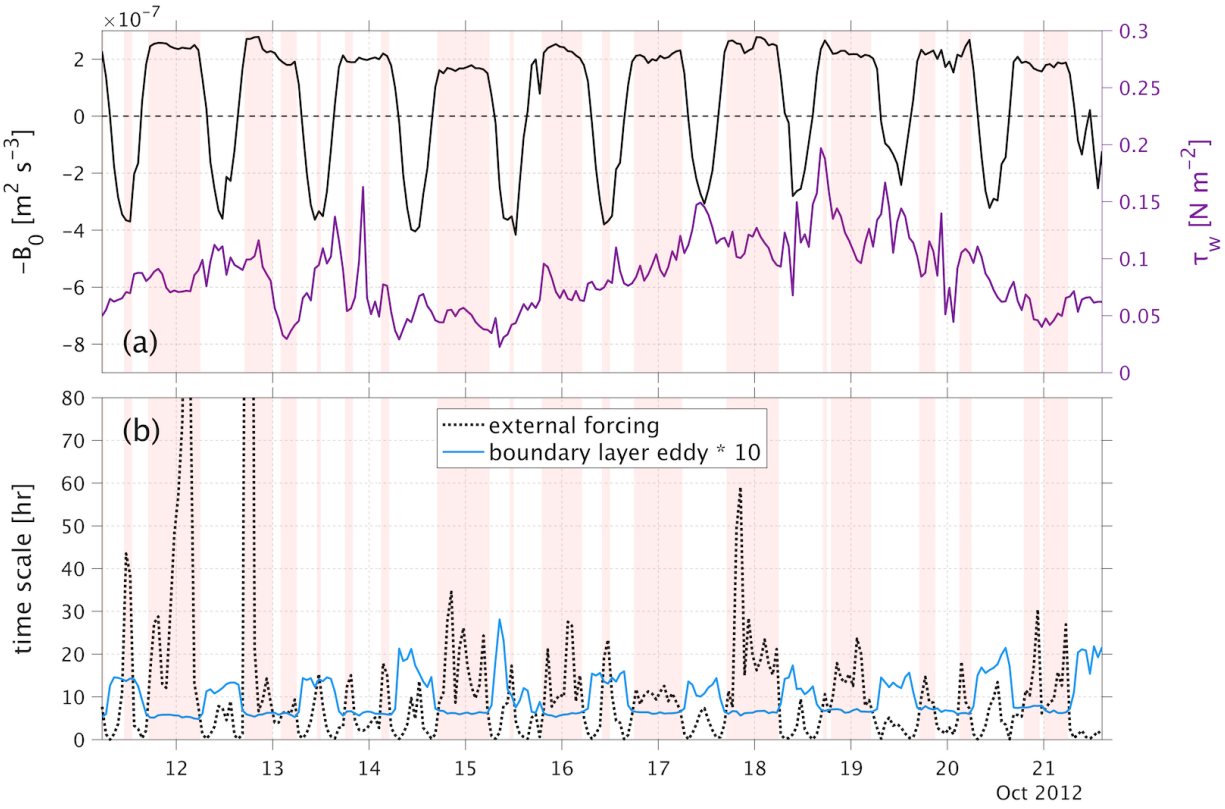

Figure 2.2: An example from SPURS-I shows the selection of quasi-steady periods. The upper panel gives a time series of the near-surface buoyancy flux (B_0, black) and wind stress (τ_w, purple) for about 10 days. The lower panel shows the time scale of external forcing (black, including the buoyancy and the wind forcing) and 10 times that of the boundary layer eddy (blue). The quasi-steady period (vertical red shading) is reached when the time scale of external forcing exceeds 10 times that of the boundary layer eddy.

flux to a layer of depth $|z|$ is computed following *Large et al.* (1994):

$$B_f(z) = B_0^t + \left[B^r(0) - B^r(z)\right], \tag{2.5}$$

where B_0^t is the turbulent component of the buoyancy flux due to sensible heat flux, latent heat flux, net downward longwave radiation, and salt flux at the surface; B^r is the radiative component that decays with depth. The sign convention for B_f is positive (negative) when the buoyancy flux is into (out of) the ocean. B^r is modeled by a 2-band exponential profile (*Paulson and Simpson*, 1977):

$$B^r(z) = \frac{\alpha g I_0}{\rho_0 c_p} \cdot \left[r_s e^{z/\mu_1} + (1 - r_s) e^{z/\mu_2}\right], \tag{2.6}$$

where I_0 is the net downward shortwave radiation at the surface, α is the thermal expansion coefficient of seawater, g is the gravitational acceleration, c_p is the specific heat at constant pressure. Here, the solar spectrum is divided into 2 wavelength bands, with fraction r_s and $1 - r_s$ of the total radiation. Each band decays exponentially with a characteristic e-folding length scale μ. The values of r_s, μ_1 and μ_2 depend on *Jerlov* (1976) water type. Based on a global climatology of water optical properties (*Simonot and Le Treut*, 1986), water type II and IB are assumed for OCSP and SPURS-I, respectively (Table 2.1). The depth-dependent buoyancy flux B_f is used to calculate the Obukhov length, as the buoyancy force experienced by seawater changes with depth. This treatment of the solar radiation is one of the simpler possible formulations, but any limitation of this approach is not likely to have a big impact on our following results, since most data selected are from nighttime (Section 2.2.1).

2.2.1 *Mean temperature profiles and vertical gradients*

For consistency, time series with resolution finer than hourly are averaged in one-hour intervals. As the salinity measurements are more susceptible to sensor drift (see Appendix 2.B) and the accuracy is not as high as temperature ($\pm$ 0.002 °C), they are only used to determine density for the purpose of identifying the boundary layer depth H.

Table 2.1: The Jerlov water type and corresponding constants assumed in this study.

Site	Jerlov water type	r_s	μ_1 (m)	μ_2 (m)
OCSP	II	0.77	1.5	14
SPURS-I	IB	0.67	1.0	17

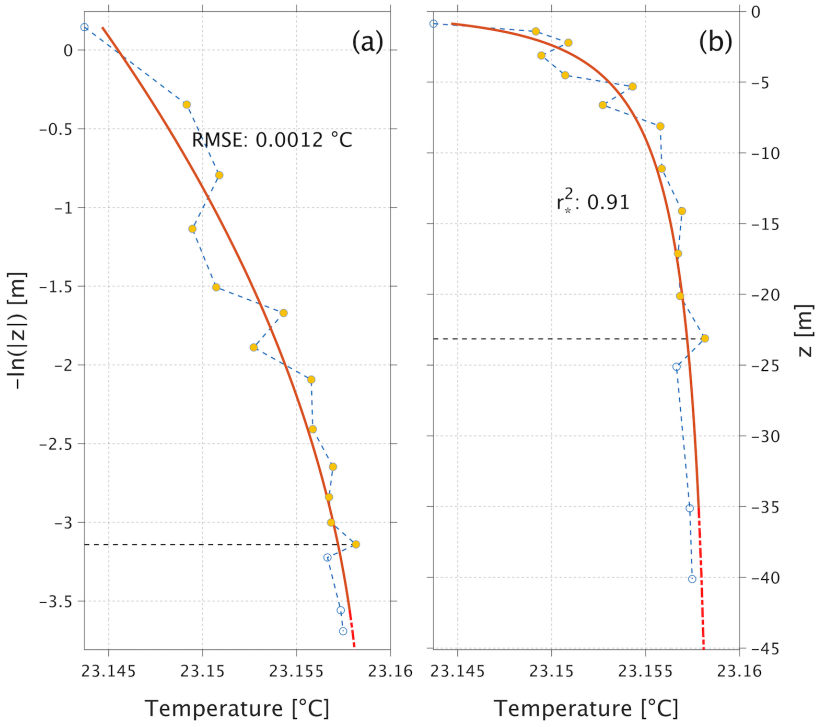

Figure 2.3: An example from SPURS-I shows the second-order polynomial fit (2.7) of temperature profile. The original profile (blue dash line with circles), taken from local time 03:30 of February 10, 2013, is shown in both (a) logarithmic and (b) linear coordinates. The solid red line shows the best fit using data within the depth range it covers. The dash-dotted red line shows the extrapolated polynomial function outside the fitting range. Surface layer depth ($0.2H$) is indicated by the horizontal black dash line. Solid yellow circles mark the depths where dimensionless gradients are computed. r_*^2 is the goodness of fit adjusted for the degrees of freedom.

Only temperature data are directly used in the validation of MOST. At first glance, the temperature profile may seem smooth, but if one zooms into the surface layer, small-scale serrations are almost ubiquitous (Figure 2.3), probably owing to the different thermal responses of sensors. To reduce these noises and extract the mean thermal stratification, we follow the standard method in atmospheric studies (*Businger et al.*, 1971) to fit every temperature profile with a second-order polynomial function in logarithmic space:

$$\overline{\theta}(z) = p_2(\ln|z|)^2 + p_1 \ln|z| + p_0 \tag{2.7}$$

where p_0, p_1, and p_2 are the polynomial coefficients. The logic behind this logarithmic fit is that the profile of any mean quantity in the surface layer is expected to vary logarithmically with height (depth) in neutral conditions, while in non-neutral conditions, the profile is usually slightly curved in the logarithmic coordinate (*Panofsky*, 1963). For each temperature profile, multiple second-order polynomial fits are conducted within the depth range of $[0, 0.3H]$, using various numbers of data points. Three criteria are required for a fit to be considered as good: (1) the first and second order vertical derivatives are monotonic functions; (2) the root mean square error (RMSE) is less than $0.002°C$; (3) after adjusting for degrees of freedom, the coefficient of determination (r^2) is larger than 0.5. Among all the good fits for a profile, we pick the best one, if there is any, that has the smallest RMSE. If no best fit can be found, then the profile is excluded from the analysis. In total, about 89% and 54% of the profiles are excluded in OCSP and SPURS-I datasets, respectively, either due to the lack of robustness of fits (17% and 16% in unstable conditions, 12% and 27% in stable conditions), or insufficient data in the surface layer. The best fitting function is used to calculate temperature gradients and ϕ_h at different levels z_i:

$$\frac{\partial\overline{\theta}}{\partial z} = \left(2p_2 \ln|z_i| + p_1\right)/z_i, \tag{2.8a}$$

$$\phi_h = \frac{\partial\overline{\theta}}{\partial z} \Big/ \frac{\theta_*}{\kappa|z_i|}, \tag{2.8b}$$

where θ_* is computed using the heat flux that includes depth-varying solar radiation. Considering the uncertainty of derivatives at the two ends of the fitting range, temperature gradients are only calculated at the interior depths of the fitting range, but still within the surface layer (Figure 2.3). This also diminishes the effect of flow distortion on temperature gradients, as the first temperature measurement below the surface usually contains a signal from seawater at shallower depth, due to the distortion of near-surface flow by the buoy.

2.2.2 *Surface layer depth*

Departing from the ASL convention, which considers the lower 10% of the ABL, we treat the upper 20% of the OSBL as the surface layer. The depth of the OSBL is determined as the shallowest level where the linearly interpolated bulk Richardson number $\mathrm{Ri_b}$ reaches a critical value $\mathrm{Ri_b^c}$. In the absence of reliable near-surface velocity measurements at the moorings considered here, buoyancy profiles are used to define a bulk Richardson number in reference to a neutral logarithmic shear profile, computed at each level z_i as

$$\mathrm{Ri_b}(z_i) = \frac{(b_1 - b_i)(z_1 - z_i)}{|\boldsymbol{u}_1 - \boldsymbol{u}_i|^2} \approx \frac{\kappa^2 (b_1 - b_i)(z_1 - z_i)}{u_*^2 \ln^2(z_i/z_1)}, \tag{2.9}$$

where $b = -g(\rho - \rho_0)/\rho_0$ is the buoyancy computed from local potential density ρ, and subscript 1 denotes quantity measured at the first sensor depth. Due to substantial sensor drifts, the salinity measurements from the SPURS-I mooring are calibrated (see Appendix 2.B) before calculating potential density. Different values of $\mathrm{Ri_b^c}$ are tested and the optimal one is chosen to have the best coincidence with the mixed layer depth diagnosed from the 0.03 kg m^{-3} criteria (*de Boyer Montégut et al.*, 2004). The resulting $\mathrm{Ri_b^c}$ for OCSP and SPURS-I are 0.85 and 2.30, respectively. Since the bulk Richardson number here is defined with an idealized velocity shear, it is not surprising to arrive at a critical value different from traditional values. The computed surface layer depths are used to confine the domain of our analysis and minimize uncertainty in the scaling results.

However, the surface layer tends to be very shallow (a few meters) during daytime, so the majority the data used comes from unstable situations, often during nighttime.

2.2.3 *Quasi-steady state*

The turbulence in the OSBL can be nonstationary due to diurnal variations of atmospheric forcing; it can also be inhomogeneous in the horizontal as surface properties vary spatially. However, if the time and length scales of the OSBL are small relative to those of the external forcing, the OSBL may be considered as quasi-steady and horizontally homogeneous. Oftentimes, the boundary layer depth H and the large-eddy turnover time T_H are regarded as the internal length and time scale of the OSBL. The boundary layer eddies driven by the wind and surface buoyancy loss can be characterized by velocity scales u_* and w_*. The larger of these two is used to determine the turnover time here:

$$T_H = H/\max(u_*, w_*), \tag{2.10}$$

where $w_* = \big(-H \cdot B_0\big)^{1/3}$ is the free-convection velocity scale (*Deardorff*, 1970) that is set by the boundary layer depth and near-surface buoyancy flux. The external forcing changes as the wind stress, or buoyancy flux varies with time. The time scale of each forcing is estimated as the ratio of the forcing magnitude to the temporal rate of change:

$$T_W = \left|\frac{\tau_w}{\partial \tau_w / \partial t}\right|, \tag{2.11a}$$

$$T_B = \left|\frac{B_0}{\partial B_0 / \partial t}\right|. \tag{2.11b}$$

Therefore, we define a period when the time scales of both wind stress (T_W) and buoyancy flux (T_B) exceed 10 times the large-eddy turnover time (T_H) as the quasi-steady period. An example of such selection is given in **??**. As for the condition of horizontal homogeneity, we argue that the spatial scales of horizontal variability at both sites are much larger than the thickness of the OSBL ($\sim$ 100 m), so that the OSBL turbulence does not feel the effect of horizontal heterogeneity. These boundary layer approximations, including the quasi-

steady state and horizontal homogeneity, are also assumed in our later simplification of PBL models (Appendix 2.C and Section 2.3).

2.2.4 *Comparison of Monin-Obukhov scaling with observations*

According to MOST, the temperature difference between any two levels z_i, z_j in the surface layer should be

$$\Delta\overline{\theta}_{ij} = \overline{\theta}(z_i) - \overline{\theta}(z_j) = \int_{z_j}^{z_i} \phi_h(|z|/L)\frac{\theta_*}{\kappa|z|}dz, \tag{2.12}$$

where $|z_i|$ and $|z_j|$ are the nominal sensor depths along the mooring line, and the universal function ϕ_h used here is based on the results [Eqs. (2.3)] from the Kansas experiment. These theoretical predictions of temperature difference are computed through trapezoidal numerical integration and are compared to those directly calculated from the fitted profiles. The comparison (Figure 2.4a and 2.4c) shows that the observed temperature gradients are about half of the theoretical predictions, over most of the observed range of $\Delta\overline{\theta}$. This is robust at both sites, and is not subject to either the selection of quasi-steady periods in Section 2.2.3, or the profile fitting in Section 2.2.1. More intuitively, the juxtaposition (Figure 2.4b and 2.4d) of the observed profiles and the MOST-predicted profiles also indicates that the ocean has weaker thermal stratification in the surface layer than the atmosphere, or than that predicted by MOST.

The distribution of the observed dimensionless temperature gradient ϕ_h in ζ is shown in Figure 2.5. Again, the smaller observed values of ϕ_h below the Kansas curve are consistent with the smaller linear regression slopes (less than 1) in Figure 2.4a and 2.4c. The deviation of the observations from the Kansas curve decrease as $|\zeta|$ increases, indicating that the failure of MOST mainly happens in the forced convection regime ($-1 < \zeta < 0$). Looking more closely, the different linear regression slopes (Figure 2.4a and 2.4c) at these two sites, and the disparity of ϕ_h values in the same ζ bin (Figure 2.5) may imply that the ϕ_h in oceanic surface layer does not only depend on ζ, and that other forcing parameters not considered in MOST might be important in setting the near-surface

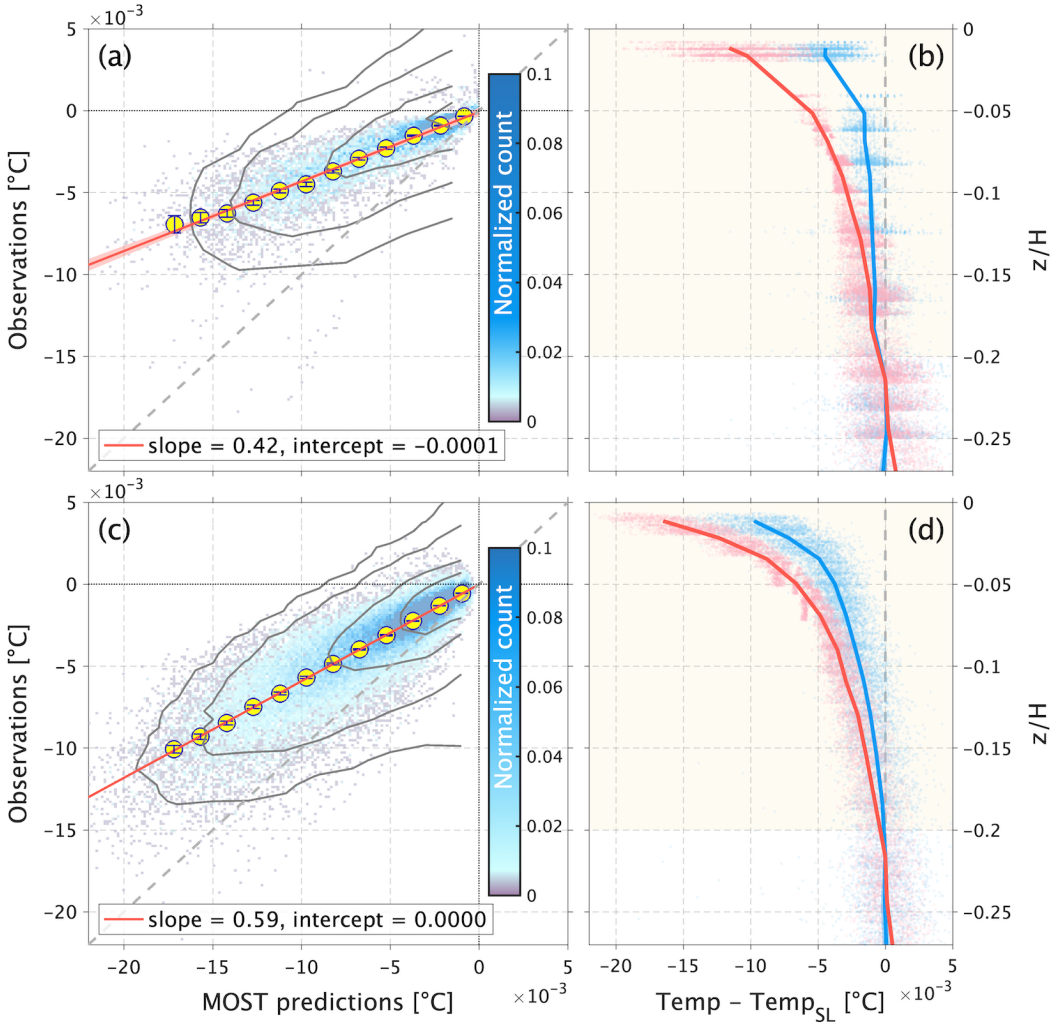

Figure 2.4: Comparisons between observations and MOST predictions of surface layer temperature. (a) Observed vertical temperature differences ($\Delta\overline{\theta}$) at OCSP versus those predicted by MOST. Scatter uses $\Delta\overline{\theta}$ from fitted profiles during quasi-steady periods, while probability contours for 30%, 60%, 90% and 96% of distribution use $\Delta\overline{\theta}$ from all original profiles. The color of the scatter represents data density; yellow circles show bin averages of scatter with 95% confidence intervals (error bars); the red line shows the linear fit of bin averages. (b) Observed temperature profiles (blue) versus those predicted by MOST (red). Predictions are obtained by cumulatively integrating the predicted gradients with ϕ_h from Eqs. (2.3). Temperatures are referenced to "Temp$_{SL}$", the mean values in the surface layer (area shaded yellow). Solid lines are ensemble averages of individual profiles (dots). Only profiles with boundary layer depth deeper than 50 m are used. For better visual comparison, profiles have been shifted to make the ensemble averages zero at the surface layer depth. (c) and (d) Same as (a) and (b) but use data from SPURS-I.

temperature gradients. Moreover, in the surface layer, smaller dimensionless temperature gradients suggest larger thermal diffusivity, as K_h is inversely proportional to ϕ_h [Eq. (2.4)]. These observational evidences clearly show that the classical Monin-Obukhov scaling for temperature is not appropriate for direct application in the unstable oceanic surface layer. This is a major finding of this study and the rest of this paper seeks to identify what process is responsible for the weaker thermal gradients, by considering surface waves.

2.3 *Hypotheses testing*

The reduced temperature gradients in the unstable oceanic surface layer naturally leads to the question of why the ocean is different from the atmosphere in this regard. As mentioned earlier, surface waves related processes can modify OSBL dynamics significantly, but they are not included in the current form of MOST. Therefore, we consider two hypotheses to explain the discrepancies between observations and MOST: (1) Surface wave breaking is responsible for the observed weak temperature gradients; (2) Langmuir turbulence is responsible for the observed weak temperature gradients. Although our current understanding of these two processes is still incomplete, attempts have been made to incorporate them into models for the PBL. Encouragingly, models with surface wave breaking (*Craig and Banner*, 1994; *Burchard*, 2001) have shown some skill in reproducing the near-surface dissipation measurements under breaking waves, and models including Langmuir turbulence were found to better predict observed vertical TKE profiles (*Harcourt*, 2015). Given the success of existing models in representing these two processes, we will take them as the approach for hypotheses testing.

The PBL models adopted here are commonly termed as Second Moment Closures (SMCs), and use solutions of second-order turbulence statistics to inform the turbulent diffusivity in closing mean equations. In view of the relatively simple dynamics in the surface layer, a full SMC can be accordingly simplified to a super-equilibrium version, where turbulence production is locally balanced by dissipation. Classical SMCs (e.g., *Mellor and Yamada*, 1982; *Kantha and Clayson*, 1994) with no explicit consideration of

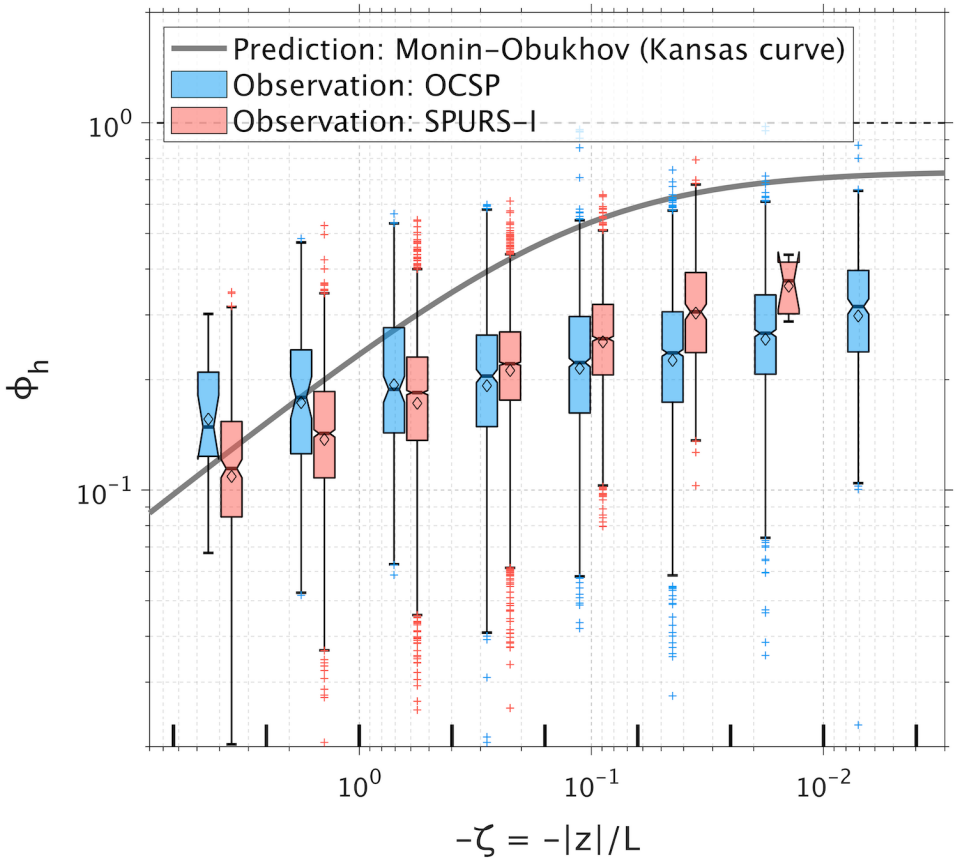

Figure 2.5: Distribution of the observed dimensionless gradient ϕ_h in ζ space. Only data from quasi-steady periods are used. Dimensionless gradients from fitted profiles are grouped into logarithmically spaced bins (see vertical bars at the bottom). The paired boxes are horizontally offset from the bin center to show the distribution of $\log_{10}(\phi_h)$ from OCSP (blue) and SPURS-I (red) in the same ζ bin. On each box, the central mark indicates the median; the diamond indicates the mean; the top and bottom box edges show the upper and lower quartiles, respectively; the whiskers show the 99th and 1st percentiles; the notch shows the comparison interval of the median. Medians of the ϕ_h from OCSP and SPURS-I are deemed different at a 5% significance level if their intervals do not overlap in the same bin. Data beyond whiskers are denoted by '+'. Empirical relationship [Eq. (2.3b)] from the Kansas experiment (*Businger et al.*, 1971) is displayed as the thick gray curve.

surface wave effects, when reduced to the super-equilibrium version, are known to have independent temperature and momentum scalings that are very similar to MOST. An example of the derivation of model intrinsic similarity relations from *Kantha and Clayson* (1994) is given in Appendix 2.C. Also, full SMCs have been shown to approximately follow Monin-Obukhov scaling in steady states when constant forcing is imposed (*Burchard et al.*, 1998). However, for an SMC that includes surface wave effects, we expect that the model-derived temperature and momentum scalings would deviate from MOST.

2.3.1 *Similarity relations in surface wave breaking model*

Craig and Banner (1994) presented the first of many models including the effects of surface wave breaking. They modified the classical *Mellor and Yamada* (1982) level $2\frac{1}{2}$ model by adding a down-the-gradient flux of TKE from the dissipated wave energy, which was assumed to be in proportion to u_*^3. Their model is successful in reproducing the high dissipation and the elevated decay with depth, but the analysis and model-observation comparison was conducted for a neutral boundary layer. In more general scenarios, buoyancy is also important for turbulence; hence we similarly alter the equation for TKE ($q^2/2$) from the classical super-equilibrium SMC [Eq. (C1a)] to get

$$-\frac{\partial}{\partial z}\left[q\ell S_q \frac{\partial}{\partial z}\frac{q^2}{2}\right] = -\overline{w'u'}\frac{\partial \overline{u}}{\partial z} + \alpha g \overline{w'\theta'} - \frac{q^3}{B_1 \ell}. \tag{2.13}$$

Variables used here are the same as defined in Appendix 2.C. The left-hand side of Eq. (2.13) represents the turbulent diffusion of TKE by using a diffusivity that is proportional to the product of turbulent velocity scale q and length scale ℓ with constant $S_q = 0.2$ (*Mellor and Yamada*, 1982). On the right-hand side are the shear production, buoyancy production (destruction), and dissipation of TKE. Technically, Eq. (2.13) no longer indicates a super-equilibrium state, so we will refer to it as "super-equilibrium", since it is still a simplified version of the original wave-breaking model. Assuming dissipation is constant in the wave breaking layer ($|z| < z_0$, z_0 is the roughness scale), the scaling of *Terray et al.* (1996) argues that about half of the wave energy input is dissipated

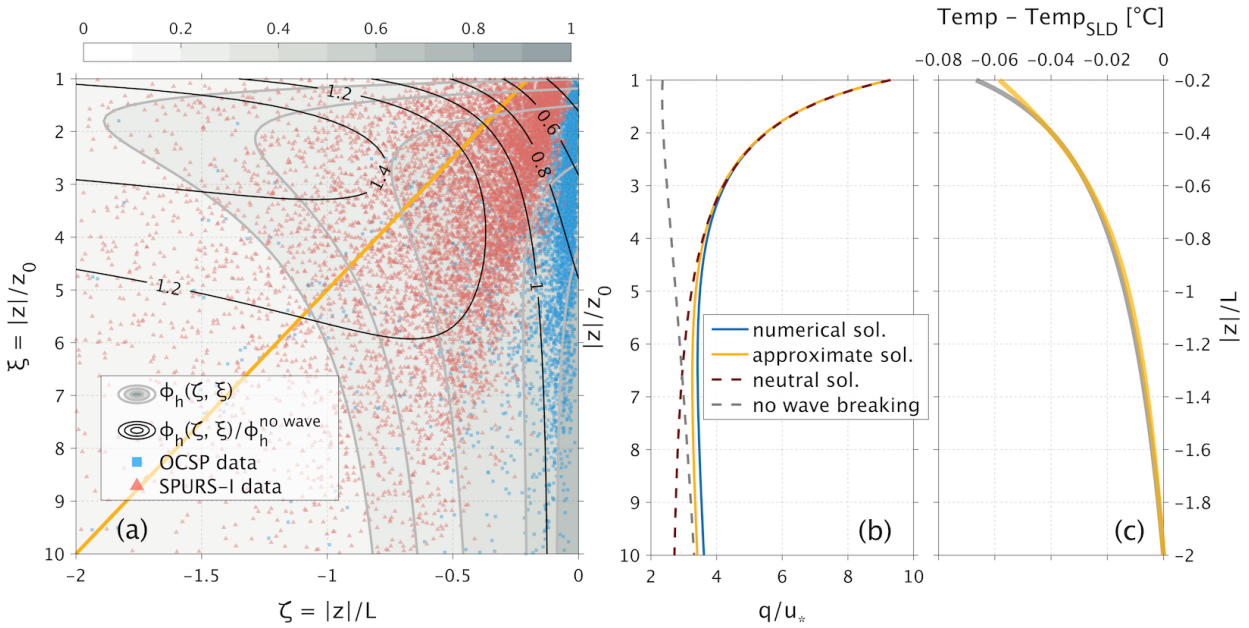

Figure 2.6: (a) Variations of ϕ_h in the "super-equilibrium" ("SE") wave breaking model (with $\ell = \kappa|z|$) where q^3 is approximated by Eq. (2.17). Color-filled contours show the values of ϕ_h (0.22, 0.25, 0.3, 0.45, 0.6) predicted by the model. Black isolines show the ratios of the model-derived ϕ_h to those from the classical super-equilibrium SMC (*Kantha and Clayson*, 1994) with no wave effects. The yellow line indicates the case ($z_0/L = -0.2$) plotted in (b) and (c). Observed parameter values at OCSP (blue) and SPURS-I (red) are overlaid. Roughness lengths are determined from significant wave heights with $z_0 = 0.6H_s$. (b) Turbulent velocity scale q in the "SE" wave breaking model when $z_0/L = -0.2$. The blue and yellow lines show the numerical and approximate solution of Eq. (2.16), respectively. Brown and gray dash line show the solution in the neutral limit (*Craig*, 1996) and in case of no wave breaking, respectively. (c) Temperature (referenced to the value at the surface layer depth) profiles predicted by MOST (gray) and by the "SE" wave breaking model (yellow). Predictions are obtained by cumulatively integrating the predicted gradients with ϕ_h from Eqs. (2.3) (gray), and from the model (yellow) with $z_0/L = -0.2$, assuming z_0 = 1.2 m, 12 m surface layer depth and 10 m s^{-1} wind at 10 m height.

in the breaking layer; the other half is transported downward via turbulent diffusion. Thus, the upper boundary condition for Eq. (2.13) is

$$q\ell S_q \frac{\partial}{\partial z}\frac{q^2}{2} = \frac{1}{2}\alpha_b u_*^3, \quad \text{at } z = -z_0, \tag{2.14}$$

where the coefficient α_b is commonly regarded as a function of sea state (*Drennan et al.*, 1992). However, for well-developed waves, its dependence on the sea state is so weak that one can treat it as a constant of order 100. For simplicity, 100 is used here, and we also require the energy flux due to breaking waves approaching zero as depth increases.

By defining a strained coordinate

$$y = \int_{-z_0}^{z} \frac{dz'}{\ell} = \frac{1}{\kappa}\ln\frac{-z_0}{z}, \tag{2.15}$$

where ℓ has been assumed to be $\kappa|z|$, and applying the surface layer approximations [Eqs. (2.35a, 2.35g, 2.35i)], equation (2.13) can be reorganized into

$$\frac{\partial^2}{\partial y^2}q^3 - \frac{3}{B_1 S_q}q^3 = \frac{-3u_*^3}{S_q}(\phi_m - \zeta). \tag{2.16}$$

As the second-order derivative of $(\phi_m - \zeta)$ in the surface layer is quite small, the analytical solution for Eq. (2.16) can be approximated as

$$q^3 = u_*^3\left[B_1(\phi_m - \zeta) + c\xi^{-n}\right], \tag{2.17}$$

with a new parameter $\xi = |z|/z_0$, and constants $c = \frac{\alpha_b}{2}\sqrt{3B_1/S_q}$, $n = \sqrt{3/B_1 S_q \kappa^2}$. Replacing Eq. (2.36a) in the classical super-equilibrium SMC with the dimensionless form of Eq. (2.17), we arrive at a set of non-dimensional equations that includes the effects of wave breaking:

$$q^{*3} = B_1(\phi_m - \zeta) + c\xi^{-n}, \tag{2.18a}$$

$$\frac{1}{3A_1 q^*} = \phi_m\left[r - C_1 - \frac{\big(6A_1 + 3A_2(1-C_2)\big)\zeta}{q^{*3}}\right] - \phi_h\left[\frac{3A_2\zeta}{q^{*3}}\right], \tag{2.18b}$$

$$\frac{1}{3A_2 q^*} = \phi_h\left[r - \frac{\big(6A_1 + B_2(1-C_3)\big)\zeta}{q^{*3}}\right]. \tag{2.18c}$$

Using the trust-region dogleg algorithm (*Powell*, 1970) implemented in MATLAB, equations (2.18) are solved to predict ϕ_h as a function of ζ and ξ (Figure 2.6a). This model considers extra TKE input from surface wave breaking, so its temperature scaling ϕ_h is additionally regulated by the distance from the depth of energy injection z_0. However, the influence of surface wave breaking is mainly confined in a shallow layer of thickness about $6z_0$. Compared to the scaling from the classical super-equilibrium SMC (or MOST), the reduction of ϕ_h in the forced convection regime can be up to 60%, while the deviation from MOST gradually diminishes as the magnitude of ξ or ζ becomes larger. Enhancement of ϕ_h can also happen in stronger unstable conditions, and this model behavior is traced back to the reduced vertical TKE ratio ($\overline{w'w'}/q^2$), or mixing efficiency, because dissipation exceeds production. Although we are not sure if this elevation of ϕ_h is physically realistic, it does not impact our test results for this wave-breaking model (Figure 2.8).

To assess the reliability of the approximate solution [Eq. (2.17)] used in the calculation of model ϕ_h, numerical solution of Eq. (2.16) is investigated with a fourth-order finite difference method (*Kierzenka and Shampine*, 2001), after substituting ϕ_m with an expression derived from Eqs. (2.18b-c), and rewriting ζ as $e^{-\kappa y} \cdot z_0/L$. Figure 2.6b shows an example of the numerically solved $q^* = q/u_*$ when $z_0/L = -0.2$, along with solutions from Eq. (2.17), from the neutral limit (*Craig*, 1996) and from the classical super-equilibrium SMC without wave breaking. The approximate solution exactly coincides with the numerical solution near the surface, but gently converges to the classical solution at depth. Compared to the neutral solution of *Craig* (1996), the approximate solution agrees better with the numerical solution as buoyancy gradually becomes important at depth, and its advantage is even more prominent at larger $|z_0/L|$. Since the subtle differences between the numerical and approximate solution are found to have negligible impact on the resulting ϕ_h, and, given that the major parameter values observed here have $|z_0/L|$ smaller than 0.2, we may conclude that Eq. (2.17) is a sound approximation for the TKE under breaking waves, as modeled by Eq. (2.13). Therefore, the temperature scaling ϕ_h based on Eq. (2.17) should largely reflect the surface layer temperature predicted by the

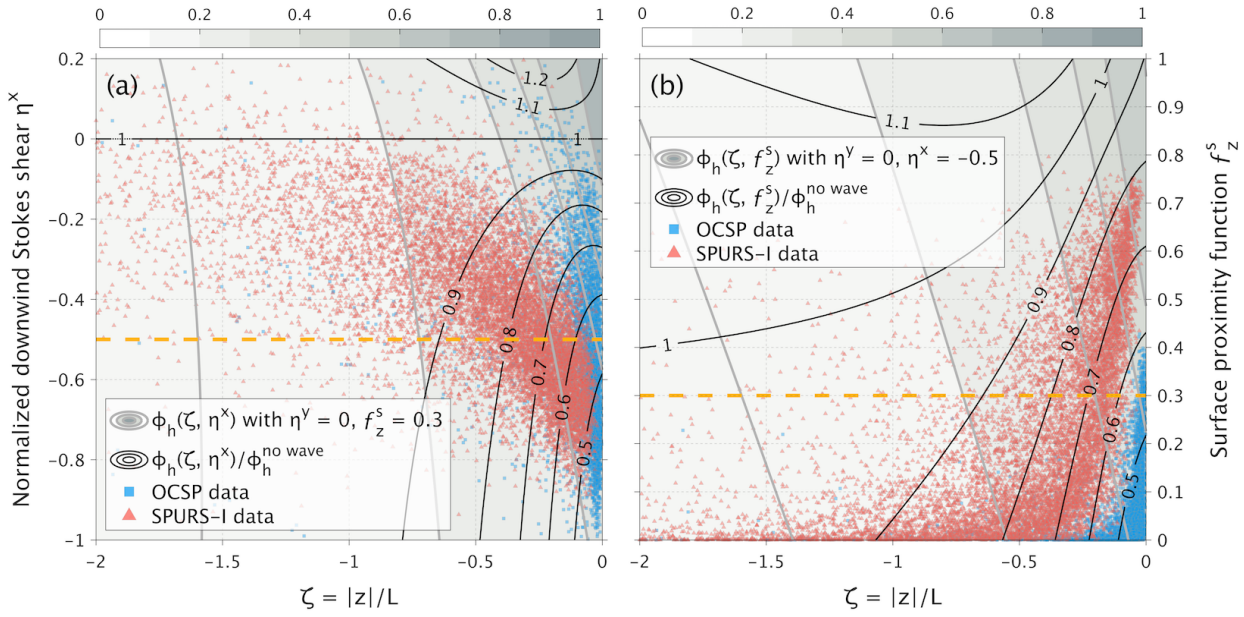

Figure 2.7: Dimensionless temperature gradient ϕ_h predicted by the super-equilibrium Langmuir turbulence model (*Harcourt*, 2015, $\ell = \kappa|z|$). (a) Variations of the model-derived ϕ_h as a function of ζ and η^x when the normalized crosswind Stokes shear $\eta^y = 0$ and the surface proximity function $f_z^s = 0.3$. (b) Variations of the model-derived ϕ_h as a function of ζ and f_z^s when $\eta^y = 0$ and $\eta^x = -0.5$. In both (a) and (b), color-filled contours show the values of ϕ_h (0.15, 0.2, 0.3, 0.4, 0.5, 0.7) predicted; black isolines show the ratios of the model-derived ϕ_h to those from the classical super-equilibrium SMC (*Kantha and Clayson*, 1994) with no wave effects; yellow dash line shows the constant parameter value selected in the other panel. Observed parameter values at OCSP (blue) and SPURS-I (red) are overlaid.

full model of *Craig and Banner* (1994).

2.3.2 *Similarity relations in Langmuir turbulence model*

Over the course of continuous efforts to include Langmuir turbulence in classical SMCs, until the recent model by *Harcourt* (2015), a series of modifications have been proposed: Governing equations are extended to incorporate the CL vortex force and other related terms (*D'Alessio et al.*, 1998; *Kantha and Clayson*, 2004); closure assumptions are generalized to have consistent dependency on Stokes drift (*Harcourt*, 2013, 2015). As a result, the

modified TKE equation has extra production by the CL vortex force, directly elevating the vertical TKE ($\overline{w'w'}$). In addition, the inhomogeneous closures for the pressure-strain rate and pressure-scalar gradient correlations (*Harcourt*, 2015) also redirect part of the CL vortex production into the crosswind direction to rectify the predictions of second-order statistics. Meanwhile, the inclusion of the CL vortex production in the algebraic Reynolds stress model (ARSM) naturally entails a fundamentally different down-gradient assumption for momentum fluxes:

$$\overline{w'\boldsymbol{u}'} = -K_m \frac{\partial \overline{\boldsymbol{u}}}{\partial z} - K_m^s \frac{\partial \boldsymbol{u}^s}{\partial z}, \tag{2.19}$$

where K_m is the conventional eddy viscosity, and K_m^s is a Stokes eddy coefficient. A similar assumption for momentum flux in the KPP scheme is also adopted in *McWilliams et al.* (2012).

With these and some other adjustments to parameterize Langmuir turbulence, the model of *Harcourt* (2015) showed promising agreements with LES results. Here we start from the super-equilibrium version of *Harcourt* (2015), with the goal to attain similarity relations in a Langmuir turbulence-affected surface layer, provided the extra physics of

Langmuir turbulence is properly represented in these model equations:

$$\frac{q^3}{B_1\ell} = -\overline{w'u'}\frac{\partial \overline{u}}{\partial z} - \overline{w'u'}\frac{\partial u^s}{\partial z} + \alpha g\overline{w'\theta'}, \tag{2.20a}$$

$$\overline{u'u'} = \frac{q^2}{3}(1-\frac{6A_1}{B_1}) - \frac{6A_1\ell}{q}(\overline{w'u'}\frac{\partial u^s}{\partial z}f_z^s\cos^2\gamma + \overline{w'u'}\frac{\partial \overline{u}}{\partial z}), \tag{2.20b}$$

$$\overline{v'v'} = \frac{q^2}{3}(1-\frac{6A_1}{B_1}) - \frac{6A_1\ell}{q}\overline{w'u'}\frac{\partial u^s}{\partial z}f_z^s\sin^2\gamma, \tag{2.20c}$$

$$\overline{w'w'} = \frac{q^2}{3}(1-\frac{6A_1}{B_1}) - \frac{6A_1\ell}{q}\Big[-\alpha g\overline{w'\theta'} + (1-f_z^s)\overline{w'u'}\frac{\partial u^s}{\partial z}\Big], \tag{2.20d}$$

$$\overline{w'u'} = \frac{-3A_1\ell}{q}\Big[(\overline{w'w'} - C_1q^2)\frac{\partial \overline{u}}{\partial z} - \alpha g\overline{u'\theta'} + (1-f_z^s)(\overline{u'u'}\frac{\partial u^s}{\partial z} + \overline{u'v'}\frac{\partial v^s}{\partial z}) - \Pi_{13}^{(\mathrm{LCB})}\Big], \tag{2.20e}$$

$$0 = \frac{-3A_1\ell}{q}\Big[(\overline{w'w'} - C_1q^2)\frac{\partial \overline{v}}{\partial z} - \alpha g\overline{v'\theta'} + (1-f_z^s)(\overline{v'v'}\frac{\partial v^s}{\partial z} + \overline{u'v'}\frac{\partial u^s}{\partial z}) - \Pi_{23}^{(\mathrm{LCB})}\Big], \tag{2.20f}$$

$$\overline{u'v'} = \frac{-3A_1\ell}{q}\Big[\overline{w'u'}\frac{\partial \overline{v}}{\partial z} - 2\overline{w'u'}\frac{\partial u^s}{\partial z}f_z^s\cos\gamma\sin\gamma\Big], \tag{2.20g}$$

$$\overline{u'\theta'} = \frac{-3A_2\ell}{q}\Big[(1-C_2)\overline{w'\theta'}\frac{\partial \overline{u}}{\partial z} + \overline{w'u'}\frac{\partial \overline{\theta}}{\partial z}\Big], \tag{2.20h}$$

$$\overline{v'\theta'} = \frac{-3A_2\ell}{q}(1-C_2)\overline{w'\theta'}\frac{\partial \overline{v}}{\partial z}, \tag{2.20i}$$

$$\overline{w'\theta'} = \frac{-3A_2\ell}{q}\Big[\overline{w'w'}\frac{\partial \overline{\theta}}{\partial z} - (1-C_3)\alpha g\overline{\theta'\theta'} + (1-f_z^s)(\overline{u'\theta'}\frac{\partial u^s}{\partial z} + \overline{v'\theta'}\frac{\partial v^s}{\partial z})\Big], \tag{2.20j}$$

$$\overline{\theta'\theta'} = \frac{-B_2\ell}{q}\overline{w'\theta'}\frac{\partial \overline{\theta}}{\partial z}. \tag{2.20k}$$

In the equations above, variables inherited from the classical SMC represent the same quantities as in Appendix 2.C, to which are added u^s and v^s, Stokes drift in the downwind and crosswind directions, respectively. Angle γ denotes the orientation of the Langmuir cells (*Van Roekel et al.*, 2012) relative to the y-coordinate in a clockwise sense; $f_z^s = 1 + \tanh(0.25z/l^s)$ is a surface proximity function that decays with depth with a characteristic

length scale

$$l^s = \frac{\int_{z_{\mathrm{PCL}^+}}^{0} \ell \cdot (-\overline{w'u'}\frac{\partial u^s}{\partial z})dz}{\int_{z_{\mathrm{PCL}^+}}^{0} -\overline{w'u'}\frac{\partial u^s}{\partial z}dz}, \tag{2.21}$$

where $|z_{\mathrm{PCL}^+}|$ is the deepest depth at which the CL vortex production ($-\overline{w'u'}\frac{\partial u^s}{\partial z}$) still remains positive. $\Pi_{ij}^{(\mathrm{LCB})}$ is the balancing component of the rapid pressure-strain rate closure designed to cancel the explicit dependence of K_m^s on the misalignment angle γ. A detailed expression for $\Pi_{ij}^{(\mathrm{LCB})}$ is provided in *Harcourt* (2015).

Note that the same boundary layer approximations have been applied in Eqs. (2.20), and the x-coordinate is still chosen to align with the surface wind stress, though the surface wave direction may be misaligned. In the case of nonzero crosswind Stokes drift v^s, although crosswind stress $\overline{w'v'}$ is zero, $\partial\overline{v}/\partial z$ is not necessarily zero because the flux proportional to the Stokes shear must be compensated by that proportional to the Eulerian shear [see Eq. (2.19)]. Thus, covariance $\overline{w'v'}$, $\overline{u'v'}$, $\overline{v'\theta'}$ are retained in Eqs. (2.20). In the process of non-dimensionalization, the downwind and crosswind components of Stokes shear can be scaled by introducing Stokes stability parameters

$$\eta^x = -\hat{\boldsymbol{\tau}}_w \cdot \frac{\partial \boldsymbol{u}^s}{\partial z} \Big/ \frac{u_*}{\kappa|z|}, \tag{2.22a}$$

$$\eta^y = -\hat{\boldsymbol{z}} \cdot (\hat{\boldsymbol{\tau}}_w \times \frac{\partial \boldsymbol{u}^s}{\partial z}) \Big/ \frac{u_*}{\kappa|z|}, \tag{2.22b}$$

where $\hat{\boldsymbol{\tau}}_w$ is the unit vector in the direction of surface wind stress and $\hat{\boldsymbol{z}}$ is the unit vector of z coordinate. Note that η^x shares the sign convention of forcing parameter ζ, not of dimensionless shear ϕ_m. Following the procedure in Appendix 2.C, equations (2.20) are

non-dimensionalized and reduced to

$$q^{*3} = B_1 \ell^* (\phi_m^x - \zeta - \eta^x), \tag{2.23a}$$

$$\frac{1}{3A_1 q^* \ell^*} = \phi_m^x \left[r - C_1 - \frac{\big(6A_1 + 3A_2(1-C_2)\big)\zeta \ell^*}{q^{*3}} - \frac{12 A_1 \tilde{\eta}^x \ell^*}{q^{*3}} \right] - \phi_h \left[\frac{3A_2 \zeta \ell^*}{q^{*3}} \right] - \phi_m^y \left[\frac{3A_1 \tilde{\eta}^y \ell^*}{q^{*3}} \right] - \tilde{\eta}^x r, \tag{2.23b}$$

$$\frac{1}{3A_2 q^* \ell^*} = \phi_h \left[r - \frac{\big(6A_1 + B_2(1-C_3)\big)\zeta \ell^*}{q^{*3}} - \frac{(6A_1 + 3A_2)\tilde{\eta}^x \ell^*}{q^{*3}} \right] - \phi_m^x \left[\frac{3A_2(1-C_2)\tilde{\eta}^x \ell^*}{q^{*3}} \right] - \phi_m^y \left[\frac{3A_2(1-C_2)\tilde{\eta}^y \ell^*}{q^{*3}} \right], \tag{2.23c}$$

$$0 = \phi_m^y \left[r - C_1 - \frac{\big(6A_1 + 3A_2(1-C_2)\big)\zeta \ell^*}{q^{*3}} - \frac{9 A_1 \tilde{\eta}^x \ell^*}{q^{*3}} \right] - \tilde{\eta}^y r, \tag{2.23d}$$

where ϕ_m^x and ϕ_m^y are dimensionless gradients of mean Eulerian velocity in the downwind ($\overline{u}$) and crosswind ($\overline{v}$) directions, and the prefactor $(1 - f_z^s)$ has been absorbed into the Stokes stability parameters in Eqs. (2.23b-d), so that $\tilde{\eta}^x = (1 - f_z^s)\eta^x$, $\tilde{\eta}^y = (1 - f_z^s)\eta^y$.

In the surface layer, we use the classical mixing length argument that $\ell^* \equiv \ell / \kappa |z| = 1$. A more dynamical determination of the length scale will be discussed later in Section 2.3.3. Making use of the same algorithm, we solve Eqs. (2.23) to express ϕ_h as a function of ζ, η^x, η^y, and f_z^s. For situations when the wind and waves are aligned ($\eta^y = 0$), a map of the model-derived ϕ_h in ζ and η^x space (Figure 2.7a) with $f_z^s = 0.3$, which is a typical value of estimated f_z^s from observations, shows this model predicts a smaller temperature scaling ϕ_h than the classical super-equilibrium SMC (or MOST), when the Stokes drift shear is in downwind direction ($\eta^x < 0$). The reduction of ϕ_h generally increases as the magnitude of η^x gets larger, but the modification of ϕ_h by Langmuir turbulence only seems to be significant when convection is weak. The smaller ϕ_h in this model is physically related to the enhanced vertical TKE and the additional contribution to vertical heat flux from horizontal heat flux [Eqs. (2.20)d, (2.20)j], both due to the CL vortex force. This model also predicts larger ϕ_h than the classical super-equilibrium SMC (or MOST) when $\eta^x > 0$, implying intensified unstable thermal gradient when Stokes drift is in

the opposite direction of the wind, however, this rarely occurs. Note that the model prediction of ϕ_h is also set by the surface proximity function, and such dependence of ϕ_h on f_z^s when $\eta^x = -0.5$ is demonstrated in Figure 2.7b. As the surface proximity function effects a local redistribution between components of Reynolds stress production, higher values normally decrease the contribution of the CL vortex production to the vertical TKE and vertical fluxes, leading to a weaker reduction of ϕ_h by Langmuir turbulence. Similarly, the model-derived ϕ_h is sensitive to f_z^s values in the weakly convective regime.

2.3.3 *Comparison of model results with observations*

The analyses of model behaviors under idealized forcing (Figure 2.6a and 2.7) clearly show that both surface wave breaking and Langmuir turbulence can modify the temperature scaling, and the temperature gradient is additionally regulated by wave forcing parameters. As a further comparison with observations needs realistic wave forcing parameters, we estimate them from available observations.

The calculation of ζ assumes the roughness length scale $z_0 = 0.6H_s$ (*Terray et al.*, 1996), where the coefficient 0.6 is admittedly uncertain, but the proportionality with H_s is supported by previous studies (*Duncan*, 1981; *Zippel et al.*, 2018). Stokes stability parameters η^x and η^y are specified by the vertical shear of Stokes drift according to Eqs. (2.22). The surface proximity function f_z^s has a decay scale l^s that is not easily quantifiable. Hence in Eq. (2.21), we use a linear profile of momentum flux, $\overline{w'u'} = -u_*^2(1 + z/H)$, and assume a parabolic profile of length scale, $\ell = \kappa|z|(1 + z/H)$, in the OSBL. Typical values for l^s are about 0.3 m and 0.7 m at OCSP and SPURS-I, respectively, generally smaller than the effective e-folding depth scale [approximately $0.14U_{10}^2/g$, per *Harcourt and D'Asaro* (2008)] of equilibrium waves.

The computed forcing parameters are laid out in Figure 2.6a and 2.7. On the ζ axis, most of the data are in the forced convection regime, and the data from SPURS-I span a wider range than OCSP. On the ζ axis, measurements mostly occurred within a distance

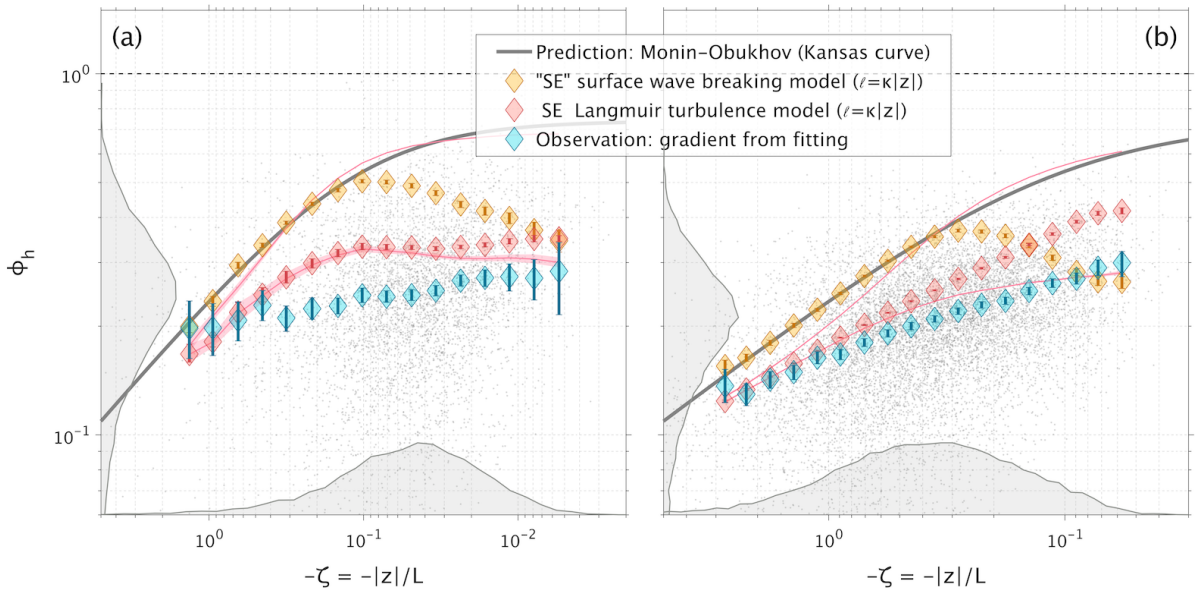

Figure 2.8: Comparison of the super-equilibrium (SE) model predictions of dimensionless gradient ϕ_h with observations at (a) OCSP and (b) SPURS-I. Only data from quasi-steady periods are presented. Model predictions are evaluated from Eqs. (2.18) and Eqs. (2.23), using realistic forcing parameters. Observations of ϕ_h (gray dots) are the same as those in Figure 2.5. Probability density functions of the observed values of $\log_{10}(\phi_h)$ and $\log_{10}(-\zeta)$ are shown by gray shadings on the left and bottom. Diamonds represent bin averages of observations and model predictions (see legend and text). The bin averages of observations also include some negative values (0.35% of total), though not shown in the log-log plot. Red lines are averages of predictions from the SE Langmuir turbulence model (*Harcourt*, 2015, $\ell = \kappa|z|$) with constant surface proximity function $f_z^s = 1$ (upper) and $f_z^s = 0$ (lower). Confidence intervals (95%) of bin averages are indicated by error bars and shadings around red lines. Empirical relationship [Eq. (2.3b)] from the Kansas experiment (*Businger et al.*, 1971) is displayed as the thick gray curve.

of $7z_0$ below the wave-breaking layer. Though highly scattered, linear relationships with varying slopes (z_0/L) between ζ and ξ stand out prominently, owing to the nearly constant Obukhov length L in unstable conditions. In general, OCSP has smaller z_0/L values than SPURS-I (Figure 2.6a). The Stokes drift shear is mostly in the destabilizing downwind direction, indicated by negative η^x and much smaller η^y (not shown). Given a similar depth for the shallowest sensor at both sites, the higher tip of SPURS-I data in Figure 2.7b suggests relatively larger decay lengths for f_z^s there.

Model predictions of ϕ_h in the case of wave breaking and Langmuir turbulence are computed with realistic forcing parameters. The aggregated results are displayed in Figure 2.8, together with the observations from Section 2.2. The "super-equilibrium" wave breaking model basically gives ϕ_h similar to the Kansas curve, except at relatively small $|\zeta|$. This is consistent with the example given in Figure 2.6c, where ϕ_h are integrated to show the difference between temperature profiles predicted by the "super-equilibrium" wave breaking model and by MOST. The peak in the model-derived ϕ_h curve occurs because the observed forcing parameters (ζ, ξ) go through a ridge in the ϕ_h contours (Figure 2.7a). Different constants in the roughness length formula, from 0.3 to 1.2, have been tested, yet the resulting ϕ_h curves have essentially the same shape, although the location of inflection differs a bit. In all, it seems that the simplified wave-breaking model predicts reduced ϕ_h only in near-surface region, where $|\zeta|$ is relatively small. Considering the ϕ_h reduction is observed over a broader ζ range, there is insufficient evidence to support the first hypothesis that surface wave breaking is the main cause of the observed weak temperature gradients.

For the super-equilibrium Langmuir turbulence model, predictions generally follow the trend of observations. At large $|\zeta|$, the model agrees well with observations, but as $|\zeta|$ becomes smaller, its prediction gradually deviates from observations, shifting toward the Kansas curve. Considering uncertainties in the estimate of the surface proximity function, we test the model with 2 bounding values, 0 and 1, of f_z^s. The test with $f_z^s = 1$, effectively a super-equilibrium version of *Kantha and Clayson* (2004), gives almost the

same prediction as the Kansas curve. On the other hand, the test with $f_z^s = 0$, a slightly modified super-equilibrium version of *Harcourt* (2013), gives result that roughly matches observations, except some deviations at OCSP. These two tests enclose all the variations of ϕ_h caused by the uncertainties of f_z^s in this model. Their convergence at large negative values of ζ is consistent with the fact that the variation of f_z^s does not change ϕ_h much at larger $|\zeta|$ (Figure 2.7b). In all, the simplified Langmuir turbulence model can predict reduced ϕ_h over a ζ range similar to that observed, and makes robust ϕ_h predictions in relatively strong unstable conditions. However, its predictions in relatively weak unstable conditions are obscured by the uncertainties of the f_z^s estimation.

Previous LES studies on Langmuir turbulence have reported near-surface turbulent length scales different than $\kappa|z|$ (e.g., *Harcourt*, 2013). The fact that we prescribed $\ell = \kappa|z|$ in Eqs. (2.23) may alter the super-equilibrium model's predictive power, given that its full version uses a prognostic equation to determine ℓ. To further explore the possible impact of varying ℓ^*, we add a $q^2\ell$ equation to the super-equilibrium Langmuir model [following *Kantha and Clayson* (2004)],

$$-\frac{\partial}{\partial z}\left[q\ell S_\ell \frac{\partial q^2\ell}{\partial z}\right] = E_1\ell(-\overline{w'u'}\frac{\partial \overline{u}}{\partial z}) + E_6\ell(-\overline{w'u'}\frac{\partial u^s}{\partial z}) + E_3\ell(\alpha g\overline{w'\theta'}) - \frac{E_2 q^3}{B_1}\left[1 + \frac{E_4\ell^2}{\kappa^2|z|^2}\right]. \tag{2.24}$$

This equation is solely patterned after the full TKE equation but with tendency and advection terms omitted. On the right-hand side of Eq. (2.24) are shear production, CL vortex production, buoyancy production (destruction) and dissipation of $q^2\ell$, respectively. A wall-proximity term with coefficient E_4 is traditionally lumped together with dissipation to ensure $\ell = \kappa|z|$ near a bounding surface (*Mellor and Yamada*, 1982). The term on the left-hand side of Eq. (2.24) represents down-the-gradient diffusion of $q^2\ell$, and it is not negligible in the surface layer as ℓ varies with depth. This departure from strict super-equilibrium assumptions is necessary to retain the law-of-the-wall asymptotic behavior for vanishing Stokes drift when including the length scale equation (*Kantha and Clayson*, 2004). For the values of constants in Eq. (2.24), *Mellor and Yamada* (1982) recommended

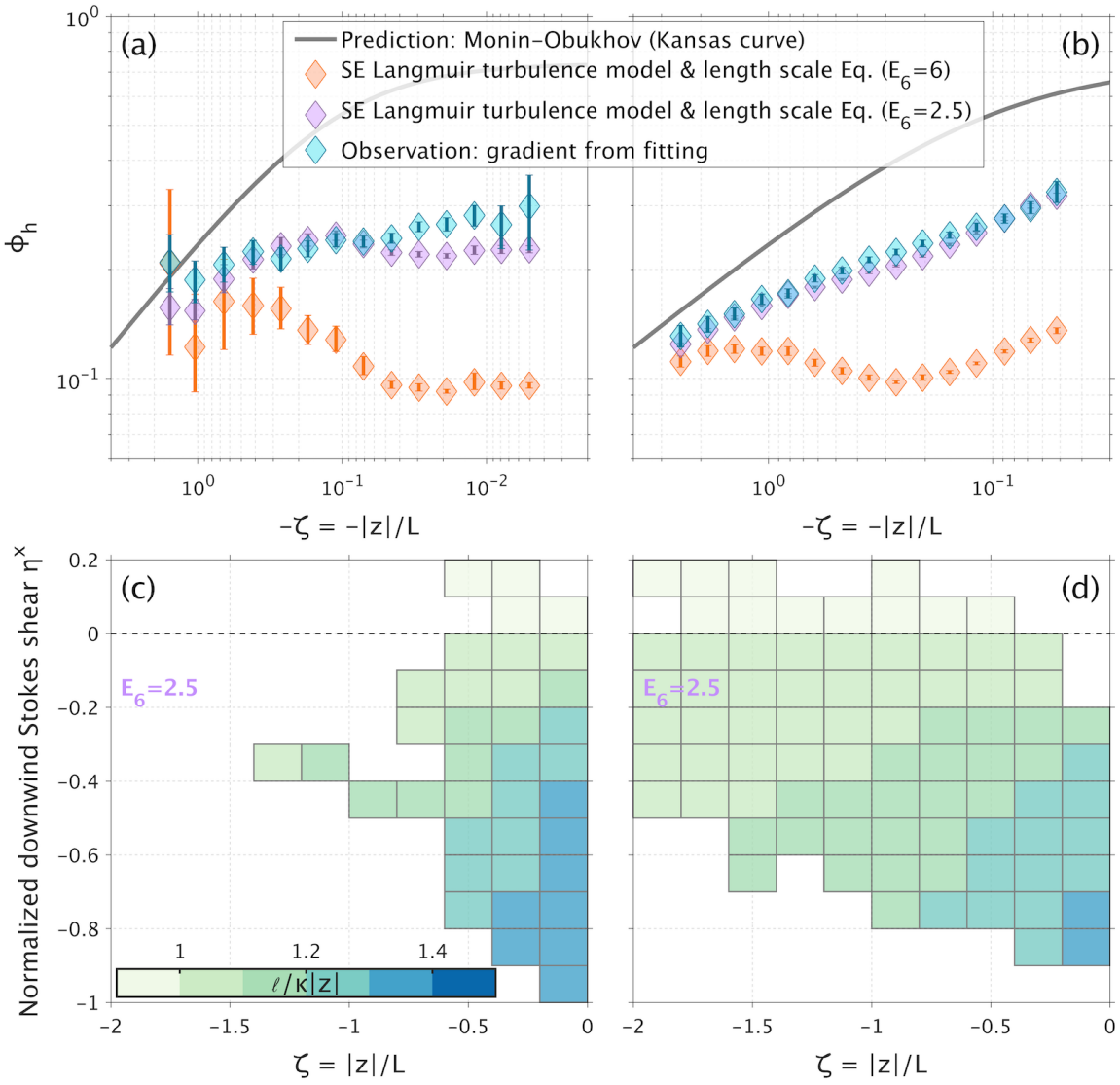

Figure 2.9: (a) Comparison of Langmuir turbulence model predictions of ϕ_h with observations at OCSP. The model here uses dynamical length scale equation (2.24), rather than assuming $\ell = \kappa|z|$. Observations and MOST predictions of ϕ_h are copied from Figure 2.8. Orange diamonds are averages of model predictions with $E_6 = 6$, as suggested by *Harcourt* (2015). Purple diamonds show averages of predictions from the same model, but tuning E_6 to 2.5 to best match observations. (b) Same as (a) but use data from SPURS-I. (c) Variations of ℓ^* (length scale ℓ normalized by $\kappa|z|$) at OCSP as a function of ζ and η^x, as predicted by this Langmuir turbulence model with $E_6 = 2.5$. Predictions of ℓ^* are bin averaged and shown by the color of grids. Bins with less than 5 data points are ignored. (d) Same as (c) but use data from SPURS-I.

$S_\ell = 0.2$, $E_1 = E_3 = 1.8$, $E_2 = 1$, $E_4 = 1.33$. Various values have been suggested for E_6 (*Kantha and Clayson*, 2004; *Carniel et al.*, 2005; *Kantha et al.*, 2010), and *Harcourt* (2015) settled at $E_6 = 6$. Applying the same scaling arguments as those in Section 2.3.2, we can non-dimensionalize Eq. (2.24) to

$$-B_1 S_\ell q^{*3}(\kappa\ell^*)^2 = B_1\ell^*(E_1\phi_m - E_3\zeta - E_6\eta^x) - E_2 q^{*3}(1 + E_4\ell^{*2}). \tag{2.25}$$

Supplementing Eqs. (2.23) with Eq. (2.25), we can solve for ϕ_h without invoking the assumption for ℓ^*. While we retain the standard model constants following *Mellor and Yamada* (1982), we find the resultant ϕ_h sensitive to the coefficient E_6 that regulates the CL vortex production of $q^2\ell$. The suggested value ($E_6 = 6$) actually gives too small ϕ_h over most of the observed ζ range (Figure 2.9a and 2.9b), due to seemingly too large ℓ^* overall (maximum is about 3). The optimal value of E_6 that produces results most similar to observations is about 2.5. In this simplified model, the necessity of using a E_6 different than that of the full model (*Harcourt*, 2015) may be linked to the negligence of turbulence transport in the TKE equation and the assumption of weak depth dependence of q^2 in the $q^2\ell$ equation. Other possible reasons may be rooted in the closure assumptions for the pressure-strain rate correlations, for which alternative formulations have been proposed by *Pearson et al.* (2019).

With $E_6 = 2.5$, the corresponding ℓ^* variations produced by tuning for model-observation agreement are shown in Figure 2.9c and 2.9d. When the Stokes drift shear is downwind, the model predicts a length scale greater than $\kappa|z|$, and the enhancement of ℓ^* is more profound in weakly unstable conditions, with ℓ^* approaching 1.5 in nearly neutral conditions. In strongly unstable conditions, the influence of Stokes drift declines, and ℓ reverts to the classical $\kappa|z|$ scaling. These are broadly consistent with the fact that Langmuir cells are indeed large scale structures, and in line with the speculation that vigorous convection out-competes Langmuir turbulence in strong cooling events (*Li and Fox-Kemper*, 2017). Despite the empiricism involved here, the success of this enhanced super-equilibrium Langmuir model in reproducing the mean scaling behavior of obser-

vations, and the reasonable underlying length scale variations, both serve to increase confidence in Langmuir turbulence as the major process responsible for reducing the near-surface temperature gradients. Note that our results for Langmuir model generally contradict previous findings from tuning model to LES solutions (*Harcourt*, 2013, 2015). Here we need to either use fixed length scale ($\kappa|z|$) and turn off surface proximity function ($f_z^s = 0$), or use dynamical determination of length scale with a different E_6 constant and retain default surface proximity function to achieve better consistency with observations.

2.4 *Summary*

In this study, we find that in the unstable oceanic surface layer, MOST fails to quantitatively predict the mean thermal stratification from surface fluxes. Observations consistently present temperature gradients smaller than those suggested by MOST. As the thermal diffusivity K_h is related to the dimensionless temperature gradient ϕ_h through Eq. (2.4), smaller ϕ_h also means larger K_h and more efficient vertical heat transport.

To further investigate the cause of the theory-observation discrepancies, two hypotheses are considered. The first one attributes the weak temperature gradients to the effects of surface wave breaking, while the second one considers Langmuir turbulence as the major contributor. Although imperfect, PBL models that include the effects of surface wave breaking (*Craig and Banner*, 1994) and Langmuir turbulence (*Harcourt*, 2015) are taken to represent these two hypotheses, respectively. Each is tested in the framework of super-equilibrium SMC ("level 2" in *Mellor and Yamada*, 1982), where model equations are reduced to give predictions of ϕ_h. It appears that the simplified surface wave-breaking model can only give results partially matching observations in weakly unstable conditions. In contrast, predictions from the simplified Langmuir turbulence model are very similar to observations across a broad stability range. When supplemented by a length scale equation, the simplified Langmuir turbulence model can quantitatively reproduce the mean scaling behavior of observations if a model constant in the length scale equation is appropriately tuned. Hence we conclude first, that there is not enough evidence to

support the surface wave breaking as the main cause of the weak temperature gradients observed; second, that the observed weak temperature gradients are more likely due to Langmuir turbulence.

We have evaluated several approaches to combine the wave breaking and Langmuir turbulence parameterizations in one model, but none of these combined models gives better results than the Langmuir model alone. However, it is of significant concern that the down-gradient diffusion assumption for TKE flux that leads to the S_q term in Eq. (2.13) is of uncertain validity when the CL vortex force interacts with the elevated TKE from wave breaking [see for example, *Sullivan et al.* (2007)]. These are issues that merit much more detailed study.

In the end, we allow that the data here may be insufficient to constrain all of the parameters in the models examined, and the conclusion of our hypotheses testing is by no means definitive. However, a combination of the data shown here and other observations will provide powerful constraints on models and theory designed to gain a physically realistic and quantitatively predictive understanding of the upper ocean boundary layer.

APPENDICES

Appendix 2.A Stokes drift

The Stokes drift velocity in deep water (with dispersion relation $\omega^2 = gk$) is calculated by integrating the directional surface wave spectrum $S(f,\lambda)$ (*Kenyon*, 1969),

$$\boldsymbol{u}^s(z) = 4\pi \int_0^\infty \int_{-\pi}^{\pi} f \cdot \boldsymbol{k} \cdot S(f,\lambda) \cdot e^{2kz} \cdot d\lambda df, \tag{2.26}$$

where $\boldsymbol{k} = k \cdot \hat{\boldsymbol{k}} = k \cdot (-\sin\lambda \cdot \hat{\boldsymbol{x}} - \cos\lambda \cdot \hat{\boldsymbol{y}})$ is the horizontal wavenumber of surface waves; $\hat{\boldsymbol{x}}, \hat{\boldsymbol{y}}$ are unit vectors directing East and North; λ is the direction the wave is coming from (clockwise from true North); f and ω are the wave frequency in hertz and radian. The directional wave spectrum $S(f,\lambda)$ is estimated from archived records as

$$S(f,\lambda) = \frac{E(f)}{\pi}\Big(\frac{1}{2} + a_1\cos\lambda + b_1\sin\lambda + a_2\cos 2\lambda + b_2\sin 2\lambda\Big), \tag{2.27}$$

in which a_1, b_1, a_2, b_2 are the normalized coefficients of directional Fourier series, and $E(f)$ is the non-directional wave spectrum. Therefore, the east and north components of the Stokes drift velocity are

$$u^s = \frac{-16\pi^3}{g} \int_0^\infty f^3 E(f) \cdot e^{8\pi^2 f^2 z/g} \cdot b_1 \cdot df, \tag{2.28a}$$

$$v^s = \frac{-16\pi^3}{g} \int_0^\infty f^3 E(f) \cdot e^{8\pi^2 f^2 z/g} \cdot a_1 \cdot df. \tag{2.28b}$$

The resolved part of Stokes drift at OCSP (SPURS-I) is obtained by summing over the range from 0.025 (0.0325) to 0.58 (0.485) Hz with frequency bandwidths varying from 0.005 (0.005) Hz at low frequencies to 0.01 (0.02) Hz at high frequencies. For the unresolved part beyond cutoff frequency f_c, we use an analytical form that is consistent with the Phillips spectrum (*Harcourt and D'Asaro*, 2008; *Breivik et al.*, 2014),

$$S_{hf} = S(f_c,\lambda) \cdot (f/f_c)^{-5}, \tag{2.29}$$

in which the high-frequency tail is assumed to have the same directional distribution as the last resolved band. Then we can write the contribution from the spectral tail as

$$\boldsymbol{u}^s_{hf}(z) = \frac{-16\pi^3 f_c^5}{g} \cdot \left[\frac{e^{-\mu f_c^2}}{f_c} - \sqrt{\mu\pi} \cdot \mathrm{erfc}\left(f_c\sqrt{\mu}\right) \right] \cdot E(f_c) \cdot \left(b_1(f_c) \cdot \hat{\boldsymbol{x}} + a_1(f_c) \cdot \hat{\boldsymbol{y}} \right), \quad (2.30)$$

with $\mu = -8\pi^2 z/g$. The vertical shear of the Stokes drift is computed by adding the vertical derivatives of the resolved part and the tail contribution, thus

$$\begin{aligned} \frac{\partial \boldsymbol{u}^s}{\partial z}(z) = & \frac{-128\pi^5}{g^2} \int_0^{f_c} f^5 E(f) \cdot e^{8\pi^2 f^2 z/g} \cdot (b_1 \cdot \hat{\boldsymbol{x}} + a_1 \cdot \hat{\boldsymbol{y}}) \cdot df - \\ & \frac{16\pi^3 f_c^5}{g} \cdot \sqrt{\frac{-2\pi^3}{gz}} \cdot \mathrm{erfc}\left(f_c\sqrt{\mu}\right) \cdot E(f_c) \cdot \left(b_1(f_c) \cdot \hat{\boldsymbol{x}} + a_1(f_c) \cdot \hat{\boldsymbol{y}} \right). \end{aligned} \quad (2.31)$$

Appendix 2.B Calibration of salinity in SPURS-I data set

Although salinity profiles are not directly used to test the classical scaling, they are still important in setting the upper ocean stratification. Unfortunately, salinity measurements from the SPURS-I mooring have shown consistently unrealistic variations in the OSBL. This is most evident during nighttime convection, as exampled by the raw profiles in Figure 2.10. The upper ocean salinity variation is so large that it dominates the density structure, while the nearly homogeneous temperature profile indicates that the convective plume has resulted in a well-mixed layer. Therefore we think these salinity jumps are probably due to bio-fouling or instrumental drift. To get a reasonable estimate of the boundary layer depth, it is necessary to adjust the raw salinity profiles to make the temperature-salinity structures consistent with expectations from convective mixing.

The method for salinity correction is to limit the range of salinity variation within the convective layer, defined as the extent to which the temperature exceeds a 0.006 °C difference from the averaged temperature in upper 3 m, while still preserving the profile shape. Three steps are involved in this adjustment. First, the salinity offset for each sensor in the convective layer is estimated once per night, in reference to the deepest, most well-mixed temperature profile with no rain event in the past 3 hours. The maximum salinity

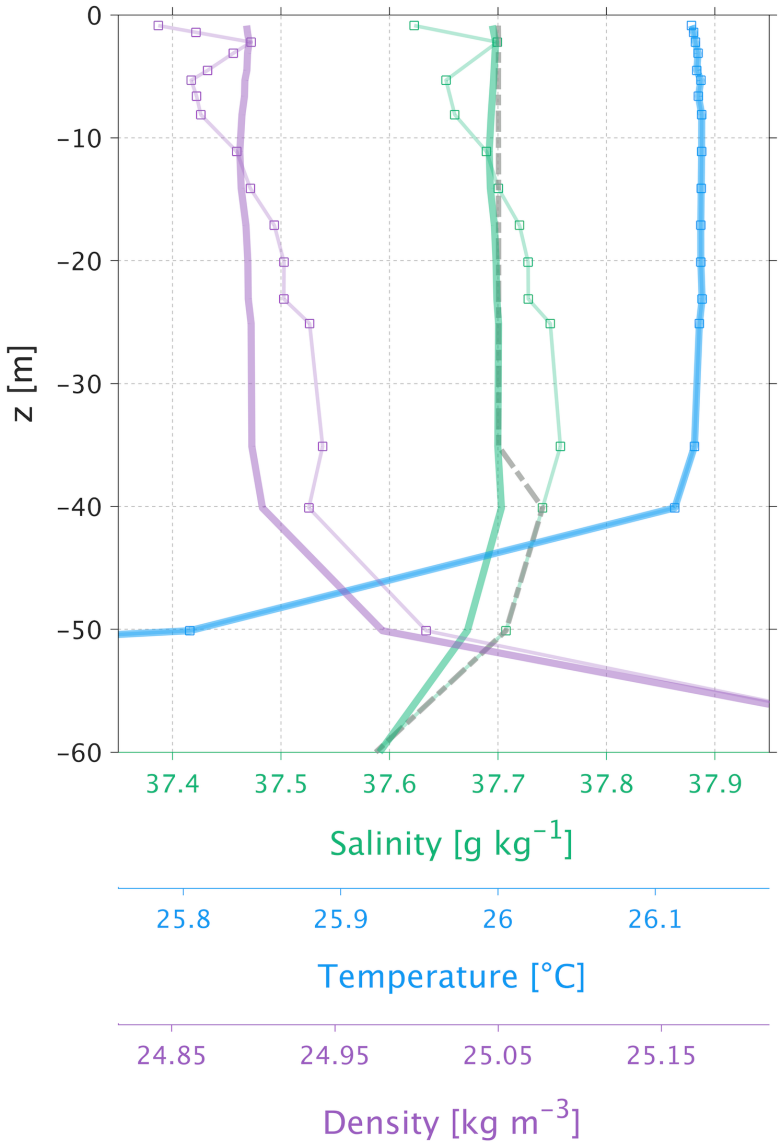

Figure 2.10: Changes in salinity (green), temperature (blue), and density (purple) before (thin line with squares) and after (thick line) the salinity correction in the SPURS-I dataset. Profiles are taken from local time 22:30, August 4, 2013. Dash dotted gray line shows the nightly adjusted profile used to estimate sensor drift curves.

variation (relative to the mean) allowed in the convective layer, $\left|\Delta\overline{S}\right|_m$, is determined by the ratio between the magnitude of near-surface salt and heat fluxes, i.e.,

$$\frac{\left|\Delta\overline{S}\right|_m}{\left|\Delta\overline{\theta}\right|_{m,\,obs}} = \frac{\left|\overline{w'S'}|_0\right|}{\left|\overline{w'\theta'}|_0\right|}, \tag{2.32}$$

where $\left|\Delta\overline{\theta}\right|_{m,\,obs}$ is the maximum of the measured temperature variation in the convective layer. The ratio of the maximum allowed, $\left|\Delta\overline{S}\right|_m$ to the maximum measured, $\left|\Delta\overline{S}\right|_{m,\,obs}$, is used to downscale the salinity variation within the convective layer (Figure 2.10). For each sensor adjusted, the salinity offset is recorded. Second, to avoid over-correction, we only use the slow-varying drift curves extracted from the time series of nightly offsets. For sensors with adequate offset estimates, a 29-point median filter is used (Figure 2.11). For sensors with only a few nightly offsets, a linear fit is used (not shown). Finally, to ensure the continuity of corrections, we interpolate these drift curves to hourly intervals before applying them to the raw salinity profiles. An example of the corrected salinity profile and the resulting density profile is shown in Figure 2.10. The fact that almost all of the individual offset estimates are within the $\pm$ 0.03 g kg^{-1} deviation bands of drift curves indicates the calibrations are well-constrained.

Appendix 2.C Similarity relations in the classical Second Moment Closure

Here we show that the surface layer similarity relations can be independently derived from the classical super-equilibrium SMC (*Kantha and Clayson*, 1994), following the procedure presented by *Mellor* (1973). A different derivation can be found in *Cheng et al.* (2002). To simplify the presentation, we only consider the effect of potential temperature fluctuation θ' on buoyancy, though an extension to include salinity can be made easily. After applying the boundary layer approximations and directing the x-coordinate to the direction of

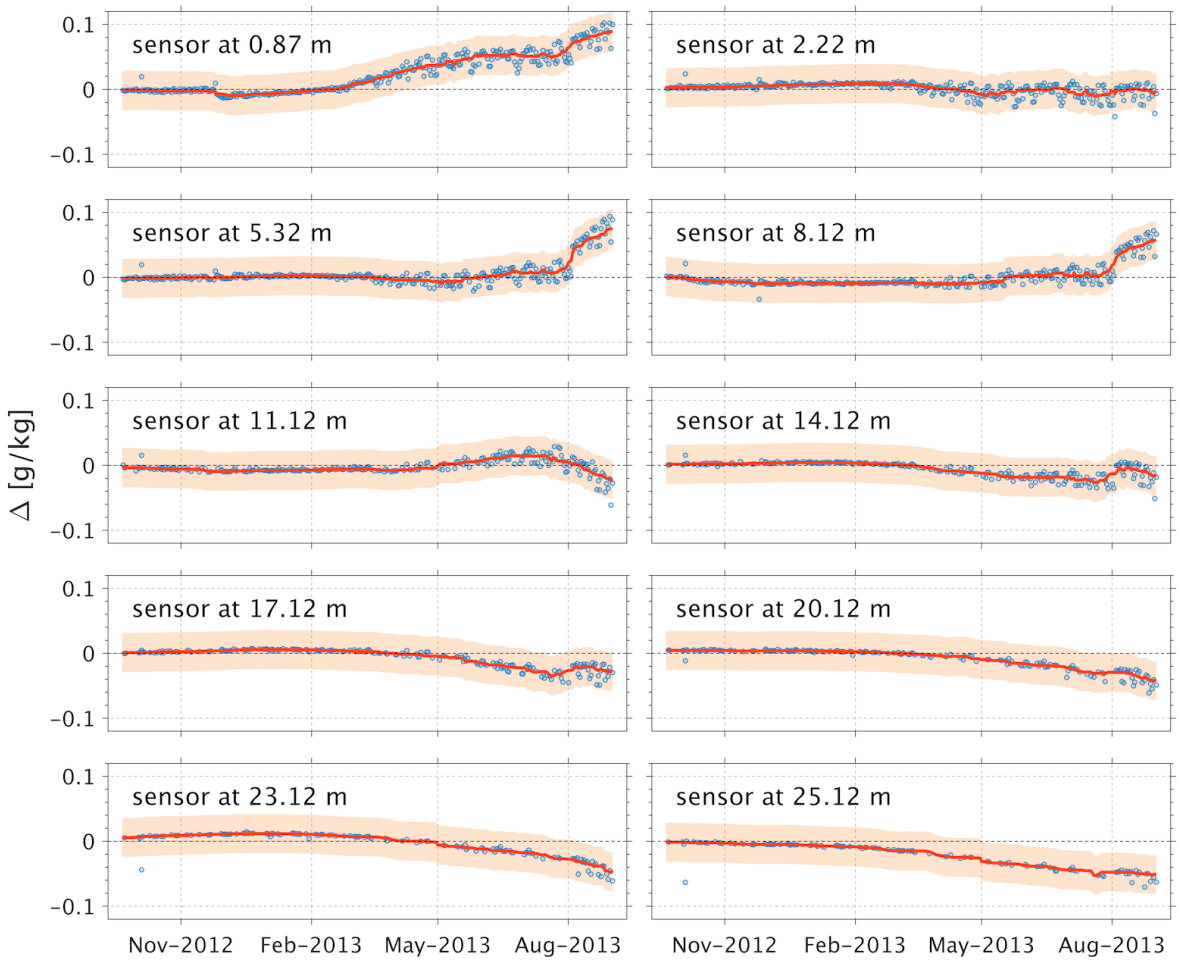

Figure 2.11: Time series of salinity corrections (Δ = adjusted value $-$ raw value) for the SPURS-I mooring sensors. Blue dots are sensor offsets estimated from the nightly corrections. Thick orange lines are drift curves derived from linear interpolations of the filtered nightly corrections. The light orange area shows $\pm$ 0.03 g kg^{-1} deviations from drift curves.

surface wind stress, the model equations can be simplified to

$$\frac{q^3}{B_1\ell} = -\overline{w'u'}\frac{\partial \overline{u}}{\partial z} + \alpha g\overline{w'\theta'}, \tag{2.33a}$$

$$\overline{u'u'} = \frac{q^2}{3}(1 - \frac{6A_1}{B_1}) - \frac{6A_1\ell}{q}\overline{w'u'}\frac{\partial \overline{u}}{\partial z}, \tag{2.33b}$$

$$\overline{v'v'} = \frac{q^2}{3}(1 - \frac{6A_1}{B_1}), \tag{2.33c}$$

$$\overline{w'w'} = \frac{q^2}{3}(1 - \frac{6A_1}{B_1}) + \frac{6A_1\ell}{q}\alpha g\overline{w'\theta'}, \tag{2.33d}$$

$$\overline{w'u'} = -\frac{3A_1\ell}{q}\Big[(\overline{w'w'} - C_1q^2)\frac{\partial \overline{u}}{\partial z} - \alpha g\overline{u'\theta'}\Big], \tag{2.33e}$$

$$\overline{u'\theta'} = -\frac{3A_2\ell}{q}\Big[\overline{w'u'}\frac{\partial \overline{\theta}}{\partial z} + (1 - C_2)\overline{w'\theta'}\frac{\partial \overline{u}}{\partial z}\Big], \tag{2.33f}$$

$$\overline{w'\theta'} = -\frac{3A_2\ell}{q}\Big[\overline{w'w'}\frac{\partial \overline{\theta}}{\partial z} - (1 - C_3)\alpha g\overline{\theta'\theta'}\Big], \tag{2.33g}$$

$$\overline{\theta'\theta'} = -\frac{B_2\ell}{q}\overline{w'\theta'}\frac{\partial \overline{\theta}}{\partial z}. \tag{2.33h}$$

In the above equations, $q^2 = \overline{u'u'} + \overline{v'v'} + \overline{w'w'}$ is twice the TKE; u', v' and w' are the three-dimensional velocity fluctuations in Cartesian coordinate system x, y, z; ℓ is the turbulent (master) length scale. Constants A_1 and C_1 were introduced in the approximations for the slow return-to-isotropy, and the rapid distortion components of the pressure-strain rate covariances, respectively (*Rotta*, 1951; *Crow*, 1968); constants A_2, C_2 and C_3 come from the approximations for the pressure-scalar gradient covariances (*Mellor*, 1973; *Andrén and Moeng*, 1993; *Moeng and Wyngaard*, 1986; *Launder*, 1975); constants B_1 and B_2 originate from the small-scale local isotropy hypothesis for the dissipation of TKE and temperature variance, respectively (*Kolmogorov*, 1941). Standard values for these constants are listed below:

$$(A_1,\ A_2) = (0.92,\ 0.74); \tag{2.34a}$$

$$(B_1,\ B_2) = (16.6,\ 10.1); \tag{2.34b}$$

$$(C_1,\ C_2,\ C_3) = (0.08,\ 0.7,\ 0.2). \tag{2.34c}$$

In the surface layer, vertical fluxes of momentum and heat may be approximated by their surface values, and other variables can be scaled accordingly:

$$(u_*^2,\ 0,\ Q) = -(\overline{w'u'},\ \overline{w'v'},\ \overline{w'\theta'}), \tag{2.35a}$$

$$\ell^* = \ell/\kappa|z|, \tag{2.35b}$$

$$(\overline{u^*u^*},\ \overline{v^*v^*},\ \overline{w^*w^*}) = (\overline{u'u'},\ \overline{v'v'},\ \overline{w'w'})/u_*^2, \tag{2.35c}$$

$$(q^{*2},\ \overline{u^*v^*}) = (q^2,\ \overline{u'v'})/u_*^2, \tag{2.35d}$$

$$\overline{\theta^*\theta^*} = \frac{\overline{\theta'\theta'}}{Q^2/u_*^2}, \tag{2.35e}$$

$$(\overline{u^*\theta^*},\ \overline{v^*\theta^*}) = (\overline{u'\theta'},\ \overline{v'\theta'})/Q, \tag{2.35f}$$

$$\phi_m = \frac{\partial\overline{u}}{\partial z}\Big/\frac{u_*}{\kappa|z|}, \tag{2.35g}$$

$$\phi_h = \frac{\partial\overline{\theta}}{\partial z}\Big/\frac{Q/u_*}{\kappa|z|}, \tag{2.35h}$$

$$\zeta = \frac{|z|}{L} = \frac{\kappa|z|\alpha g Q}{u_*^3}. \tag{2.35i}$$

With the scaling of variables defined above, the model equations can be non-dimensionalized and reduced to

$$q^{*3} = B_1\ell^*(\phi_m - \zeta), \tag{2.36a}$$

$$\begin{aligned}\frac{1}{3A_1q^*\ell^*} =& \phi_m\left[r - C_1 - \frac{\big(6A_1 + 3A_2(1-C_2)\big)\zeta\ell^*}{q^{*3}}\right] \\ & -\phi_h\left[3A_2\zeta\ell^*/q^{*3}\right],\end{aligned} \tag{2.36b}$$

$$\frac{1}{3A_2q^*\ell^*} = \phi_h\left[r - \big(6A_1 + B_2(1-C_3)\big)\zeta\ell^*/q^{*3}\right], \tag{2.36c}$$

where $r = 1/3 - 2A_1/B_1$. The length scale ($q^2\ell$) equation is not included here, because for the classical super-equilibrium SMC, the length scale equation can be simplified to give $\ell^* \approx 1$ (*Kantha and Clayson*, 2004). Therefore, by assuming $\ell = \kappa|z|$ (i.e., $\ell^* = 1$), one can numerically solve Eqs. (2.36) to express ϕ_m and ϕ_h as a function of ζ. These predictions of dimensionless gradients are referred to as the "model intrinsic similarity relations" in

this paper. Previous studies have shown that the prediction of ϕ_h in this classical SMC matches the Kansas experimental data pretty well, especially under unstable conditions (see Figure 2 of *Kantha and Clayson*, 1994).

Chapter 3

SCALING NEAR-SURFACE OBSERVATIONS OF TURBULENT VERTICAL VELOCITY IN THE OCEAN, PART I: SURFACE LAYER

Abstract

Conventional scaling of near-surface vertical velocity variance $\overline{w^2}$ in the ocean relies on the Monin-Obukhov similarity theory (MOST). Here we test this standard scaling approach using measurements of vertical velocity made by neutrally buoyant Lagrangian floats. These data cover a broad range of surface wind, wave, and buoyancy forcing conditions with wind speeds ranging from 7 to 47 m s^{-1}, significant wave heights from 0 to 10 m, upward surface buoyancy fluxes from -4.2$\times 10^{-7}$ to 1.6$\times 10^{-7}$ W/kg, and boundary layer depths from 12 to 1204 m. While MOST can predict the trend of $\overline{w^2}$ variation with the wind and buoyancy forcing, it fails to account for the large variability under the same wind stress and surface buoyancy flux. Observations are typically higher than the predictions of MOST by a factor varying from 1 to 3. This elevation of variance is proportional to the strength of surface wave forcing, measured by the relative magnitude of wave-induced Stokes drift to the stress-induced friction velocity. An improved scaling, incorporating the local production due to Stokes drift shear with a correction for surface proximity, reduces the mean absolute percentage error of $\overline{w^2}$ to 13%, a factor of 3 smaller than that of MOST. Incorporation of this scaling into boundary layer parameterizations based on MOST may make them more realistic.

3.1 Introduction

The ocean and atmosphere communicate through the boundary layers on both sides of the air-sea interface. The dynamical evolution of these two layers directly controls the

exchange of tracers that are important to the prediction of weather and climate. Our ability to make such predictions relies on our understanding of the turbulent motions within the boundary layer that advect, and diffuse or mix tracers throughout. Of all the three directions of the boundary layer turbulence, the vertical motion has the most direct impact on vertical fluxes that govern the boundary layer dynamics through flux divergence, while the mean properties and turbulence of the boundary layer are assumed homogeneous in horizontal directions. In this one-dimensional approximation, the vertical velocity is an important measure of the vertical mixing strength and is widely used to parameterize the vertical eddy diffusivity (*Large et al.*, 1994; *Reichl and Hallberg*, 2018; *Allouche et al.*, 2022). Measurements of the turbulent vertical velocity are usually presented as the variance $\overline{w^2}$ to represent its kinetic energy level. Observations of $\overline{w^2}$ are valuable in testing and refining the various scaling relationships that underpin the vertical eddy diffusivity in boundary layer models.

The ocean surface boundary layer (OSBL) is relatively less understood compared to the atmospheric boundary layer (ABL). Many existing models of the OSBL (*Mellor and Yamada*, 1982; *Large et al.*, 1994; *Kantha and Clayson*, 1994; *Reichl and Hallberg*, 2018) are constructed using empirical scaling relationships in the ABL. Here we focus on the scaling of vertical velocity in the near-surface, upper 20% of the boundary layer, referred to as the surface layer. In the atmospheric surface layer (ASL), observations and large eddy simulations (LES) have shown that the $\overline{w^2}$ profiles closely follow scaling based on the Monin-Obukhov similarity theory (MOST) under destabilizing conditions (*Panofsky et al.*, 1977; *Wilson*, 2008; *Maronga and Reuder*, 2017); and are also consistent with the z-less scaling, an asymptote of MOST in the stratified regime, up to moderately stabilizing conditions (*Wyngaard and Coté*, 1972; *Sorbjan*, 1986; *Grachev et al.*, 2013). The formulation of the surface layer scaling is introduced later in Section 3.3.

Neither of these two surface layer scaling relationships for $\overline{w^2}$ has been formally tested using ocean measurements, but contemporary studies have demonstrated that the corresponding ABL scaling for the neutral and boundary layer-averaged, bulk vertical

velocity variance $\langle\overline{w^2}\rangle$ does not generally hold for the OSBL. Using neutrally buoyant Lagrangian float data and ignoring weak buoyancy forcing, *D'Asaro* (2001) reported 75% $\sim$ 100% higher vertical velocity variance in the ocean mixed layer than in laboratory solid-wall boundary layers. This enhancement was in agreement with LES-modeled elevated levels of $\langle\overline{w^2}\rangle$ in "Langmuir turbulence" (*Skyllingstad and Denbo*, 1995; *McWilliams et al.*, 1997), due to the generation of Langmuir circulation within the OSBL by the interaction between vorticity and the Stokes drift of surface gravity waves (*Craik and Leibovich*, 1976), or equivalently, by the Stokes shear force (*Suzuki and Fox-Kemper*, 2016). This theory was confirmed in subsequent quantitative comparisons between boundary layer averaged Lagrangian float measurements and LES-derived scaling relationships for $\langle\overline{w^2}\rangle$ in Langmuir turbulence (*Harcourt and D'Asaro*, 2008), and through comparisons of $\langle\overline{w^2}\rangle$ measurements between fully developed open ocean seas and fetch-limited lake environments with reduced Stokes drift (*D'Asaro et al.*, 2014a). However, these studies did not mention how the enhancement due to Langmuir turbulence would vary in non-neutral conditions and with depth. Given that the buoyancy forcing plays a primary role in regulating the boundary layer evolution and that model results are sensitive to the vertical structure of mixing (*Reichl et al.*, 2016), it is rewarding to further explore the depth-dependent scaling of vertical velocity variance under a wide range of buoyancy forcing conditions. Conventionally, the depth-dependency and the buoyancy effect are discussed in the context of surface layer scaling and boundary layer scaling. In this Chapter, we concentrate on the scaling of surface layer $\overline{w^2}$. The scaling of $\overline{w^2}$ in the entire boundary layer is discussed in Chapter 4.

3.2 Data and method

Five sets of observational data with auxiliary reanalysis products and model simulations are used in this study to test the surface layer scaling of the vertical velocity variance in the ocean. Three of them were collected at the ocean climate station Papa (50°N, 145°W) during the winter and spring of 2011, the late summer of 2012; and at Lake Washington

near Seattle during the fall of 2012. These three are the same data sets used by (*D'Asaro et al.*, 2014a). Additional data sets include the Labrador Sea Deep Convection Experiment (*Marshall et al.*, 1998) data collected in the deeply ventilated southwest half of the basin during two consecutive winters (1997-1998), and the data collected under typhoon Fanapi (September 2010) in the Impact of Typhoons on the Ocean in the Pacific (ITOP) field campaign *D'Asaro et al.* (2014b). The second year of the Labrador Sea data is omitted due to the substantial influence of lateral heat flux divergence inferred from estimates of the one-dimensional heat budget (see Appendix 3.A). This lateral effect is also evidenced by the observed intensification of submesoscale eddy activities in 1998 (*Steffen and D'Asaro*, 2004). The selected data sets cover a wide range of wind forcing, buoyancy forcing, and wave forcing conditions (Figure 3.1), but because float measurement is more accurate when the turbulence is stronger, they unavoidably only represent the strongly-forced half of the global upper ocean.

3.2.1 Vertical velocity

Lagrangian float data is the major component of each observation set. A few variants of the float are used in different experiments, a notable example is the Deep Lagrangian Float (DLF) in the deep convection experiment (*Steffen and D'Asaro*, 2002), but the operation principle is nearly identical and hence has no impact on the computed velocity. The float is designed to follow the three-dimensional motion of surrounding water parcels within the boundary layer, by maintaining nearly neutral buoyancy and by having a high drag (*D'Asaro et al.*, 1996; *D'Asaro*, 2003a). These floats are about 1 m in size, and record depth using one or several onboard pressure sensors sampling at 1 Hz (DLF samples pressure every 5 minutes). The fluid vertical velocity is measured from the rate of change of the pressure by assuming negligible relative motion between the float and the ambient water. The sampling frequency is adequate to resolve the inertial sub-range of the Lagrangian velocity spectrum (*Lien et al.*, 1998). This approach filters out the much larger surface

wave orbital velocity as waves have a negligible effect on the pressure along a Lagrangian trajectory (*D'Asaro*, 2015). The assumption of no relative motion is not always valid and depends on the quality of the float buoyancy calibration, so the float can be imperfectly Lagrangian at times. Circumstances with anomalous float buoyancy are identified and removed (see Appendix 3.B), and the buoyancy-induced errors for $w_{rms} = \sqrt{\overline{w^2}}$ in other cases are estimated to be less than 5% (*D'Asaro et al.*, 2014a). The finite size of the float also causes an underestimate of the true velocity as the float only tracks motions of scale larger than itself and averages the effect of smaller eddies. This bias is corrected by fitting the measured Lagrangian vertical acceleration spectrum to a universal spectral model (*Lien et al.*, 1998) and adding the theoretical value of missed variance to the computed vertical velocity variance (see Appendix 3.C). More details about the velocity calculation and processing are included in the supporting information Appendix 3.B.

3.2.2 *Depth-dependent velocity variance*

Previous estimates (*D'Asaro et al.*, 2014a) of bulk variance $\langle\overline{w^2}\rangle$ are obtained by averaging w^2 along the drifting trajectory over intervals longer than the overturning time of the boundary layer h/w_{rms}, where h is the boundary layer depth, so each value is statistically independent. This method also assumes the float uniformly samples the boundary layer across depths, so the mean in each interval is essentially a layer average. Here, to obtain variance profiles, a different method is used. For every quality-controlled Lagrangian drift, w from the center difference of p over two sampling intervals are low-passed, and w^2 are averaged in each 1 m (5 m for DLF) and 1 hour bin that the float passes through. Weighted averages are then computed from the binned w^2, each with a weight (or degree of freedom) estimated as $n\Delta t/T$, where n is the number of data in each bin, Δt is the sampling period, and $T = 2\overline{h/w_{rms}}$ is the time scale for a round trip overturn averaged over the entire experiment. The boundary layer depth at station Papa and Lake Washington are computed from a bulk Richardson number criteria using one-dimensional

KPP (*Griffies et al.*, 2015) simulations forced by realistic forcing; for other cases, h is estimated from the float drifting trajectory (see Appendix 3.D). The results of the vertical velocity variance scaling are not sensitive to marginal errors in the estimates of h.

3.2.3 *Air-sea fluxes*

As in *D'Asaro et al.* (2014a), surface fluxes of momentum, heat, and freshwater at station Papa and Lake Washington are estimated from buoy measurements of surface meteorological conditions, using the Coupled Ocean-Atmosphere Response Experiment (COARE) 3.0 formulae (*Fairall et al.*, 2003). Errors associated with the bulk estimates are discussed in *D'Asaro et al.* (2014a).

Although there are accompanying shipboard meteorological measurements in the deep convection experiment, the floats are not always close to the ship track (Figure 3.5). Given the considerable spatial variation of fluxes at scales comparable to the distance between floats and the ship, we use the hourly ERA5 surface reanalysis product (*Hersbach et al.*, 2020). A correction of the ERA5 turbulent fluxes is applied to achieve a better match with the shipboard observations (see Appendix 3.E).

Air-sea fluxes under tropical cyclones are highly variable (*Sroka and Emanuel*, 2021) and the current parameterization in the bulk formulae is less reliable in the high wind regime. For that, we adopt the *Hsu et al.* (2019) drag coefficient results for typhoon Fanapi and their reconstructed wind fields to compute the surface stress at Lagrangian float positions. Their drag coefficient values are estimated from the storm-forced response of the horizontal velocity by assuming a linear momentum budget in the upper 100 m (*Sanford et al.*, 2011; *Hsu et al.*, 2017). The horizontal velocity is measured by the Electromagnetic Autonomous Profiling Explorer (EM-APEX) floats, which are air-deployed along with the Lagrangian floats used here. A slightly different analysis of the same EM-APEX float data yields similar results (*Zhou et al.*, 2022). In this mechanical forcing-dominated boundary layer, the impact of surface buoyancy flux on $\overline{w^2}$ is relatively small. Nevertheless, we use the

heat and freshwater fluxes of the ERA5 reanalysis and adjust the sensible and latent heat flux to match the storm-averaged values from observations (*Lin et al.*, 2013). Details of the flux calculation for typhoon Fanapi are included in the supporting information Appendix 3.F.

3.2.4 Surface waves

Nearby Waverider buoys at station Papa and Lake Washington provide half-hourly measurements of directional surface wave spectrum to compute the Stokes drift profile and its vertical shear. No direct measurements of surface waves are available for the Labrador Sea and typhoon Fanapi case. We instead use the ERA5 reanalysis wave spectra (*Hersbach et al.*, 2020) and a WaveWatch III model output forced by typhoon Fanapi wind field (*Zhou et al.*, 2022). The Stokes drift and its shear are projected to the direction of surface wind stress, which is the same as the direction of the wind vector except in typhoon Fanapi (*Hsu et al.*, 2019). For the purpose of specifying surface wave forcing, only the downwind component is used. Details of the calculation are presented in the supporting information Appendix 3.G.

3.3 Scaling framework

3.3.1 The conventional approach

The surface layer Monin-Obukhov similarity theory (MOST) considers flow properties in a horizontally homogeneous, quasi-steady, wall-bounded turbulent surface layer, in which the turbulent eddies grow larger as they move away from the surface. This turbulent flow is driven by a combination of the stress (u_*^2) and buoyancy flux (B_0) imposed at the surface and can be well characterized by the local ratio of the neutral Eulerian shear production (ESP_n, the shear production it would have if there were no buoyancy effect) and the buoyancy flux (BF) in the turbulent kinetic energy (TKE) budget. As a result, most flow properties in the surface layer, such as the vertical gradient of mean velocity

and scalar, and the turbulent velocity and scalar variances, when properly normalized according to Buckingham's Pi theorem, are universal functions of the local production ratio $(-\zeta)$, e.g.,

$$\phi_{ww} = \frac{\overline{w^2}}{u_*^2} = f(\zeta), \qquad -\zeta = \frac{-B_0 G(z)}{u_*^3 G(z)/\kappa|z|} = \frac{|z|}{-L}, \tag{3.1}$$

where the turbulent stress and the buoyancy flux are assumed to have the same vertical structure $G(z)$, which is usually a linear decay from the surface value to zero at the boundary layer depth, or even uniform with depth using a constant-flux layer assumption, $\kappa = 0.4$ is the von Kármán constant, $L = -u_*^3/\kappa B_0$ is the Obukhov length that defines the depth where the neutral Eulerian shear production equals the buoyancy flux. This local production ratio is also known as the Monin-Obukhov stability parameter (ζ) as it separates the destabilizing and stabilization conditions. The exact form of the universal function $f(\zeta)$ is not predicted by MOST and has to be determined from measurements.

However, MOST does predict the asymptotic behavior of these functions. In the very unstable regime ($\zeta \ll -1$), $\phi_{ww} \sim (-\zeta)^{2/3}$ (local free convection scaling). In the very stable regime ($\zeta \gg 1$), vertical motion is suppressed by stratification, and turbulence becomes decoupled from the surface, thus $|z|$ is no longer relevant in the scaling, and ϕ_{ww} stays constant (z-less scaling). Analysis of *Sorbjan* (1986) suggests a maximum value for ϕ_{ww} of about 2.5 in stabilized conditions. To compare with the ocean $\overline{w^2}$ measurements, we adopt the following universal function for vertical velocity variance

$$f_{ASL}(\zeta) = \begin{cases} (1 - 4.5\zeta)^{2/3}, & \zeta < 0 \\ 1, & \zeta > 0 \end{cases} \tag{3.2}$$

The empirical formula for $\zeta < 0$ is from *Wilson* (2008). It agrees with the LES results of *Maronga and Reuder* (2017) and approaches the local free convection scaling as $\zeta \to -\infty$. The function for $\zeta > 0$ is generally considered to be a constant (*Grachev et al.*, 2015) and 1 is used here to ensure continuity across the neutral condition. Other functions have also been proposed to fit various measurements of $\overline{w^2}$ in the ASL. These are represented by

the gray shading in Figure 3.2, with the upper bound from *Panofsky et al.* (1977) and the lower bound from an alternative formula proposed by *Wilson* (2008).

3.3.2 *An extension for Langmuir turbulence*

This conventional scaling framework is not sufficient for Langmuir turbulence. The turbulent flow associated with Langmuir circulation is more energetic, especially in the vertical, due to additional kinetic energy input from the work of Stokes shear force (*Suzuki and Fox-Kemper*, 2016) or vortex force (*Craik and Leibovich*, 1976). Therefore the flow property in the Langmuir surface layer is likely regulated by all three source terms of the TKE budget.

Previous studies (*Belcher et al.*, 2012) have found that the bulk turbulence quantity of the OSBL can be effectively parameterized in a regime diagram consisting of two axes, one representing the bulk ratio of the buoyancy flux to the Stokes shear production (SSP), the other representing the bulk ratio of the neutral Eulerian shear production to the Stokes shear production. Following the same strategy, an intuitive extension to the conventional surface layer scaling framework is to consider two local TKE production ratios, one between the buoyancy flux and the Stokes shear production, and another between the neutral Eulerian shear production and the Stokes shear production. Here the conventional form of the neutral Eulerian shear production $[u_*^3 G(z)/\kappa|z|]$ is retained for simplicity and consistency, although its reduction relative to the no-wave case is often seen in both observations and numerical simulations of Langmuir turbulence (*Feddersen et al.*, 2007; *Large et al.*, 2019). Similar to that of *Belcher et al.* (2012), a regime diagram for the surface layer scaling (Figure 3.1) can be constructed, with the horizontal and vertical axis defined by ESP_n/SSP and BF/SSP, respectively. This regime diagram uses the local production ratio, rather than a scaling measure of the bulk ratio of productions. Lines of constant slopes in this diagram represent the Monin-Obukhov stability parameter ζ. The

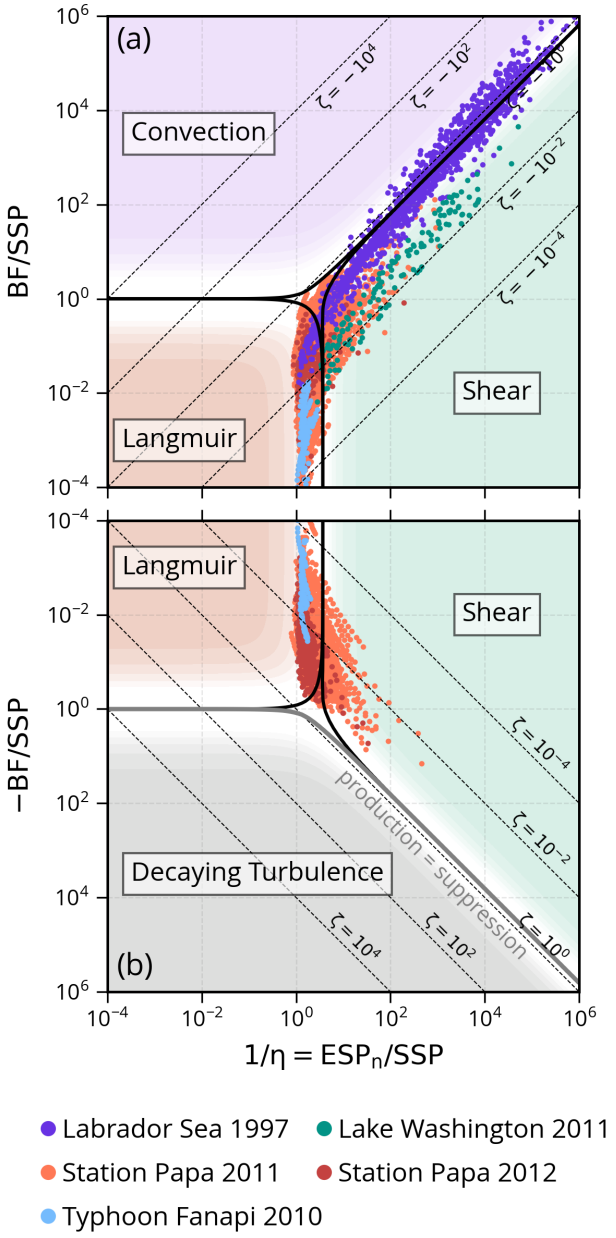

Figure 3.1: Turbulence regime diagrams for surface layer scaling under conditions of (a) destabilizing and (b) stabilizing surface buoyancy flux. The horizontal (vertical) axis is the local ratio of neutral Eulerian shear production ESP_n (buoyancy flux BF) to Stokes shear production SSP. Background colors show the fraction (50% $\sim$ 100%) of SSP (white to orange), $|BF|$ (white to purple, white to gray), and ESP_n (white to green) in the total local production (Equation 3.3). Thick black lines mark where each term contributes 50% to the total production. The gray line marks where the local production equals the suppression due to stabilizing buoyancy flux. Slanted dash lines show contours of the Monin-Obukhov stability parameter $\zeta = -BF/ESP_n$. The parameter space covered by the observational data is shown by the colored dots, assuming $G(z) = 1 + z/h$.

total local production of TKE ($\mathcal{P}$) is

$$\mathcal{P} = SSP \cdot \left(1 + \frac{BF}{SSP} + \phi_m \chi_m \frac{ESP_n}{SSP}\right), \tag{3.3}$$

where ϕ_m and χ_m are non-dimensional functions representing the effect of buoyancy flux and Langmuir turbulence on the Eulerian shear. With the empirical function ϕ_m from *Large et al.* (1994), and χ_m from *Large et al.* (2019), the fraction of $\mathcal{P}$ contributed by each production mechanism is shown by the background colors in Figure 3.1. Corners encompassed by the 50% contribution line define regions where the Langmuir, convective, and shear turbulence dominates the TKE production.

By analogy to MOST, non-dimensional flow properties in this system should depend on two local production ratios. For consistency, in addition to the conventional parameter ζ, we introduce a Stokes production ratio,

$$\eta = SSP/ESP_n = \frac{\partial u^s}{\partial z} \Big/ \frac{u_*}{\kappa |z|}, \tag{3.4}$$

where $\partial u^s / \partial z$ is the vertical shear of Stokes drift u^s. Similar to the local free convection limit, when the Stokes shear production dominates the TKE production, we expect an asymptotic scaling $\phi_{ww} \sim \eta^{2/3}$. The skill of this new scaling parameter η is tested in Section 3.4.2.

3.4 *Results*

3.4.1 *The dependence on wind and buoyancy forcing*

Measurements of vertical velocity variance in the surface layer are normalized by u_*^2 and are shown as bin averages in the ζ coordinate (Figure 3.2). Similar to the results of *D'Asaro et al.* (2014a), the lake values are lower than open ocean values at station Papa, regardless of any processing details (Figure 3.9). The conventional Monin-Obukhov scaling is able to predict the tendency of ϕ_{ww} variation with stability conditions. The overall mean of all data rises as convection gets stronger in destabilizing conditions, and

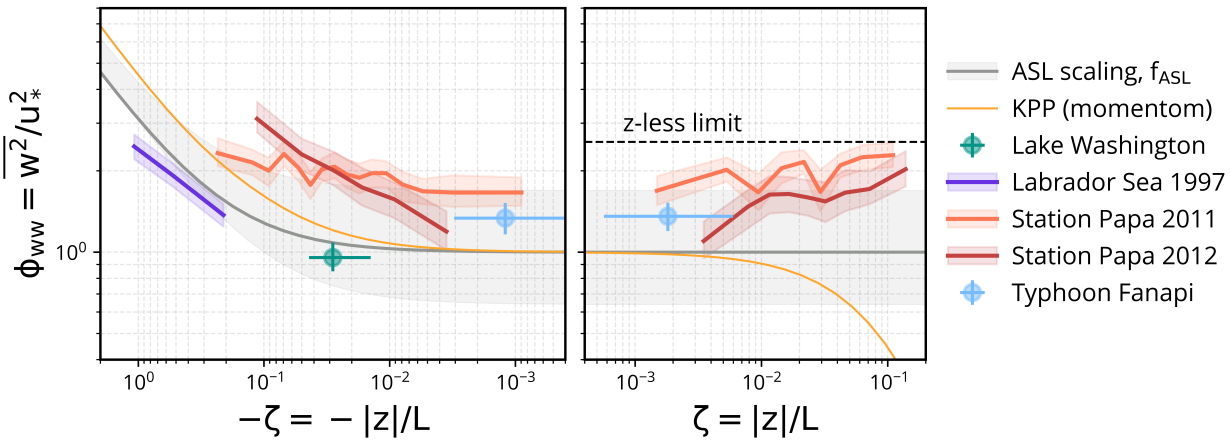

Figure 3.2: Conventional surface layer scaling of the vertical velocity variance $\langle w^2 \rangle$. Lagrangian float measurements are averaged in bins of approximately the same degrees of freedom ($\sim$5), and placed at the median values of ζ. Color shadings of observations and vertical error bars show the 95% bootstrap confidence intervals of the mean and horizontal error bars show the lower and upper quartiles of ζ. A commonly used empirical function $f_{ASL}(\zeta)$ (*Wilson*, 2008) is given as the gray line and the gray shading shows the variation of a few other variants (see main text). The black dash line is the z-less limit in very stable conditions (*Sorbjan*, 1986). The orange curve is the equivalence of the turbulent velocity scales used in the KPP model (*Large et al.*, 1994)

flattens, approaching the z-less limit in stabilizing conditions. This suggests that the buoyancy effect on vertical turbulence intensity remains about the same in the oceanic surface layer.

However, there is a large amount of unexplained variability among these data sets, which we think is due to the diverse contribution of wave forcing at different environments (Section 3.4.2). The comparison with a commonly used universal function for ϕ_{ww} (Equation 3.2) and a few variants of it shows different levels of agreement. The lake data are consistent with the ASL results, but about 30% lower if we don't correct for the float size effect (Figure 3.9). The Labrador Sea data match the ASL results better if we use the corrected ERA5 surface fluxes, but the agreement is still solid if no correction is applied (Figure 3.9). Data from station Papa and typhoon Fanapi are higher than the ASL results

in both destabilizing and stabilizing conditions, by a factor varying between 1 and 3. Even though the variance increase is less prominent if we don't account for the float size effect, the higher values for $\zeta < -0.2$ remains significant (Figure 3.9). Overall, predictions based on the Monin-Obukhov scaling have a mean absolute percentage error of about 39%. Since there is no doubt that the finite float size would cause a low bias in measured variance, we conclude that the conventional scaling based on the wind and buoyancy forcing is not enough to capture the major variability of $\overline{w^2}$ in the oceanic surface layer and hence parameterizations built on this conventional scaling would underestimate the mixing near the surface.

3.4.2 *The dependence on wave forcing*

To further investigate the deviations of ϕ_{ww} from the conventional scaling, we normalize the dimensionless $\overline{w^2}$ in Figure 3.2 by the empirical formula f_{ASL} from ASL to remove the effects of wind and buoyancy forcing. If one suspects that the Langmuir turbulence affects the surface layer scaling, it is perhaps most straightforward to explore the dependence of these ϕ_{ww} deviations on Langmuir numbers, which have been proven quite useful in the bulk $\langle\overline{w^2}\rangle$ scaling (*Harcourt and D'Asaro*, 2008; *Van Roekel et al.*, 2012; *Reichl et al.*, 2016). Two variants of the Langmuir number are considered here. The turbulent Langmuir number La_t uses the ratio of the friction velocity u_* to the surface Stokes drift velocity u_0^s as a proxy for the strength of Langmuir turbulence, while the surface layer Langmuir number La_{SL} replaces u_0^s with the surface layer averaged Stokes drift referenced to the Stokes drift near the boundary layer depth $[u^s(-0.765h)]$ to emphasize the average effect of a spectrum of waves with different decay depth. Figure 3.3a and 3.3b show the ϕ_{ww} deviations as a function of the turbulent Langmuir number and the surface layer Langmuir number, respectively. Although it is very clear that these deviations increase as the wave forcing becomes stronger relative to the wind forcing, neither form of the Langmuir number can adequately characterize the variation of enhanced ϕ_{ww}. The turbulent Langmuir number

scaling has a small scatter overall, but it fails for the Labrador Sea data. This is because the wintertime boundary layer at the deep convection site is extremely deep (820 m on average), even though the surface waves can be quite big during storms, the Stokes drift decays rapidly in the upper 10 m and contributes less to the turbulence in the entire surface layer of thickness about 164 m. This limitation of La_t can be remedied by using the surface layer Langmuir number that averages the near-surface Stokes drift out to a small number for deep surface layers, but the La_{SL} scaling only poorly collapses the data from different environments, with a root mean square error (RMSE) about 0.09. This is actually not surprising, since the surface layer Langmuir number effectively uses a turbulent length scale-weighted averaged Stokes shear over the boundary layer (*Kukulka and Harcourt*, 2017). Given its physical basis on the boundary-layer averaged balance between the Stokes shear production and the TKE dissipation, La_{SL} works very well in scaling the mean vertical velocity variance of the entire boundary layer. But it would not necessarily perform well here as the surface layer scaling considers vertical variation and is strongly affected local dynamics.

One alternative to the Langmuir numbers that can be used to describe the wave forcing but also contains local information is the Stokes shear production ratio η introduced in Section 3.3.2. We compute this parameter using the Stokes shear profile and assume a linear decay of the turbulent stress and buoyancy flux profile. Figure 3.3c shows the ϕ_{ww} deviations as a function of the SSP ratio. It has hardly any merit over the Langmuir number scaling. The variation of ϕ_{ww} deviation is not monotonic as η increases, a peak occurs around $\eta = 0.6$.

This non-monotonic behavior is maybe physically related to the non-local effects of Langmuir turbulence. First, the turbulent transport of vertical TKE is significant in the presence of Langmuir turbulence (*Polton and Belcher*, 2007; *Grant and Belcher*, 2009; *Kukulka et al.*, 2010, 2012). Near the surface, a large portion of the locally produced vertical TKE is carried by the large-scale downwelling plumes of Langmuir turbulence to the lower part of the OSBL, leading to smaller $\overline{w^2}$ in the surface layer. Another possibility is that, near the

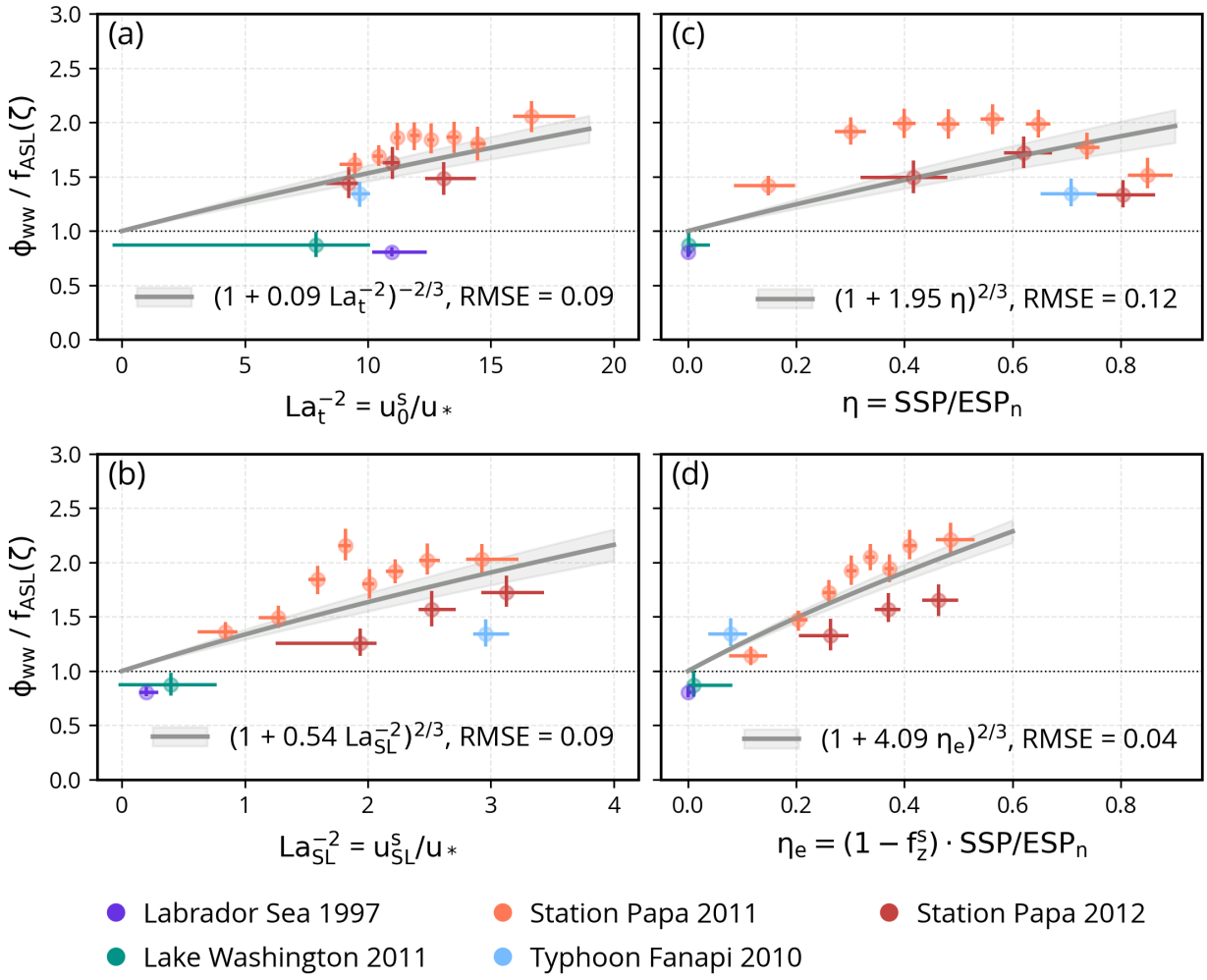

Figure 3.3: Observed deviations of dimensionless vertical velocity variance ϕ_{ww} from the ASL scaling $f_{ASL}(\zeta)$ as a function of (a) turbulent Langmuir number La_t, (b) the surface layer Langmuir number La_{SL}, (c) the SSP ratio, and (d) the effective SSP ratio. Measured dimensionless variances ϕ_{ww} are normalized by the ASL scaling before averaging in bins of about 15 degrees of freedom. Mean values with 95% bootstrap confidence intervals are placed at the median values of the coordinate, whose lower and upper quartiles are shown by the horizontal error bars. The shading of the least-square fits represents the uncertainty of the fitting parameter.

surface, pressure–strain correlations can "block" the near-surface Stokes production of $\overline{w^2}$ along the downwind jet and redirect it anisotropically into the crosswind component as fluid is pulled into the counter-rotating vortices of Langmuir cells. Such a mechanism has been recognized (*Pearson et al.*, 2019) and parameterized in the turbulence closure model of *Harcourt* (2015). To incorporate the non-local effects on the surface layer scaling of $\overline{w^2}$, we assume the non-local terms, including the turbulent transport and the pressure–strain correlations, decay with depth and are proportional to the local Stokes shear production. These are represented in the effective Stokes shear production (SSP) ratio $\eta_e = (1 - f_z^s) \cdot \eta$, where $f_z^s = 1 + \tanh(c_l^s \cdot z/l^s)$ is a surface proximity function (*Harcourt*, 2015) that models the fraction of the redirected or transported SSP, the decay length scale l^s is the mean turbulent length scale weighted by positive SSP in the boundary layer, and c_l^s is a constant. Note that *Harcourt* (2015) sets $c_l^s = 1/4$, but we find a smaller value $c_l^s = 1/24$ is needed to rearrange the data in Figure 3.3c to a monotonic trend. Figure 3.3d shows the ϕ_{ww} deviations as a function of the effective SSP ratio. With a simple power law fit, the scaling based on the effective SSP ratio reduces the mean absolute percentage error down to 13% with an RMSE of about 0.04. It appears that η_e can scale the enhanced ϕ_{ww} much better than η, and perhaps more skillful than either form of the Langmuir number tested here.

3.5 *Summary*

Five sets of Lagrangian float measurements of vertical velocity are used to investigate the depth-dependent scaling in the oceanic surface layer. These data show that they scale with the wind and buoyancy forcing, similarly as they do in the atmospheric or wall-bounded surface layer. However, a large degree of variability above this traditional prediction appears attributable to the presence of surface waves, as for the bulk average of $\overline{w^2}$ over the entire boundary layer. The measured surface layer $\overline{w^2}$ deviates from the conventional scaling by a factor varying between 1 and 3 and proportional to the magnitude of surface wave forcing. The enhancement of $\overline{w^2}$ in the surface layer can not be sufficiently scaled by either the turbulent Langmuir number or the surface layer Langmuir number. Local

analysis of the TKE budget for Langmuir turbulence suggests that the ratio of Stokes shear production to the neutral Eulerian shear production should be the additional scaling parameter to consider. However, a scaling approach based on the local production ratios does not work well unless the suppression of Stoke shear production with proximity to the surface is incorporated.

APPENDICES

Appendix 3.A Lateral restratification effects in the Labrador Sea 1998 data

The Labrador Sea vertical velocity data collected in 1998 are excluded from the one-dimensional scaling analysis, because the boundary layer turbulence is strongly suppressed by the restratification due to baroclinic eddies formed as a result of sharp horizontal density gradients. The contribution of lateral heat flux divergence is estimated by computing the 1-D heat budget using float measurements of temperature (*D'Asaro*, 2003b, 2004). In 1997, the lateral heat flux divergence is less than 10% of those in the vertical, while in 1998, the lateral heat flux divergence is about the same as the vertical heat flux divergence.

Appendix 3.B From float trajectory to vertical velocity

At all four different experimental locations considered, turbulent vertical velocities in the ocean surface boundary layer (OSBL) are measured by the neutrally-buoyant Lagrangian floats. A typical float mission cycles between a downward profile to below the boundary layer, a ballasting segment during which the float settles on an isopycnal and thereby measures its own density, an upward profile back into the boundary layer, a Lagrangian drift during which the float continuously matched its density to that of the surrounding water, and a surfacing during which the float transmitted data and received commands via Iridium (*D'Asaro et al.*, 2014a). The length of one drift is about 18 hours for measurements at station Papa and under typhoon Fanapi, and about $2 \sim 3$ times shorter at Lake Washington. The float mission at the Labrador Sea was different. The floats were programmed to drift continuously for about two months after the initial one-week ballasting.

All measurements of pressure p are first corrected for atmospheric pressure variations and calibration offsets. The drifting pressure segment is also trimmed to remove pieces where the float is still adjusting the mode switch, and pieces where the float is trapped near the surface or the bottom of the boundary layer. Numerical simulations of imperfect floats (*Harcourt and D'Asaro*, 2010) have suggested that the skewness of the pressure [$S_p = \overline{(p-\overline{p})^3}/(\overline{(p-\overline{p})^2})^{3/2}$] is a good predictor of the excess float buoyancy that can bias the computed boundary layer depth low, the vertical velocity variance high, and the vertical velocity skewness high. Therefore, periods of Lagrangian drift are filtered by requiring the magnitude of the pressure skewness to remain below 1. Drifts shorter than 3 hours are not used. Float-measured pressure is converted to depth and the vertical velocity is computed from the centered difference of the depth variation. To suppress the instrumental noise, these raw vertical velocities are further filtered by a 5-point running median filter, and by a second-order Butterworth filter with a cutoff frequency of 0.1 $rad\,s^{-1}$ applied forward and backward across each Lagrangian drift (*D'Asaro et al.*, 2014a).

Appendix 3.C Float size correction

Because the size of the float is larger than the smallest eddy in the OSBL, the bulk variance w^2_{rmsF} of the float-measured vertical velocity from Appendix 3.B underestimates the total variance. This float size effect can be modeled by a universal spectrum of Lagrangian vertical acceleration (*Lien et al.*, 1998)

$$\Phi^L_{aa}(\omega) = 1.8\epsilon\left[1+\left(2.2\frac{\omega_0}{\omega}\right)^4\right]^{-0.5}\left[1+\left(0.63\frac{\omega}{\omega_L}\right)^2\right]^{-0.8}, \tag{3.5}$$

where ω is the angular frequency in radians, ϵ is the dissipation rate of the turbulent kinetic energy, ω_0 is the large eddy frequency, and $\omega_L = (\epsilon L_f^{-2})^{1/3}$ is the float size frequency with L_f the half-length of the float, 0.33 m for the Labrador Sea floats and 0.46 m for other floats. Following the method of *D'Asaro et al.* (2014a), we fit the model spectrum to the Lagrangian acceleration spectrum estimated from each drift

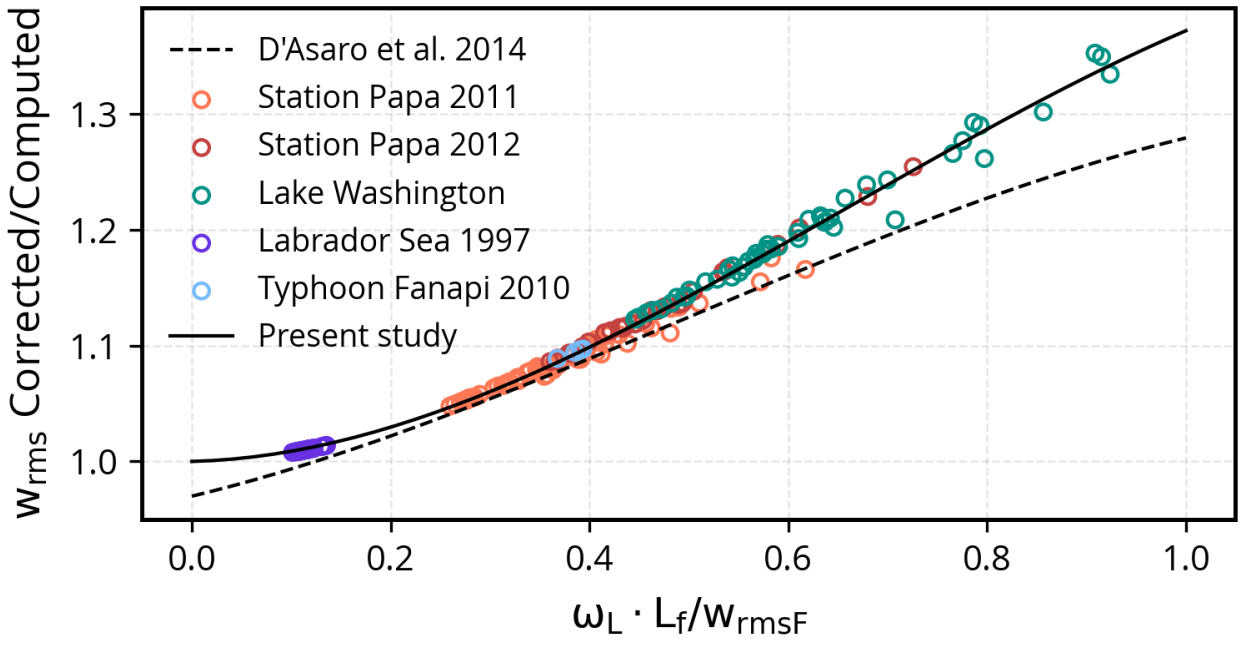

Figure 3.4: Scaling of the float size correction. The ratio w_{rmsC}/w_{rmsF} of float *rms* vertical velocity corrected for the float's finite size to the uncorrected value scales with the non-dimensional vertical velocity $w_{rmsF}(\omega_L \cdot L_f)^{-1}$ with a standard deviation of 0.006. The cubic polynomial fit used in this study is $-0.355x^3 + 0.706x^2 + 0.021x + 1$, where $x = \omega_L \cdot L_f / w_{rmsF}$.

segment. For the Labrador Sea data, the spectrum is estimated from each 3.56-day segment. The missing variance due to the finite float size is estimated as $\delta w^2_{rms} = \int \omega^{-2}\Phi^L_{aa0} \cdot d\omega - \int \omega^{-2}\Phi^L_{aa} \cdot d\omega$, where Φ^L_{aa0} is the model spectrum with ω_0 and ϵ from the fit but setting $L_f = 0$. The corrected bulk variance is $w^2_{rmsC} = w^2_{rmsF} + \delta w^2_{rms}$. Using the data from station Papa and Lake Washington, *D'Asaro et al.* (2014a) found that the fractional correction w^2_{rmsC}/w^2_{rmsF} is a universal function (their Figure S12) of the non-dimensional vertical velocity $(\epsilon L_f)^{1/3}/w_{rmsF}$. However, their empirical formula does not approach 1 in the limit of float size $L_f = 0$. Here we add two more data sets from typhoon Fanapi and the Labrador Sea and update the polynomial fit to give a better empirical formula (Figure 3.4). The new scaling of the float size correction is applied uniformly in depth to correct the vertical velocity variance in each drift.

Appendix 3.D Boundary layer depth

The boundary layer depth h, defined as the extent to which the boundary layer eddies can penetrate in the vertical, is determined using the bulk Richardson criteria *Large et al.* (1994). At station Papa and Lake Washington, the calculation is done internally within the one-dimensional KPP (*Griffies et al.*, 2015) simulation that is initialized from the float-measured temperature and salinity profile before each drift, and forced by surface fluxes from the nearby buoy measurements. The horizontal velocity in the single-column simulation is damped by a relaxation to zero on a 5-day time scale to represent the transfer of inertial energy to the ocean interior (*D'Asaro*, 1985) and avoid the build-up of strong inertial current shear (*Li et al.*, 2019).

For the other two locations, the boundary layer depth is approximated by a mixing depth describing the extent to which mixing is actively occurring. In the mixing layer, Lagrangian particles are uniformly distributed in the vertical and their mean depth is half of the mixing depth. Assuming the float samples the boundary layer uniformly, we estimate the mixing depth from the weighted moving mean of drifting pressure within a Hann window that is 20 times longer than the overturning time scale h/w_{rms}. Since the

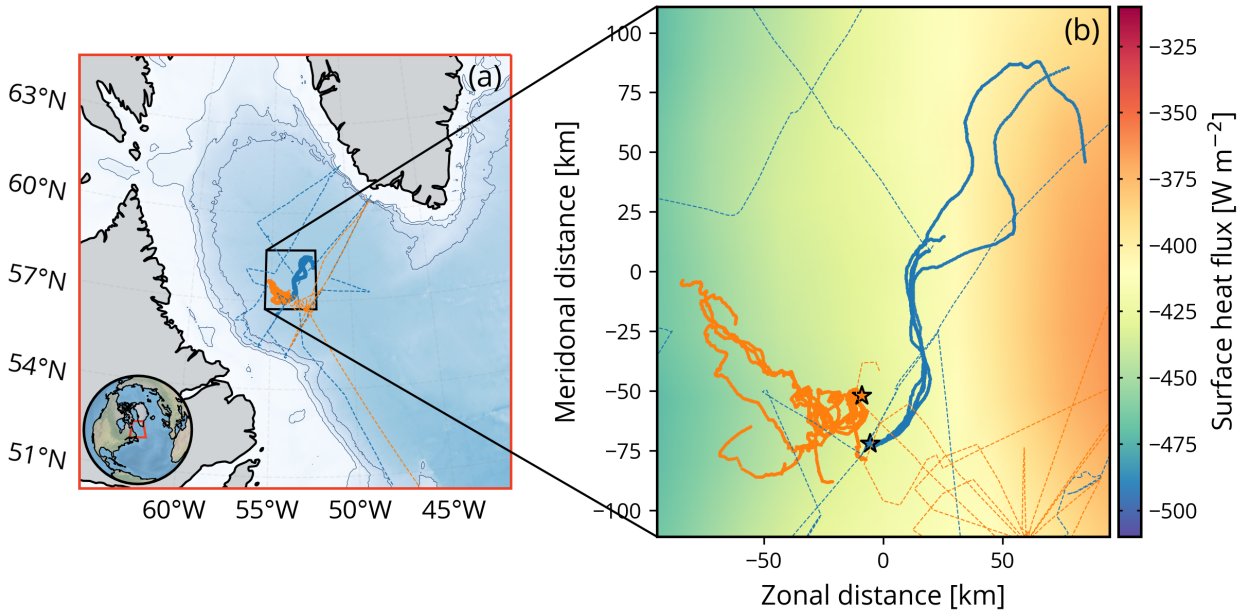

Figure 3.5: Ship tracks (dash lines) and float tracks (dots) in the Labrador Sea deep convection experiment (1997: blue; 1998: orange). The background color and thin lines in (a) show the bathymetry and isobaths of 500, 1500, and 2500 m. (b) Zoomed in view of various trajectories overlaid on the mean February surface heat flux map of 1997.

window width depends on h, the calculation is done recursively with some initial guesses of h and w_{rms} (*D'Asaro et al.*, 2014a). The results usually converge within a few iterations. For the Labrador Sea case, estimates of h are averaged across all floats. In the end, the boundary layer depth is further low-passed with a cut-off frequency of 72 hours for the Labrador Sea data and 12 hours for the rest.

Appendix 3.E Air-sea fluxes: Labrador Sea

Hourly surface fluxes from the ERA5 reanalysis (*Hersbach et al.*, 2020) are linearly interpolated to float positions (Figure 3.5), which are determined by acoustical tracking (*Steffen and D'Asaro*, 2002). But not all of them (4 of the 13 returning floats in 1997) were successfully tracked. For floats with no horizontal track, we use the mean horizontal

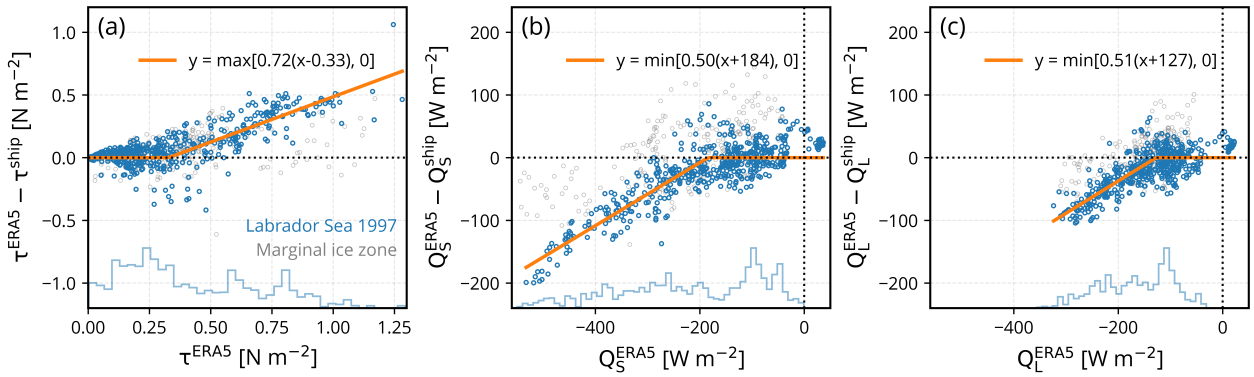

Figure 3.6: Corrections of ERA5 (a) surface stress τ, (b) sensible heat flux Q_S, and (c) latent heat flux Q_L in the 1997 Labrador Sea data set. Orange curves are least-square fits based on selected data (blue dots). Data in the marginal ice zone (gray dots) are not used for fitting. The bottom histograms in each panel show the probability distribution function of corresponding ERA5 fluxes interpolated to float trajectories.

positions of other tracked floats, but only before they diverged by a distance more than half of the horizontal resolution (0.25 degree) of the ERA5 flux field.

The ERA5 surface fluxes are also linearly interpolated to ship positions. The comparison between ERA5-interpolated fluxes and bulk fluxes calculated from shipboard observations using COARE 3.0 indicates that ERA5 fluxes are generally consistent with observations but the turbulent fluxes of momentum, sensible and latent heat are often biased high at high winds (Figure 3.6). This difference is largely consistent with a recent evaluation of the ERA5 reanalysis in similar subpolar regions around the Iceland and Greenland Seas (*Renfrew et al.*, 2021). Therefore we adjust the ERA5 turbulent fluxes using least-square fits of the bias (ERA5 - shipboard observation) after the interpolation to float trajectories. This correction assumes the ERA5 high wind bias only depends on the original ERA5 flux and the dependence does not vary spatially on spatial scales typical of ship-float distances.

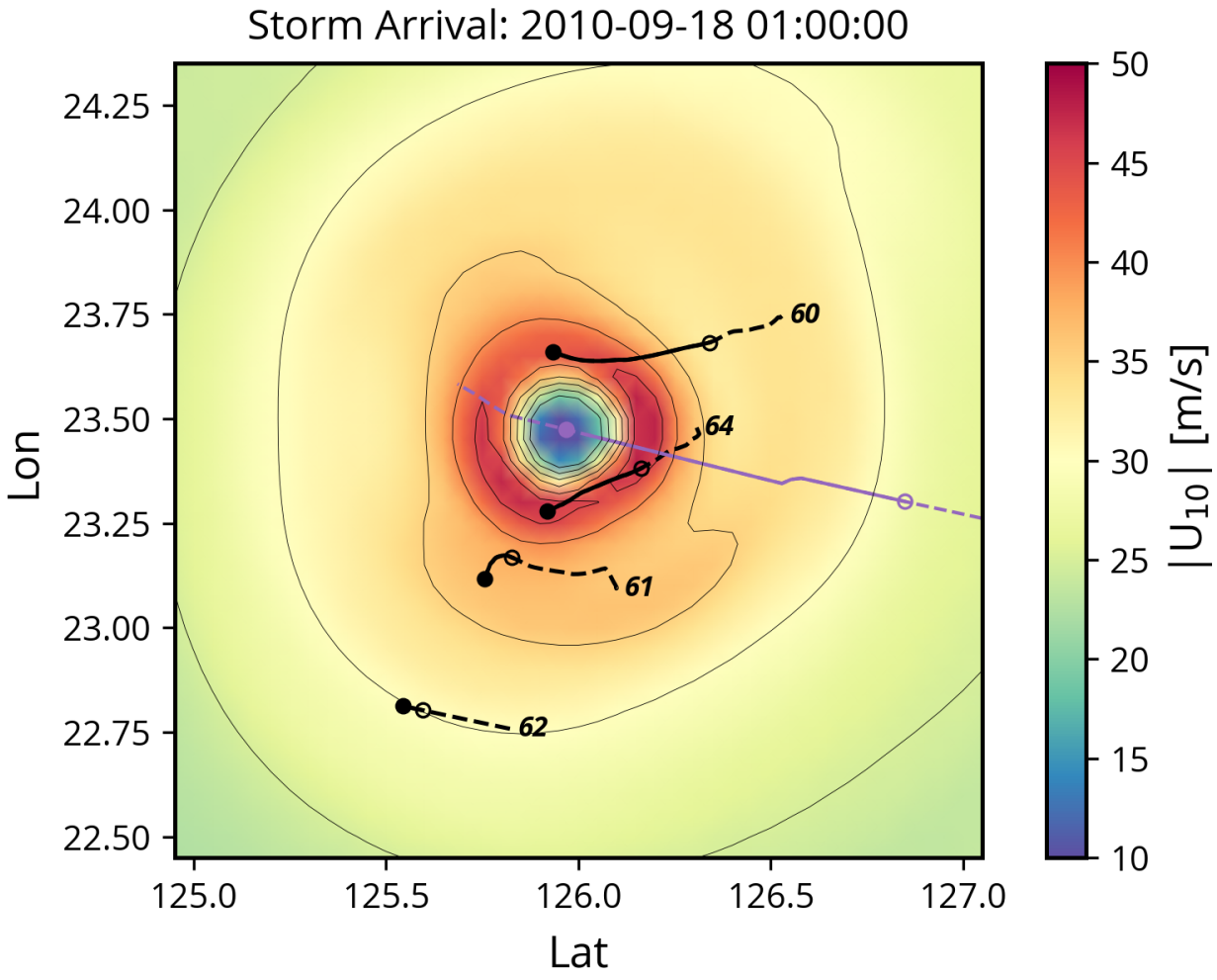

Figure 3.7: Map of Typhoon Fanapi surface wind field and Lagrangian float trajectories (black lines) when the storm arrives at the float locations. Gray contour lines correspond to wind speed from 20 to 45 m s^{-1}, with an interval of 5 m s^{-1}. The purple line shows the track of the storm center, approximately moving from east to west. Open circles indicate the positions of floats and the storm center when the wind speeds at float locations first become larger than 25 m s^{-1}. Filled circles are the corresponding locations when the storm arrives.

Appendix 3.F Air-sea fluxes: typhoon Fanapi

Four Lagrangian floats are deployed under typhoon Fanapi (2010), their horizontal positions (Figure 3.7) are recorded from GPS fixes at the time of deployment, at the one storm surfacing, and after the storm has passed. Interpolation between these is done by integrating the nearby Electromagnetic Autonomous Profiling Explorer float-measured horizontal velocities at the Lagrangian float depth and adjusting this curve to fit the GPS points (*D'Asaro*, 2012). One Lagrangian float passed the right-hand side of Fanapi's track, one passed the eye of Fanapi, and the rest two passed the left-hand side of Fanapi's track.

The 10 m wind speed (U_{10}) along the Lagrangian float track is linearly interpolated from the reconstructed wind fields of *Hsu et al.* (2019). Using the interpolated wind speed, the downwind drag coefficient ($\widetilde{C_{//}}$), and the stress angle (ϕ) are estimated from linear interpolations of the wind speed averaged results of *Hsu et al.* (2019), for the front-right and front-left, respectively. The front-right and front-left sectors are defined in the same way as in *Hsu et al.* (2019). We ignore the buoyancy effect on air-sea momentum transfer in this strongly wind-forced regime. The stress magnitude (τ) is calculated as $\tau = \rho_a \widetilde{C_{//}} |U_{10}|^2 \cdot \sqrt{1 + \tan^2 \phi}$, where ρ_a is the air density; and the stress direction is determined by the angle ϕ relative to the direction of U_{10}. We estimate the surface stress only when the wind speed is greater than 25 $m\,s^{-1}$ and only before the storm passes the float because the results of *Hsu et al.* (2019) are only valid in these conditions.

Surface heat and freshwater fluxes along the Lagrangian float track are estimated from linear interpolations of ERA5 fluxes. Because the ERA5 air-sea temperature (humidity) differences and wind are not accurate, and the ERA5 wind is smaller than the observation-based wind product of *Hsu et al.* (2019), we adjust the ERA5 sensible and latent heat fluxes (Figure 3.8) based on a combination of the wind ratio ($R_{wind} = |U_{10}^{obs}|/|U_{10}^{ERA5}|$) and the correction for air-sea temperature and humidity differences ($R_{\Delta T}$, $R_{\Delta q}$). Variations of the turbulent exchange coefficient for high winds are assumed small (*Black et al.*, 2007; *Sroka and Emanuel*, 2021). The correction for air-sea temperature and humidity differences

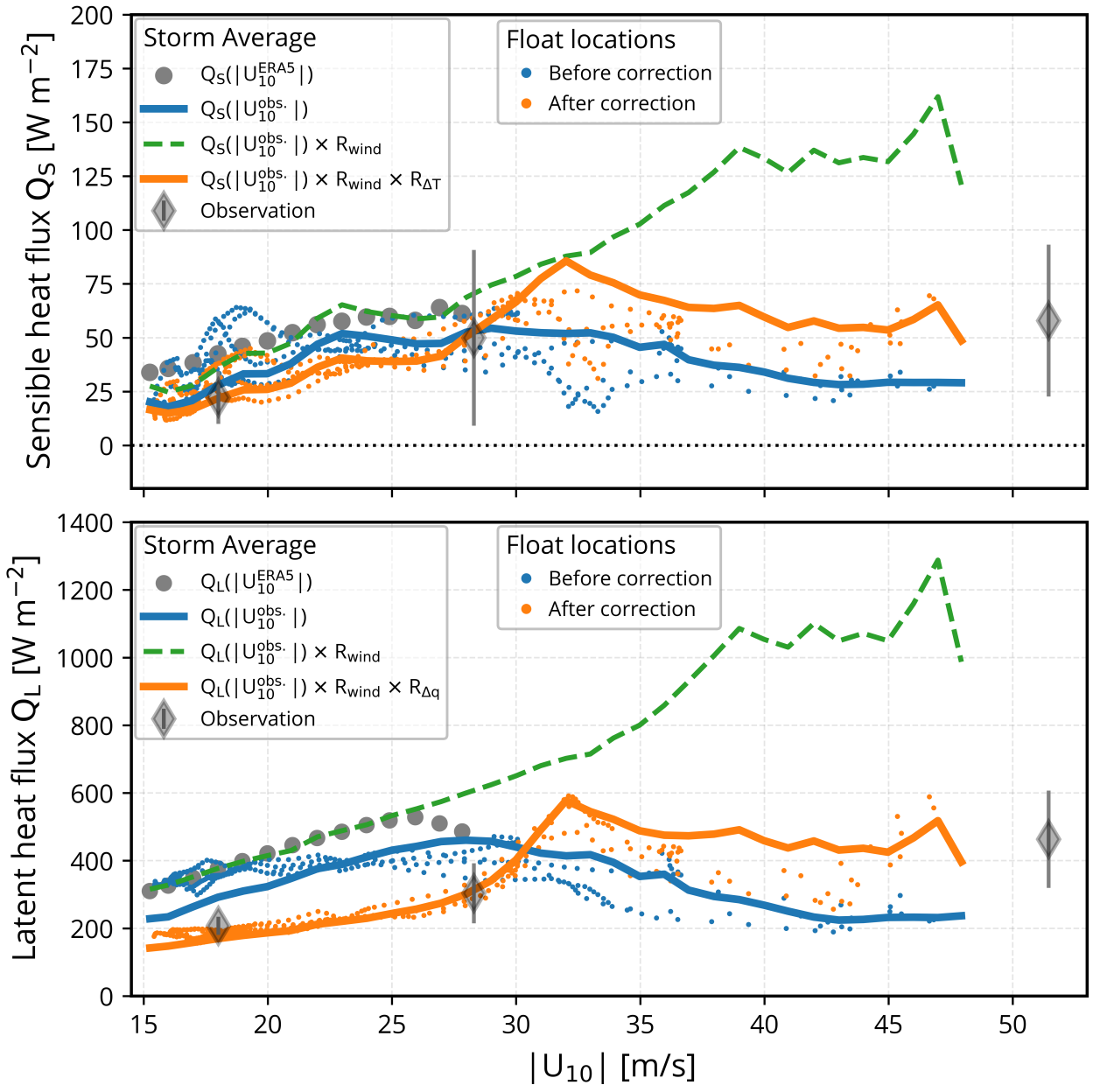

Figure 3.8: Corrections of ERA5 (a) sensible heat flux Q_S, and (b) latent heat flux Q_L in the typhoon Fanapi data set. The original storm-averaged ERA5 fluxes are shown as a function of both the ERA5 winds (gray solid circles) and the observed winds (blue lines). Storm-averaged fluxes adjusted for the wind ratio R_{wind} are shown in green dashed lines. Storm-averaged fluxes adjusted for both the R_{wind} and the air-sea temperature and humidity differences ($R_{\Delta T}$, $R_{\Delta q}$) are shown in orange lines. The gray diamonds with error bars (standard deviation) are observations of storm-averaged fluxes (*Lin et al.*, 2013). Blue and orange dots show the comparison of original fluxes and adjusted fluxes at float locations.

are tuned to match the storm-averaged, wind speed-dependent sensible and latent heat fluxes from observations (*Lin et al.*, 2013).

Appendix 3.G Stokes drift

The eastward (u^s) and northward (v^s) Stokes drift profiles are calculated by integrating the frequency spectra $E(f)$ over the measured frequency range $[f_1, f_c]$,

$$u^s = \frac{-16\pi^3}{g}\int_{f_1}^{f_c} f^3 b_1(f)E(f)e^{8\pi^2 f^2 z/g}df, \quad v^s = \frac{-16\pi^3}{g}\int_{f_1}^{f_c} f^3 a_1(f)E(f)e^{8\pi^2 f^2 z/g}df, \tag{3.6}$$

where g is the acceleration of gravity, a_1 and b_1 are the normalized coefficients of the directional Fourier series, and df is the frequency bandwidth. Following previous studies (*Harcourt and D'Asaro*, 2008; *Breivik et al.*, 2014), a high-frequency f^{-5} tail is added to the spectrum to account for unresolved small waves. The tail contribution to the Stokes drift is

$$u^s_{tail} = \frac{-16\pi^3 f_c^5 b_1(f_c)E(f_c)}{g}\left[\frac{e^{-\mu f_c^2}}{f_c} - \sqrt{\mu\pi}\cdot \mathrm{erfc}\left(f_c\sqrt{\mu}\right)\right], \tag{3.7}$$

$$v^s_{tail} = \frac{-16\pi^3 f_c^5 a_1(f_c)E(f_c)}{g}\left[\frac{e^{-\mu f_c^2}}{f_c} - \sqrt{\mu\pi}\cdot \mathrm{erfc}\left(f_c\sqrt{\mu}\right)\right], \tag{3.8}$$

with $\mu = -8\pi^2 z/g$. Though patching on an f^{-5} tail is a standard approach to extend the spectrum beyond what is feasibly measured, we recognize that it may result in an underestimation of Stokes drift on the order of 10% $\sim$ 30% if the highest measured cut-off frequency f_c is lower than the transition frequency between the equilibrium and saturation range (*Lenain and Pizzo*, 2020).

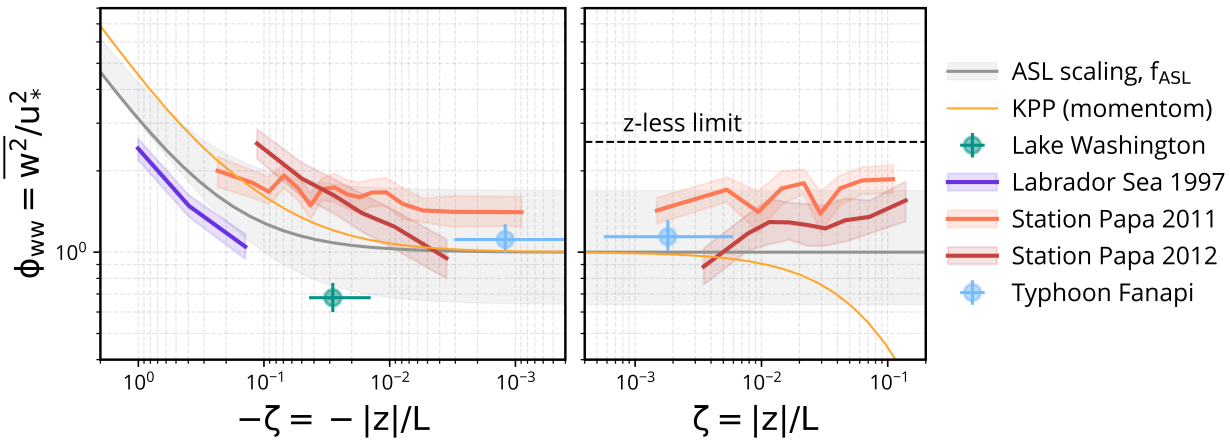

Figure 3.9: Same as Figure 3.2, but without float size correction.

Chapter 4

SCALING NEAR-SURFACE OBSERVATIONS OF TURBULENT VERTICAL VELOCITY IN THE OCEAN, PART II: BOUNDARY LAYER

Abstract

Surface wave-driven Langmuir turbulence increases both the vertical turbulent kinetic energy (TKE) $\overline{w^2}$, and its vertical turbulent transport $\overline{w^3}$ in ocean surface boundary layers. However, this process is absent in traditional scaling approaches that only consider wind and buoyancy effects, and in boundary layer mixing parameterizations based upon them. Here we introduce a consistent framework for scaling the vertical TKE with boundary layer forcing parameters. Using this framework, three separate asymptotic behaviors for the boundary layer averaged $\overline{w^2}$ are combined into a unified scaling with surface wind, wave, and buoyancy flux, across a revised non-dimensional space that measures the importance of wave forcing against wind forcing, and against buoyancy forcing. Predictions from the unified scaling are consistent with Lagrangian float measurements and published large eddy simulation results to within 7.5% and 6.7% on average, respectively. Float measurements of vertical velocity are used to obtain boundary layer profiles of the vertical TKE and the vertical turbulent transport of $\overline{w^2}$. In comparison with profiles in wave-free boundary layers, we find that in near-neutral conditions, with negligible wave forcing, observations generally agree with the traditional scaling. With strong wave forcing in near-neutral conditions, both the vertical TKE and its vertical transport are enhanced over a depth scale related to the e-folding scale of Stokes drift. In deep convection with strong buoyancy forcing, where the layer thickness is much larger than the Stokes e-folding scale, surface wave effects are less important; other factors such as planetary rotation might come into play.

4.1 Introduction

Turbulent vertical velocity in the ocean surface boundary layer (OSBL) directly contributes to vertical turbulent fluxes of heat, momentum, and trace gases, therefore critical for modeling the dispersion of material, the evolution of mixed layer depth, sea surface temperature, and other pivotal factors shaping Earth's climate. The current generation of climate models uses boundary layer mixing schemes [e.g., K-Profile Parameterization (KPP)] that rely on semi-empirical scaling of the vertical velocity to model the vertical eddy diffusivity (*Large et al.*, 1994; *Van Roekel et al.*, 2018). Historically, this scaling was based on an extrapolation of the Monin-Obukhov similarity theory to the entire boundary layer and measurements in the terrestrial atmospheric boundary layer (ABL). These suggest that the root mean square (*rms*) vertical velocity w_{rms} is controlled either by the surface stress τ when the wind-induced shear turbulence dominates, or by the surface buoyancy flux B_0 when the buoyancy effect takes precedence. In more common situations where both forcing mechanisms hold significance, the vertical velocity scales with a combination of the convective velocity (*Deardorff*, 1970) $w_* = (h \cdot B_0)^{1/3}$, where h is the boundary layer depth, and the friction velocity $u_* = (\tau/\rho_0)^{1/2}$, where ρ_0 the reference water density.

This traditional perspective on vertical velocity scaling, while concise and valuable, has faced many challenges as our understanding of turbulence in the OSBL evolves over time. A notable example of this evolution is the growing body of evidence pointing to higher vertical velocity variance $\overline{w^2}$ (or w_{rms}^2, the second moment of w) in the OSBL, substantiated by both field observations (*D'Asaro*, 2001; *Tseng and D'Asaro*, 2004; *Gerbi et al.*, 2009; *D'Asaro et al.*, 2014a; *Gargett and Grosch*, 2014) and turbulence-resolving large eddy simulations (LES) of wavy boundary layers (*Skyllingstad and Denbo*, 1995; *McWilliams et al.*, 1997; *Li et al.*, 2005; *Harcourt and D'Asaro*, 2008; *Van Roekel et al.*, 2012, and others). The enhancement of $\overline{w^2}$ is attributed to the presence of Langmuir turbulence, as the interaction between the current $\overline{u}$ and the Stokes drift u^s of surface waves (*Craik and Leibovich*, 1976),

or the Stokes shear force (*Suzuki and Fox-Kemper*, 2016), generates additional turbulent kinetic energy (TKE). Surface wave breaking may also play a role in triggering the Craik-Leibovich instability that leads to Langmuir turbulence (*Sullivan et al.*, 2007), but its effect is limited to a shallow layer spanning a few significant wave heights. By using LES that includes the Craik-Leibovich vortex force, the dimensionless bulk[1] vertical velocity variance $\langle \overline{w^2} \rangle / u_*^2$ has been found to depend on a non-dimensional Langmuir number that describes the relative importance of wind and Stokes drift forcing (*McWilliams and Sullivan*, 2000; *Harcourt and D'Asaro*, 2008; *Van Roekel et al.*, 2012; *Reichl et al.*, 2016). Various Langmuir number-dependent scaling relations have been proposed to quantify the enhanced $\langle \overline{w^2} \rangle / u_*^2$ in neutral conditions. These results are also incorporated into a variety of boundary layer mixing schemes to include the effect of Langmuir turbulence on eddy diffusivity. However, given the significant discrepancies reported among the current suite of Langmuir schemes (*Li et al.*, 2019), the development of Langmuir mixing parameterization is still far from complete.

Future efforts will benefit from a more comprehensive scaling of the Langmuir effect on vertical velocity, with a targeted emphasis on three aspects that have not been adequately addressed before. First, the existing Langmuir number-dependent scaling relations only represent the enhancement of Langmuir turbulence over shear turbulence, while the Langmuir effect in convective turbulence may be different (*Li and Fox-Kemper*, 2017). Thus, directly applying a neutral enhancement factor to the traditional scaling based on w_* and u_* has a potential risk of misrepresenting the Langmuir effect in conditions where surface buoyancy flux is important (*Li and Fox-Kemper*, 2017). In fact, such conditions are where most of the real world appears to be situated (*Li et al.*, 2019). Here we introduce a scaling framework that considers multiple turbulence generation mechanisms concurrently. Within this framework, we propose a generalized scaling for $\langle \overline{w^2} \rangle$ forced by varying combinations of wind, waves, and surface buoyancy flux.

---

[1]The vertical average over the boundary layer, denoted by $\langle\ \rangle$.

Second, present bulk scaling relations do not account for the varying degree of $\overline{w^2}$ enhancement at different depths, which is often weaker near the surface and bottom of the boundary layer (*Reichl et al.*, 2016). Applying a vertically-uniform enhancement factor to the wave-free eddy diffusivity profile would likely cause large errors near the surface and overentrainment at the mixed layer base. Although several variants of the KPP model have already considered the Langmuir effect on the vertical shape of eddy diffusivity (*Sinha et al.*, 2015; *Yang et al.*, 2015; *Reichl et al.*, 2016), these formulations lack support from observational data.

Last, there is currently no scaling relation for the Langmuir effect on the third moment $\overline{w^3}$ and the skewness [$S_w = \overline{w^3}/(\overline{w^2})^{3/2}$] of the turbulent vertical velocity. These higher-order statistics, although requiring considerably longer averaging time to achieve the same relative statistical significance as variance (*Lenschow et al.*, 1994), provide information on the turbulent transport of vertical TKE ($\overline{w^2}$) and the up-down asymmetry of the w probability distribution, both of which are widely used in high-order and mass-flux closure schemes (*Giordani et al.*, 2020; *Garanaik et al.*, 2022). LES studies have consistently shown that Langmuir turbulence exhibits a significantly more negative skewness and $\overline{w^3}$ (*McWilliams et al.*, 1997; *Sullivan et al.*, 2007, 2012) compared to pure shear turbulence. This distinction arises from the presence of narrow, intense downwelling jets within coherent Langmuir cells. However, information on this matter from observational data is still quite limited. In an initial effort to bridge these gaps and establish pertinent depth-dependent scaling relations, here we analyze a set of archived Lagrangian float (*D'Asaro et al.*, 1996; *D'Asaro*, 2003a) measurements of vertical velocity in the OSBL. The profiles of $\overline{w^2}$, $\overline{w^3}$, and w-skewness are examined in the traditional ABL scaling framework to isolate the impact of surface waves.

In Section 4.2, we present a scaling framework for the vertical velocity variance in the boundary layer. A key outcome of using this framework is the generalization of the scaling for $\langle\overline{w^2}\rangle$ to combine contributions from wind, waves, and surface buoyancy flux. In Section 4.3, we test the skill of the generalized $\langle\overline{w^2}\rangle$ scaling using data and also explore

the depth-dependent scaling of $\overline{w^2}$, $\overline{w^3}$, and w skewness. The results are summarized and discussed in Section 4.4.

4.2 Scaling Framework

We start by considering the 1-D steady state TKE equation, neglecting the turbulent and pressure transport:

$$\epsilon = -\overline{u'w'}\frac{\partial \overline{u}}{\partial z} + \overline{w'b'} - \overline{u'w'}\frac{\partial u^s}{\partial z}, \tag{4.1}$$

where ϵ is the TKE dissipation rate, $-\overline{u'w'}$ is the turbulent stress, z is the vertical coordinate defined as positive upward with zero at the surface, and $\overline{w'b'}$ is the turbulent buoyancy flux. The terms on the right-hand side represent the Eulerian shear production, the buoyancy production or suppression, and the Stokes shear production, respectively.

Since production and dissipation are the leading order term of the TKE budget over a significant portion of the OSBL (*Kukulka and Harcourt*, 2017), we anticipate a simple balance between them would lead to a physically motivated scaling for $\overline{w^2}$. In the following two subsections, we first review some previous scaling results derived using this balance and then extend it to include the Stokes shear production and propose a generalized scaling that combines contributions from all three production terms. For simplicity, we parameterize the dissipation as proportional to q^3/ℓ (*Mellor and Yamada*, 1982), where ℓ is a length scale and q is a velocity scale of the TKE ($q^2/2$). We also make the assumption of linearly decaying stress and buoyancy flux, such that $-\overline{u'w'} = u_*^2(1 + z/h)$, and $\overline{w'b'} = B_0(1 + z/h)$.

4.2.1 Shear and convective turbulence

In pure shear turbulence, the balance is approximately

$$\epsilon \sim \frac{q^3}{\ell} \sim \frac{w_{rms}^3}{\ell} \sim u_*^2(1 + z/h)\frac{u_*^2(1 + z/h)}{K_m}, \tag{4.2}$$

where the Eulerian shear $\partial\overline{u}/\partial z$ is related to the stress through an eddy diffusivity K_m by invoking the down-gradient diffusion assumption, $-\overline{u'w'} = K_m\partial\overline{u}/\partial z$, the TKE velocity

scale q is further approximated by the *rms* vertical velocity, following *Harcourt and D'Asaro* (2008). With a simple eddy diffusivity analogous to the KPP model, $K_m \sim w_{rms} \cdot \ell$, we have

$$\overline{w^2} \sim u_*^2(1 + z/h). \tag{4.3}$$

This relationship is consistent with the ABL local scaling (*Nieuwstadt*, 1984), in which $\overline{w^2}$ is approximately constant if normalized by the local turbulent stress, $u_*^2(1 + z/h)$ in this case. The vertical average of Equation 4.3 over the boundary layer gives $\langle\overline{w^2}\rangle \sim 0.5u_*^2$. LES of shear turbulence (*Li et al.*, 2005; *Harcourt and D'Asaro*, 2008) in the OSBL suggest that $\langle\overline{w^2}\rangle \approx 0.64u_*^2$, thus the constant of proportionality in Equation 4.3 is about 1.28.

Similarly, in purely convective turbulence, the balance is approximately

$$w_{rms}^3 \sim \ell \cdot B_0(1 + z/h) \quad \Rightarrow \quad \overline{w^2} \sim w_*^2(z/h)^{\frac{2}{3}}(1 + z/h)^2, \tag{4.4}$$

where the KPP length scale $\ell \sim |z|(1 + z/h)^2$ is used. Near the surface, this scaling reduces to $\overline{w^2}/w_*^2 \sim (z/h)^{2/3}$, equivalent to the (local) free convection limit of the surface layer scaling (e.g., Chapter 3), $\overline{w^2}/u_*^2 \sim (z/L)^{2/3}$. As a whole, this scaling is also largely consistent with the ABL convective scaling (*Lenschow et al.*, 1980, 2012; *Zhou et al.*, 2019),

$$\overline{w^2} = 1.8w_*^2(z/h)^{\frac{2}{3}}(1 + 0.8z/h)^2. \tag{4.5}$$

A notable distinction in this empirical scaling is the inclusion of an additional coefficient (0.8) when transitioning into stratified interiors to maintain a finite vertical TKE due to entertainment, which is ignored in the simple profile for the turbulent buoyancy flux in Equation 4.4. The corresponding bulk scaling of Equation 4.5 is $\langle\overline{w^2}\rangle \approx 0.31w_*^2$.

When shear and convective turbulence coexist, one may again use the production-dissipation balance to seek a combined expression for $\langle\overline{w^2}\rangle$. Unfortunately, this leads to a quartic equation with no manageable solution for scaling purposes. As an alternative approach, we leverage the established asymptotic scaling relations from above and combine their contribution to the bulk w_{rms}^3, instead of those to the bulk w_{rms}^2. While a linear combination may appear straightforward, it overlooks the interaction between

shear and convective turbulence. One crucial aspect of this interaction is the influence of convection-induced w_{rms} on Eulerian shear, mediated by the eddy diffusivity K_m. Therefore, we introduce a weight α_B for the shear turbulence part to account for the reduction (intensification) of Eulerian shear in convection (stratification), and another weight β_S for the convective turbulence part so that

$$\langle \overline{w^2} \rangle = \left(\alpha_B \cdot c_S u_*^3 + \beta_S \cdot c_B w_*^3 \right)^{\frac{2}{3}}, \tag{4.6}$$

where $c_S = 0.64^{\frac{3}{2}}$, $c_B = 0.31^{\frac{3}{2}}$. The weight function α_B may be seen as an extension and the bulk average of the surface layer non-dimensional Eulerian shear, which varies with stability and has a neutral value of 1. Although a more complex model is possible, we find the following simple expression for α_B works well,

$$\alpha_B = \frac{c_S u_*^3}{c_S u_*^3 + c_B w_*^3} = \frac{c_S}{c_S - c_B h/\kappa L}, \tag{4.7}$$

where κ is the von Kármán constant, L is the Obukhov length, and $h/\kappa L = -w_*^3/u_*^3$ is the bulk stability parameter. The weight function β_S represents the potential impact of shear turbulence on convective turbulence. Previous studies have shown that wind-driven shear turbulence can disrupt the formation of convective plumes (*Domaradzki and Metcalfe*, 1988) and diminish the role of convection. But this is a more subtle effect and seems even more so in the presence of Langmuir turbulence (*Li and Fox-Kemper*, 2017). Here we treat convection as independent of shear turbulence and set $\beta_S = 1$.

4.2.2 *Inclusion of Langmuir turbulence*

The consideration of Langmuir turbulence adds another production mechanism of TKE. Although Langmuir turbulence typically does not exist alone in reality, the scaling for Langmuir-induced $\langle \overline{w^2} \rangle$ is still a valuable asymptotic limit in guiding the development of a generalized scaling. A similar argument based on the production-dissipation balance suggests that

$$w_{rms}^3 \sim \ell \cdot u_*^2 (1 + z/h) \frac{\partial u^s}{\partial z} \quad \Rightarrow \quad \frac{\langle \overline{w^2} \rangle}{u_*^2} \sim \left(\frac{u_{SL}^s}{u_*} \right)^{\frac{2}{3}} = La_{SL}^{-\frac{4}{3}}, \tag{4.8}$$

where the vertical average of the length scale weighted Stokes shear production is approximated by the product of u_*^2 and a vertically filtered Stokes drift $u_{SL}^s = \langle u^s \rangle_{SL} - u_{ref}^s$, defined as the difference between $\langle u^s \rangle_{SL}$, the average of u^s in the surface layer ($-0.2 < z/h \leq 0$), and a reference value in the lower boundary layer ($z/h \approx -0.765$). This approximation is explained in more detail by *Kukulka and Harcourt* (2017).

The resulting dependence of $\langle \overline{w^2} \rangle / u_*^2$ on the surface layer Langmuir number La_{SL} is quantified in *Harcourt and D'Asaro* (2008). Their neutral Langmuir-inclusive scaling can well characterize the total contributions from shear and Langmuir turbulence but is not applicable under conditions with large surface buoyancy flux. When all three production terms are important, a linear combination of the neutral Langmuir-inclusive scaling and the convective scaling (Equation 4.5) is not sufficient to scale the total bulk w_{rms}^3, as the enhancement due to Langmuir turbulence behaves differently in shear-dominated and convection-dominated regimes (*Li and Fox-Kemper*, 2017). Although there may be other factors in play, we think the difference is related to the fact that with destabilizing surface buoyancy fluxes, the Eulerian shear production is further reduced. In contrast, the Stokes shear production remains about the same in convection. Thus the contribution of shear turbulence in the neutral Langmuir-inclusive scaling should be adjusted as the importance of buoyancy effects changes.

However, it is not immediately clear how one could separate the part due to shear turbulence from the neutral Langmuir-inclusive scaling because it also varies with the strength of Langmuir turbulence. Specifically, the Stokes drift shear can strongly affect the Eulerian shear by elevating w_{rms} (just like convection), and additionally, by supporting most of the stress near the surface, leaving a small amount of stress in balance with the diffusion of Eulerian momentum (*Harcourt*, 2013). The separation becomes convenient if the neutral Langmuir-inclusive scaling is in a form similar to Equation 4.6, such as

$$\langle \overline{w^2} \rangle = \left(\alpha_L \cdot c_S u_*^3 + \gamma_S \cdot c_L u_*^3 La_{SL}^{-2} \right)^{\frac{2}{3}}, \tag{4.9}$$

where $\alpha_L = c_S / \left(c_S + c_L La_{SL}^{-2} \right)$ is an approximation for the Langmuir-induced reduction

of Eulerian shear, $\gamma_S = 1$ signifies that shear turbulence exerts no influence on Langmuir turbulence, $c_L = 0.498$ is a constant determined by minimizing the square errors between Equation 4.9 and the scaling of *Harcourt and D'Asaro* (2008). This approximated scaling (Equation 4.9) is almost identical to the original formulation (*Harcourt and D'Asaro*, 2008), with a coefficient of determination R^2 of about 0.987 (Figure 4.2c). The two terms in Equation 4.9 are the contribution of Eulerian and Stokes shear production to the bulk w^3_{rms}, respectively. Following the same manner, we can write the generalized scaling as

$$\langle \overline{w^2} \rangle = \left(\alpha_B \alpha_L \cdot c_S u_*^3 + \beta_S \beta_L \cdot c_B w_*^3 + \gamma_S \gamma_C \cdot c_L u_*^3 La_{SL}^{-2} \right)^{\frac{2}{3}}, \tag{4.10}$$

where β_L and γ_C represent the potential two-way influence between Langmuir and convective turbulence. Here we assume that Langmuir and convective turbulence do not interact and set $\beta_L = \gamma_C = 1$. Strictly speaking, this generalized scaling is invalid in strongly stable conditions because the buoyancy adjustment of Eulerian shear α_B blows up as the stabilizing buoyancy flux (negative w_*^3) becomes significant. Since the turbulence under such conditions is relatively less understood, and the data sets used for comparison only extend to weakly stable conditions [$-w_*^3/u_*^3 \leq \mathcal{O}(1)$, Figure 4.1b and 4.1d], a more accurate representation of this forcing scenario is left for future research. The skill of this scaling is tested in Section 4.3.

Previous studies (*Belcher et al.*, 2012) have identified two non-dimensional parameters, $La_t = (u_*/u_0^s)^{1/2}$, where u_0^s is the surface Stokes drift, and $h/L_L = w_*^3/u_*^2 u_0^s$, where L_L is the Langmuir stability length, as the basis of a regime diagram that maps out the contribution of each type of turbulence to the dissipate ϵ_m in the middle of the OSBL. These two parameters represent the importance of the Eulerian shear production and the buoyancy production or suppression, relative to the Stokes shear production in a bulk sense, respectively. Such a regime diagram[2] is shown in Figure 4.1a and 4.1b for conditions of destabilizing and stabilizing surface buoyancy flux, separately. Based on the

[2]Note that we use the square of Langmuir number as the horizontal axis to keep it consistent with the vertical axis in terms of representing the ratio of bulk-averaged production terms.

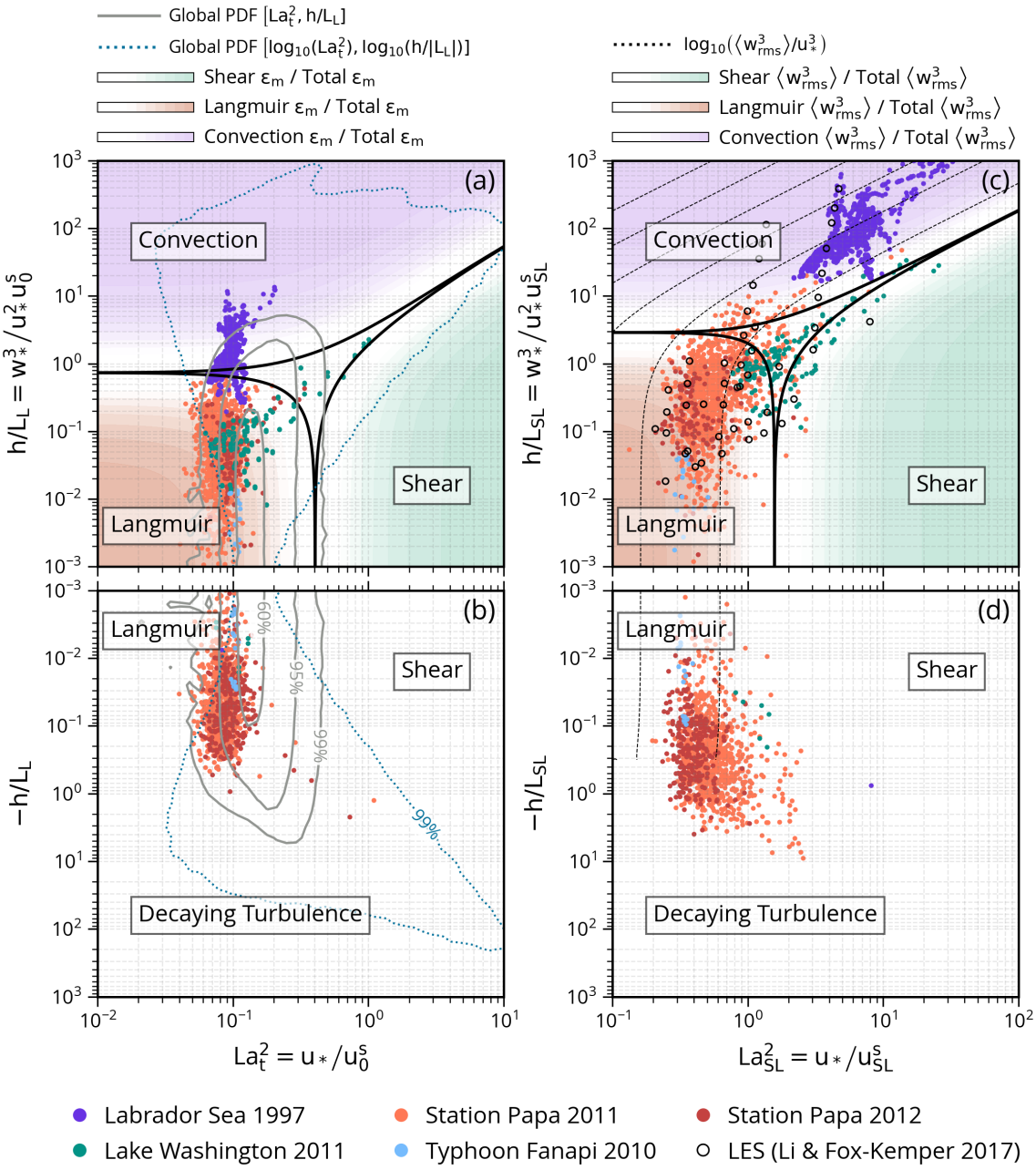

Figure 4.1: Turbulence regime diagrams for the OSBL under conditions of (a, c) destabilizing and (b, d) stabilizing surface buoyancy flux. Background colors in (a) and (c) show the fractions (50% ∼ 100%) of the dissipation rate ϵ_m and the bulk w^3_{rms} contributed by each type of turbulence, according to the scaling of *Belcher et al.* (2012) and Equation 4.10, respectively. The 50% contours of these fractions are shown in black lines. Gray contours in (a) and (b) show the joint probability distribution function (PDF) of La_t^2 and h/L_L, indicating 60%, 95%, and 99% of occurrences across global oceans (*Li et al.*, 2019). The observations and LES cases are overlaid as colored dots.

generalized scaling (Equation 4.10), we can construct a similar regime diagram, specifically for the non-dimensional bulk vertical TKE that depends on La_{SL} and $h/L_{SL} = w_*^3/u_*^2 u_{SL}^s$,

$$\frac{\langle \overline{w^2} \rangle}{u_*^2} = \left(\alpha_B \alpha_L \cdot c_S + c_B \frac{h}{L_{SL}} La_{SL}^{-2} + c_L La_{SL}^{-2} \right)^{\frac{2}{3}}, \tag{4.11}$$

where the unity factors β_S, β_L, γ_S, and γ_C in Equation 4.10 are omitted hereafter, L_{SL} is the Langmuir stability length defined using u_{SL}^s instead of u_0^s. This new regime diagram for the bulk vertical TKE is shown in Figure 4.1c and 4.1d for conditions of destabilizing and stabilizing surface buoyancy flux, separately.

4.3 *Results*

To investigate the bulk and the depth-dependent scaling of vertical velocity in the OSBL, we use the same observational data sets as those in Chapter 3. These include multiple Lagrangian float measurements and accompanying wave and meteorological data collected at station Papa (2011 and 2012), Lake Washington (2011), Labrador Sea (1997), and under typhoon Fanapi (September 2010) in the western Pacific Ocean. Details of the data processing are described in Chapter 3. In addition, we also include the LES data from *Li and Fox-Kemper* (2017) in the bulk scaling. The non-dimensional parameter space covered by these data and a typical year of the global oceans (*Li et al.*, 2016, 2019) are displayed in Figure 4.1.

4.3.1 *Bulk vertical velocity variance*

The generalized scaling for $\langle \overline{w^2} \rangle$ is tested here, using data spanning a broad range of the non-dimensional parameter space (La_{SL}, h/L_{SL}) (Figure 4.1c and 4.1d). Float measurements of w^2 are evenly divided into segments of about 40 degrees of freedom. The degree of freedom reflects the number of statistically independent measurements and is defined as $n\Delta t/T$, where n is the number of data, Δt is the sampling period, and $T = 2\overline{h/w_{rms}}$ is the time scale for a round trip overturn averaged over the entire

experiment. Within each segment, hourly averages of w^2 are normalized by hourly u_*^2 and weighted averaged in z/h bins of about 2 degrees of freedom. The bulk average of $\overline{w^2}/u_*^2$ is then computed from each profile. The quality of each bulk average is evaluated by comparing the cumulative distribution function (CDF) of z/h within the segment to that of an ideal uniform distribution. Segments with an *rms* CDF deviation larger than 0.1 and those with a mean z/h outside $[-0.6, -0.4]$ are not used. The screened bulk variance is further averaged in $(La_{SL}^{-2}, w_*^3/u_*^3)$ coordinate and shown in Figure 4.2a as scatter points, along with the prediction from the generalized scaling (Equation 4.10). Although not a perfect match, the observations are generally consistent with the generalized scaling, without any parameter tuning. Small deviations from the prediction are usually within the 95% confidence interval of measurements.

The typhoon Fanapi data has a relatively large deviation, probably because the simulated surface waves (*Zhou et al.*, 2022) have smaller wind-wave misalignment angles. The Labrador Sea data is significantly lower than both the generalized and the asymptotic convective scaling. This can be attributed to several different processes not considered in the scaling arguments. First, the thermal expansion coefficient α of seawater increases with pressure, leading to a thermobaric effect that can enhance the turbulent buoyancy flux and further energize convective plumes. Second, lateral re-stratification can effectively decrease the turbulent buoyancy flux profile and suppress boundary layer turbulence. Last, deep convection at the Labrador Sea is usually suppressed by the Coriolis effect as the boundary layer depth is larger than the rotational depth scale $B_0^{1/2} f^{-3/2}$, where f is the Coriolis frequency.

Considering the thermobaric effect, *Garwood et al.* (1994) showed that the boundary layer average of the buoyancy flux is enhanced by a factor $1 + h/3h_\alpha$, where h_α is the thermobaric depth scale defined as the ratio of α to $|\partial\alpha/\partial z|$ at the surface. For average conditions during the 1997 Labrador Sea experiment, the boundary layer depth h is about 823 m, h_α is about 3205 m, suggesting that $\overline{w^2}/w_*^2$ should have been 8.6% higher if the thermobaric effect is included. Based on estimates of the lateral heat flux divergence

in 1997 (see appendix 3.A), the lateral effect likely cancels the enhancement due to the thermobaricity. Therefore, we speculate that the smaller $\langle\overline{w^2}\rangle$ at the Labrador Sea is a result of the Coriolis effect on deep convection, which we discuss more in the following subsection on the depth-dependent scaling. If we vary the coefficient c_B in Equation 4.10 to represent the modulation of vertical TKE by Earth's rotation, we find $c_B = 0.127$ gives the best match with the Labrador Sea data.

The skill of the generalized $\langle\overline{w^2}\rangle$ scaling is perhaps more readily shown in the direct comparison of observations with the corresponding predictions (Figure 4.2b). These predictions exhibit a close match to the observations ($R^2 = 0.805$, excluding the gray Labrador Sea data), with a mean absolute percentage error of approximately 7.5% (blue shading). An even better agreement with the LES results of *Li and Fox-Kemper* (2017) is also shown in Figure 4.2c, in which the LES data have been separated into cases with and without surface waves. The predictions of the generalized scaling agree better with the wave-inclusive LES data (mean absolute percentage error $\sim$ 6.7%) than with the wave-free LES data. This difference is likely due to the stronger rotational suppression of vertical mixing in cases with no Craik-Leibovich vortex force, or the imposed wall-bounded near-surface similarity relations that are maybe not valid in the ocean. Nonetheless, the generalized scaling still predicts the majority of the $\langle\overline{w^2}\rangle$ variations with an accuracy of about 15% (blue shading). Note that all predictions in Figure 4.2b and 4.2c are calculated with canonical parameter values, except the purple marker for the Labrador Sea, which uses $c_B = 0.127$ in Equation 4.10. Other ways of combining the various asymptotic scaling relations in Section 4.2 are also tested. In general, we find that combinations of the bulk w_{rms}^3 scaling perform better than those using the bulk w_{rms}^2 scaling, probably because the former is energetically consistent with the production-dissipation balance of TKE.

Based on the generalized scaling, a neutral $\langle\overline{w^2}\rangle$ can be defined as

$$\langle\overline{w^2}\rangle_n = \left(\langle\overline{w^2}\rangle^{\frac{3}{2}} - c_B w_*^3\right)^{\frac{2}{3}} \tag{4.12}$$

to remove the buoyancy effect. Values of neutral $\langle\overline{w^2}\rangle / u_*^2$ in observations are computed

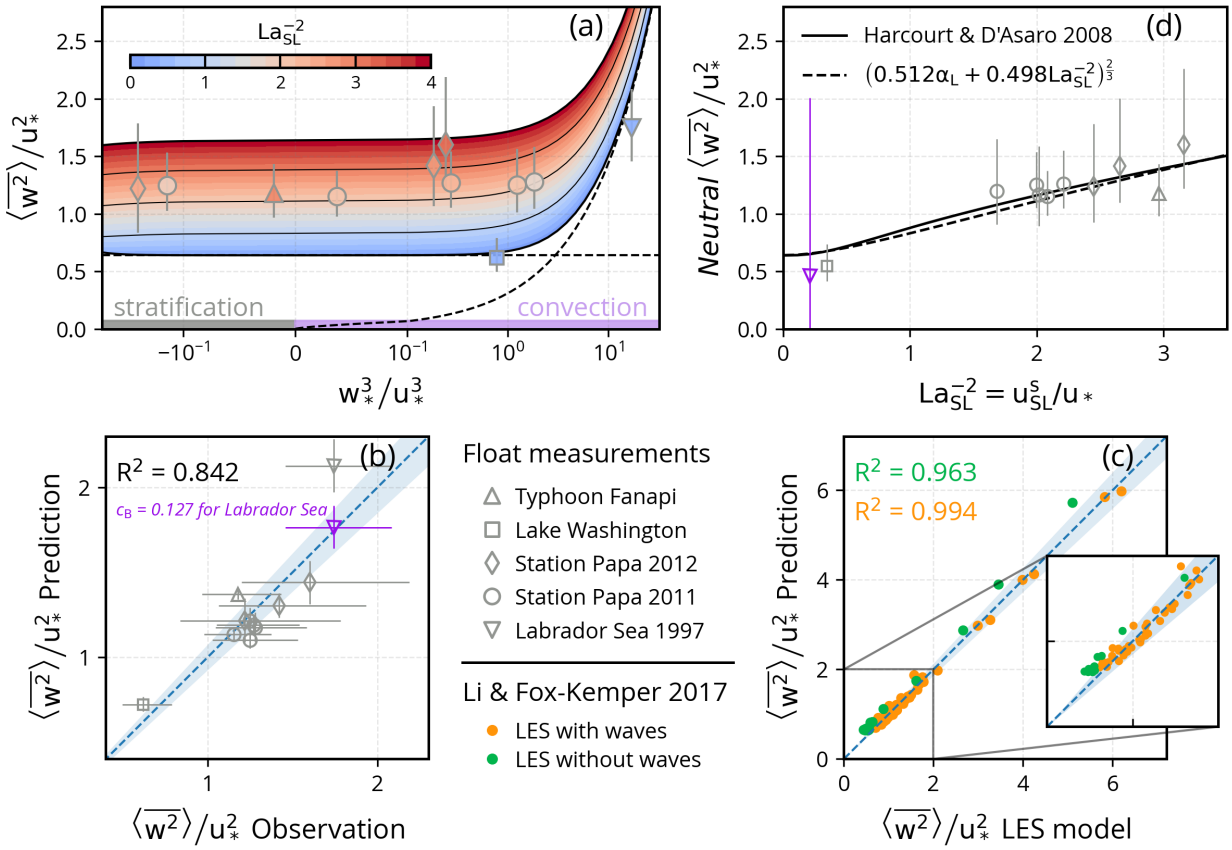

Figure 4.2: Scaling of the bulk vertical velocity variance $\langle \overline{w^2} \rangle$. (a) Time- and depth-averaged measurements of w^2 over the boundary layer are normalized by u_*^2 and plotted against time-averaged w_*^3/u_*^3. Scatter points with different markers show observations from different data sets, with error bars indicating the 95% confidence interval, and marker color corresponding to the mean value of La_{SL}^{-2} within the averaging window. Dash lines are the asymptotic scaling relations for pure shear turbulence (0.64) and pure convective turbulence ($0.31 w_*^2/u_*^2$). The colored contours show the prediction of $\langle \overline{w^2} \rangle / u_*^2$ from the generalized scaling (Equation 4.10). Note the horizontal axis is linear between -10^{-1} and 10^{-1} but logarithmic elsewhere. (b,c) Direct comparison of (b) float-measured $\langle \overline{w^2} \rangle / u_*^2$ and (c) LES-modeled $\langle \overline{w^2} \rangle / u_*^2$ (*Li and Fox-Kemper*, 2017) with the prediction from the generalized scaling (Equation 4.10). The blue shadings show the mean absolute percentage error [7.5% in (a), 6.7% in (b) for orange points] of the one-to-one correspondence. (d) The neutral $\langle \overline{w^2} \rangle / u_*^2$ estimated from measurements as a function of La_{SL}^{-2}, compared to the neutral Langmuir-inclusive scaling of *Harcourt and D'Asaro* (2008), and the approximation (Equation 4.9) used in the generalized scaling (Equation 4.10).

following Equation 4.12 with $c_B = 0.127$ for the Labrador Sea data and $c_B = 0.31^{\frac{3}{2}}$ for the rest (Figure 4.2d). As previously reported in *D'Asaro et al.* (2014a), the observed neutral values of $\langle\overline{w^2}\rangle$ agree with the scaling of *Harcourt and D'Asaro* (2008) and its approximation (Equation 4.9). The agreement seems better here, maybe because the buoyancy contribution is removed in a better way.

4.3.2 *Profiles of vertical velocity variance*

The exact mechanism of how Langmuir and convective turbulence, each with its own characteristic length and velocity scale, interact and modify the vertical structure of $\overline{w^2}$ is poorly understood. The reported weak interaction between Langmuir and convection in the bulk scaling does not imply the same for the profile shape. Here we do not attempt to address this challenging problem, instead, we examine the asymptotic scaling of $\overline{w^2}$ profile in the convective and the Langmuir-shear regime separately, and highlight the impact of surface waves. Therefore, measurements in the OSBL are divided into two groups, one in strongly convective conditions, and the other in near-neutral conditions, according to the importance of the buoyancy effect. The classification uses the generalized $\langle\overline{w^2}\rangle$ scaling (Equation 4.10), in which the importance of buoyancy is measured by r_B, the fraction of the bulk w_{rms}^3 that is contributed by the buoyancy effect.

In the first group ($r_B > 0.5$), convection is the largest contributor to the bulk vertical TKE; measurements of w^2 are normalized by w_*^2 and bin averaged in the z/h coordinate (Figure 4.3a). Only the Labrador Sea deep convection site has enough data to resolve the vertical structure of $\overline{w^2}$ in this group. These deep convection data are compared to the empirical convective scaling relations (Equation 4.5) established in the ABL (*Lenschow et al.*, 1980). Just like the bulk average, the $\overline{w^2}$ profile in the Labrador Sea is overall smaller than the ABL convective scaling. The observed vertical structure is moderately consistent with the ABL convective scaling, except that the observed maximum $\overline{w^2}$ is slightly smaller ($0.38w_*^2$ as opposed to $0.48w_*^2$), and the depth of the maximum is also shallower ($0.2h$

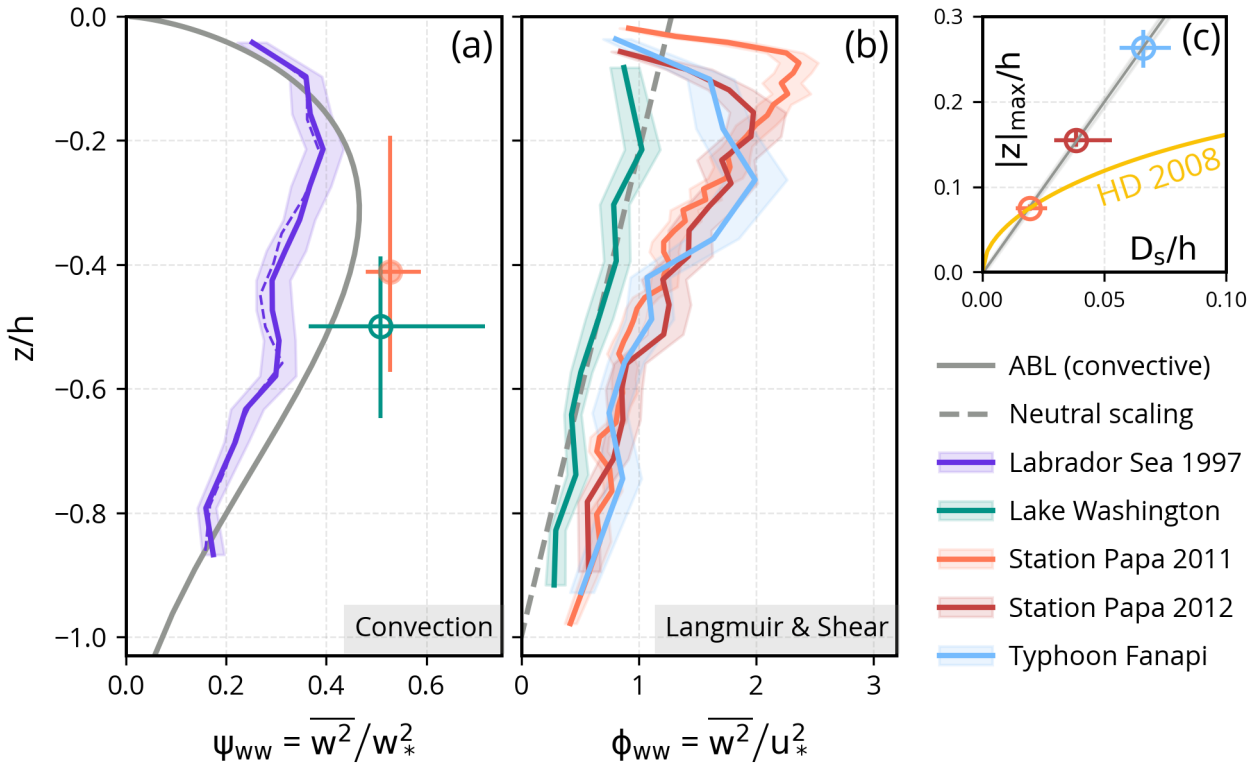

Figure 4.3: Scaling of the vertical velocity variance profiles in the OSBL under (a) strongly convective and (b) near-neutral conditions. Lagrangian float measurements are averaged in bins of about the same degrees of freedom [5 in (a); 10 in (b)], and placed at the median values of z/h. Open circles in (a) have degrees of freedom less than 5. Color shadings of observations and horizontal error bars show the 95% bootstrap confidence intervals of the mean and vertical error bars show the lower and upper quartiles of z/h. Empirical functions for the corresponding ABL convective scaling *Lenschow et al.* (1980) and neutral scaling are shown by the gray solid and dashed lines, respectively. (c) The depth of peak variance $|z|_{max}$ in near-neutral conditions scales with the penetrative scale D_S of Stokes drift. The gray line is a linear fit $|z|_{max}/h = 4.02 D_S/h$. The relevant scaling from *Harcourt and D'Asaro* (2008), $|z|_{max}/h = 0.22\sqrt{\tanh(6D_S/h)}$, is shown in yellow (HD2008).

as opposed to $0.3h$). This small deviation from the ABL convective scaling meets the expectation for rotation-constrained convective flow, in which the importance of rotation is measured by the natural Rossby number $Ro_* = B_0^{1/2} f^{-3/2} h^{-1}$ (*Maxworthy*, 1997, and others). We find the Labrador Sea $\overline{w^2}$ profile, with $Ro_* \sim 0.2$ on average, is highly similar to the LES result of the moderate Ro_* case reported by *Mironov et al.* (2000).

In the second group ($|r_B| < 0.5$), Langmuir and shear turbulence are the major contributors to the bulk vertical TKE; measurements of w^2 are normalized by u_*^2 and bin averaged in the z/h coordinate (Figure 4.3b). Data from Lake Washington, station Papa, and typhoon Fanapi are compared to the neutral scaling relations, $\langle \overline{w^2} \rangle = 1.28 u_*^2 (1 + z/h)$. The lake $\overline{w^2}$ profile is generally consistent with the neutral scaling, as expected from the small Stokes drift (Figure 4.2c). The other three profiles have significantly higher $\overline{w^2}$ throughout the boundary layer. This elevation of $\overline{w^2}$ is much stronger in the upper half of the layer, with a subsurface maximum of about $2u_*^2 \sim 3u_*^2$. Both the depth $|z|_{max}$ and the magnitude (not shown) of the $\overline{w^2}$ maximum are proportional to the e-folding decay scale D_S of the Stokes drift profile (Figure 4.3c). A linear fit $|z|_{max}/h = 4.02 D_S/h$ can accurately scale the depth of $\overline{w^2}$ peak. However, we note this behavior is slightly different than that in LES results of *Harcourt and D'Asaro* (2008), in which $|z|_{max}$ approaches a maximum of $0.22h$ as D_S increases. These ocean $\overline{w^2}$ profiles, measured in conditions with La_{SL}^{-2} typically ranging from 1.5 and 3, are overall consistent with LES results of Langmuir turbulence (*McWilliams et al.*, 1997; *Harcourt and D'Asaro*, 2008, and others).

4.3.3 *Profiles of the third moment and the skewness of vertical velocity*

The depth-dependent scaling of $\overline{w^3}$ is also explored in tandem with the w skewness profile. Here we assume the same turbulence regime defined using the generalized $\langle \overline{w^2} \rangle$ scaling also applies to higher-order velocity statistics. For the scaling of $\overline{w^3}$, measurements of w^3/w_*^3 and w^3/u_*^3 are bin averaged in the z/h coordinate (Figure 4.4a and 4.4b) for data in the convective ($r_B > 0.5$) and Langmuir-shear ($|r_B| < 0.5$) regime. Data

in the convective regime are also compared to an empirical ABL scaling relation $\overline{w^3} = -w_*^3(|z|/h)(1+0.7z/h)^3$ proposed by *Gryanik and Hartmann* (2002). Since the atmospheric convection is initiated from the bottom while the oceanic convection is the opposite, a negative sign is added to the ABL scaling to compare with the ocean data. Observed $\overline{w^3}$ profiles are predominantly negative in all cases, indicating a downward flux of vertical TKE. The profile of $\overline{w^3}$ in deep convection differs from the ABL scaling, especially in the upper half of the boundary layer, where the observation shows a vertical decay of $\overline{w^3}$ to almost 0 near $z = -0.2h$. The bulk average of the deep convection $\overline{w^3}$ is about $-0.08w_*^3$, about 40% smaller than that of the ABL scaling in magnitude. This difference is again likely a result of the rotational effect since LES results of rotating convection (*Mironov et al.*, 2000) suggest that the $\overline{w^3}$ profile becomes flatter and the turbulent transport of vertical TKE is suppressed as the rotation gets stronger. Profiles of $\overline{w^3}/u_*^3$ in the Langmuir-shear regime all exhibit a similar shape as the variance profile, but the effect of Langmuir turbulence on vertical TKE flux is more pronounced. This is shown by the much larger amplification of ocean data over the lake data (Figure 4.4b). The depth of the subsurface minimum $\overline{w^3}$ also seems to scale with the penetration depth of Stokes drift. These similarities suggest that the $\overline{w^3}/u_*^3$ profile in Langmuir and shear regimes may be sufficiently described by an empirical function that depends on three non-dimensional parameters: La_{SL}, D_S/h, and z/h. The development of this empirical formula is currently in progress.

For the scaling of w skewness, measurements of w^3 and w^2 are bin averaged in the z/h coordinate, and the ratio $\overline{w^3}/(\overline{w^2})^{3/2}$ is shown in Figure 4.4c and 4.4d for data in the convective ($r_B > 0.5$) and Langmuir-shear ($|r_B| < 0.5$) regime, respectively. The observed w skewness profiles are primarily negative throughout the boundary layer in all cases, indicating a persistent pattern of stronger and narrower downward motions than upward motions in the OSBL. Likely due to the rotational constraint, the Labrador Sea skewness profile behaves differently from the structure commonly seen in the convective ABL, in which the magnitude of skewness tends to increase from the surface, reaching

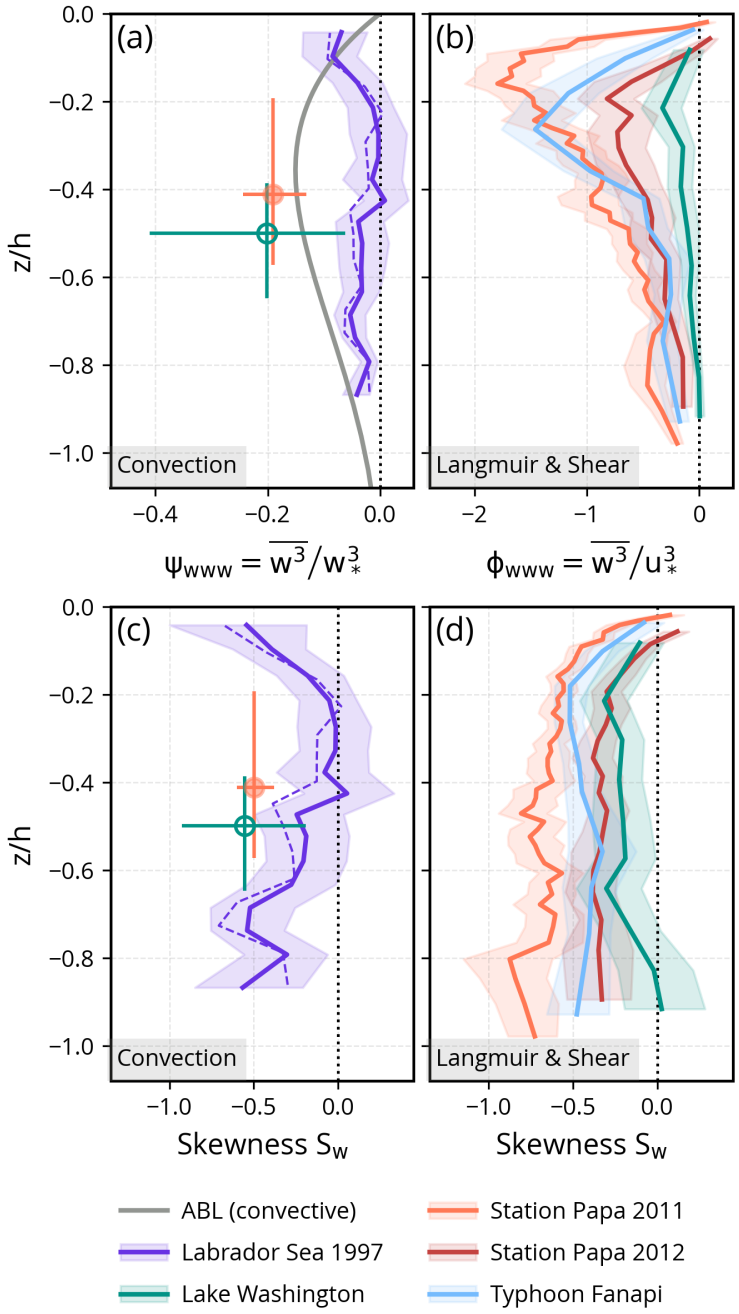

Figure 4.4: Scaling of the profile of (a, b) the third moment and (c, d) the skewness of vertical velocity in the OSBL under (a, c) strongly convective and (b, d) near-neutral conditions. Lagrangian float measurements are averaged in bins of about the same degrees of freedom [5 in (a) and (c); 10 in (b) and (d)], and placed at the median values of z/h. Open circles in (a) and (c) have degrees of freedom less than 5. Color shadings of observations and horizontal error bars show the 95% bootstrap confidence intervals of the mean and vertical error bars show the lower and upper quartiles of z/h. The empirical ABL convective scaling of $\overline{w^3}/w_*^3$ (*Gryanik and Hartmann*, 2002) is shown by the gray solid line in (a).

a maximum in the upper half of the ABL, and sharply declines to zero beyond that point. The bulk magnitude of the Labrador Sea skewness is also smaller than that in the convective ABL (0.3 as opposed to 0.8). Profiles of w skewness in the Langmuir-shear regime share a similar vertical structure that resembles the convective ABL skewness described earlier. Additionally, they generally agree with previous results obtained from LES of the OSBL (*McWilliams et al.*, 1997; *Sullivan et al.*, 2007). These LES studies have shown that simulations incorporating vortex force and stochastic wave breaking consistently yield stronger skewness than those without vortex force. Observations from Lake Washington closely match the skewness profile in the wave-free simulation of *Sullivan et al.* (2007, their Figure 20). The enhancement of skewness, whether caused by the presence of Langmuir turbulence alone or in combination with surface breaking, is evident in the observations as well. Compared to the results of *Sullivan et al.* (2007), observations from the ocean are more in line with LES under developed seas. The LES case with small wave age has a much stronger skewness magnitude throughout. The data collected during the 2011 station Papa experiment have the most pronounced negative skewness, roughly twice that observed in Lake Washington, and comparable to the typical magnitude observed in free convection. This suggests that in terms of the flux of vertical TKE and the asymmetry in top-down and bottom-up diffusion (*Wyngaard*, 1987), a neutral OSBL can be similar to a convective one when surface waves are present. The expected decline of skewness magnitude near the base of the boundary layer is not well resolved by the float measurements, except in Lake Washington. Nonetheless, these data stand as the first-ever measurements of the skewness profile in the OSBL, adding new insights to the existing body of knowledge.

4.4 Summary

In this study, we present a scaling framework for the vertical velocity variance $\overline{w^2}$ in the OSBL. Within this framework, we first propose a generalized scaling of the bulk $\overline{w^2}$ that combines the effect of wind, waves, and surface buoyancy flux in asymptotic limits and

also accounts for the interaction among them. While the current form of the generalized scaling primarily focuses on the reduction of Eulerian shear by convective and Langmuir turbulence, additional interactions can be readily accommodated as our understanding of upper ocean turbulence advances. The proposed bulk scaling (Equation 4.10) is shown to match the bulk $\overline{w^2}$ measured by the Lagrangian floats and those simulated in LES within 15% error. The proposed scaling can be used to construct a regime diagram for the bulk vertical TKE in the OSBL, mapping out the contributions of different forcing mechanisms in the non-dimensional space shown in Figure 4.1c.

Using a set of float measurements, we also examine the depth-dependent scaling of $\overline{w^2}$, $\overline{w^3}$, and w skewness in the convective and the Langmuir-shear regime, respectively. The deep convection data in the convective regime only agree partially with the ABL convective scaling, suggesting a significant role of planetary rotation and a negligible impact from surface waves. Observations in the Langmuir-shear regime exhibit large differences between the lake and the ocean data, as a result of disparate Stokes forcing. In particular, for the first time in observations, we show that the third moment and the skewness of w are substantially enhanced during conditions of strong Stokes forcing. The Langmuir-enhanced profiles of $\overline{w^2}$, $\overline{w^3}$, and w skewness all have a similar vertical structure, in which the depth and the magnitude of the subsurface maximum or minimum are proportional to the penetration depth of the Stokes drift.

Overall, these observational data not only directly support previous LES results, but also serve as the groundwork for future developments of depth-dependent scaling to incorporate the Langmuir effects on $\overline{w^2}$, $\overline{w^3}$, and skewness profiles, which would eventually promote a more complete representation of Langmuir turbulence in upper ocean vertical mixing parameterizations.

Chapter 5
CONCLUSION

5.1 Synthesis

This dissertation highlights the importance of surface wave effects on turbulent kinetic energy, turbulent transport, and vertical mixing of heat in the OSBL.

In particular, scaling results for the temperature gradient and vertical velocity suggest that Langmuir turbulence is the primary driver of the observed deviations, but these observations do not necessarily exclude the potential contribution from wave breaking. Results from Chapters 2 to 4 are consistent with each other, even though the physical variables investigated and the observing platforms and instruments involved are distinctly different. Together, they reinforce the statement that the conventional ABL scaling relations do not apply in the OSBL, as they neglect the intricate variations of turbulence caused by surface wave forcing.

In addition to the examination of conventional ABL scaling relations, this study also develops new approaches to incorporate the Langmuir turbulence effect in the scaling of vertical velocity variance. For the surface layer scaling, a new scaling parameter representing the local ratio of Stokes shear production to neutral Eulerian shear production, along with a surface proximity function representing the non-local terms are introduced. These two parameters are shown to give a more effective scaling of the Langmuir effect than either form of the Langmuir number. For the scaling of the boundary layer averaged vertical velocity variance, the various asymptotic scaling behaviors under a single forcing mechanism are combined to give a generalized expression. The generalized scaling agrees well with Lagrangian float measurements and LES results, except in deep convection, where the asymptotic convective scaling appears to be modulated by the

effects of planetary rotation and thermobaricity.

5.2 *Implications*

This dissertation shows that the conventional ABL scaling relations underestimate the vertical mixing in the OSBL. Boundary layer schemes that rely on turbulence scaling relations (e.g., KPP) should, at least, be updated to adopt new scaling relations that explicitly represent Langmuir turbulence.

For the turbulent velocity scale in KPP, two distinct pathways for improvement are possible. First, we can keep the existing KPP formulation but have to replace the surface layer scaling relations of temperature gradient and shear with a new set that includes the Langmuir effect. Note that this approach only raises the magnitude of the velocity scale on the basis of the smaller mean gradients in the surface layer. Recent LES-based work by *Large et al.* (2019) is a pioneering effort in advancing KPP along this pathway. However, due to the sensitivity of the LES near-surface results to the subgrid-scale model, the extent to which their new parameterization aligns with observations remains uncertain. Second, given that Langmuir turbulence modifies both the velocity magnitude and the length scale, we can propose an entirely new formulation based on a generalized expression for the depth-dependent scaling of $\overline{w^2}$. Such a scaling relation is not available at this moment, but the results of Chapters 3 to 4 have provided some guidance for future developments. An additional challenge associated with this pathway is determining the appropriate differentiation of the velocity scale for the eddy diffusivity of heat and momentum. Exploring the variation of the turbulent Prandtl number in the Langmuir turbulence regime (*Large et al.*, 2019) could provide valuable insights to address this challenge.

Furthermore, the results of $\overline{w^3}$ and w-skewness profiles in Chapter 4 also encourage a scaling relation for the turbulent transport of vertical TKE, which is significant in the presence of Langmuir turbulence. This scaling will benefit the future development of Second-Moment Closure (*Harcourt*, 2013, 2015) to include non-local effects in the algebraic

Reynolds stress model.

Last, these results all contribute to the efforts of developing a comprehensive scaling of the surface-driven turbulence in the OSBL. This is not only valuable in guiding the advancement of boundary layer parameterizations, but also helps us to identify regions and times where the lateral inhomogeneity and the non-equilibrium effects are important.

5.3 *Outlook*

This dissertation expands our knowledge of turbulence scaling in the OSBL, but also points out a variety of unresolved questions.

First, Chapter 2 only considers the surface layer scaling in conditions of destabilizing surface buoyancy flux. Similarly, in Chapter 3 and Chapter 4, the results of the vertical velocity scaling do not extend to scenarios with strong stabilizing surface buoyancy flux. It is expected that, with surface heating and Langmuir turbulence, the temperature gradients would also be smaller than the Monin-Obukhov scaling (*Kukulka et al.*, 2013; *Pearson et al.*, 2015), and the Stokes shear production would compete against the suppressing buoyancy flux to raise the turbulence intensity and maintain an otherwise shallower boundary layer. With an appropriately defined Obukhov length that accounts for penetrative solar heating, future research should focus on the stable side and the development of scaling relations to quantify these deviations from the Monin-Obukhov scaling and other conventional ABL scaling.

Second, the analysis in Chapter 2 also leads to questions about the surface layer scaling of the vertical Eulerian shear $\partial\overline{u}/\partial z$. LES studies have demonstrated a significant reduction (up to 80%) of Eulerian shear in Langmuir turbulence. Due to the contamination of much larger surface wave orbital velocity and other complications, detailed observations of near-surface shear have been difficult. With the emergence of new observing techniques, future research on this topic should examine its various quantitative scaling relations, including those neglecting surface waves (*Businger et al.*, 1971), and those explicitly accounting for surface waves (*Large et al.*, 2019).

BIBLIOGRAPHY

Agrawal, Y. C., E. A. Terray, M. A. Donelan, P. A. Hwang, A. J. Williams, W. M. Drennan, K. K. Kahma, and S. A. Krtaigorodskii, Enhanced dissipation of kinetic energy beneath surface waves, *Nature*, *359*(6392), 219–220, doi:10.1038/359219a0, 1992.

Allouche, M., E. Bou-Zeid, C. Ansorge, G. G. Katul, M. Chamecki, O. Acevedo, S. Thanekar, and J. D. Fuentes, The Detection, Genesis, and Modeling of Turbulence Intermittency in the Stable Atmospheric Surface Layer, *J. Atmos. Sci.*, *79*(4), 1171–1190, doi:10.1175/JAS-D-21-0053.1, 2022.

Anderson, N., J. Keene, and M. Cronin, Data Acquisition and Processing Report for OCS Mooring PA008, *Noaa data rep.*, NOAA/Pacific Marine Environmental Laboratory, Seattle, WA, https://www.pmel.noaa.gov/ocs/sites/default/files/atoms/files/OCS_DAPR_PA008_FINAL.pdf, 2018.

Andrén, A., and C.-H. Moeng, Single-Point Closures in a Neutrally Stratified Boundary Layer, *J. Atmos. Sci.*, *50*(20), 3366–3379, doi:10.1175/1520-0469(1993)050<3366:SPCIAN>2.0.CO;2, 1993.

Belcher, S. E., et al., A global perspective on Langmuir turbulence in the ocean surface boundary layer, *Geophys. Res. Lett.*, *39*(18), doi:10.1029/2012GL052932, 2012.

Black, P. G., E. A. D'Asaro, W. M. Drennan, J. R. French, P. P. Niiler, T. B. Sanford, E. J. Terrill, E. J. Walsh, and J. A. Zhang, Air-sea exchange in hurricanes: Synthesis of observations from the coupled boundary layer air-sea transfer experiment, *Bull. Am. Meteorol. Soc.*, *88*(3), 357–374, doi:10.1175/BAMS-88-3-357, 2007.

Bouchard, P., and J. Farrar, Preliminary techniques for measuring waves on UOP buoys, *Technical note of the whoi upper ocean processes group*, Woods Hole Oceanographic Institution, Woods Hole, MA, http://uop.whoi.edu/techdocs/technote/TN-Feb08-WAMDAS.pdf, 2008.

Breivik, Ø., P. A. Janssen, and J. R. Bidlot, Approximate stokes drift profiles in deep water, *J. Phys. Oceanogr.*, *44*(9), 2433–2445, doi:10.1175/JPO-D-14-0020.1, 2014.

Buckingham, E., On physically similar systems; illustrations of the use of dimensional equations, *Phys. Rev.*, *4*, 345–376, 1914.

Burchard, H., Simulating the Wave-Enhanced Layer under Breaking Surface Waves with Two-Equation Turbulence Models, *J. Phys. Oceanogr.*, *31*(11), 3133–3145, doi:10.1175/1520-0485(2001)031<3133:STWELU>2.0.CO;2, 2001.

Burchard, H., O. Petersen, and T. P. Rippeth, Comparing the performance of the Mellor-Yamada and the k-ϵ two equation turbulence models, *J. Geophys. Res. Ocean.*, *103*(C5), 10,543–10,554, doi:10.1029/98jc00261, 1998.

Businger, J., J. Wyngaard, Y. Izumi, and E. Bradley, Flux- profile relationships in the atmospheric surface layer, *J. Atmos. Sci.*, *28*(2), 181–189, doi:10.1175/1520-0469(1971)028<0181:fprita>2.0.co;2, 1971.

Businger, J. A., A note on free convection, *Boundary-Layer Meteorol.*, *4*(1), 323–326, doi:10.1007/BF02265241, 1973.

Carniel, S., M. Sclavo, L. H. Kantha, and C. A. Clayson, Langmuir cells and mixing in the upper ocean, *Nuovo Cimento C*, *28*(1), 33–54, doi:10.1393/ncc/i2005-10022-8, 2005.

Carniel, S., L. H. Kantha, J. W. Book, M. Sclavo, and H. Prandke, Turbulence variability in the upper layers of the Southern Adriatic Sea under a variety of atmospheric forcing conditions, *Cont. Shelf Res.*, *44*, 39–56, doi:https://doi.org/10.1016/j.csr.2011.01.003, 2012.

Cheng, Y., V. M. Canuto, and A. M. Howard, An improved model for the turbulent PBL, *J. Atmos. Sci.*, *59*(9), 1550–1565, doi:10.1175/1520-0469(2002)059<1550:AIMFTT>2.0.CO;2, 2002.

Craig, P. D., Velocity profiles and surface roughness under breaking waves, *J. Geophys. Res. Ocean.*, *101*(C1), 1265–1277, doi:10.1029/95JC03220, 1996.

Craig, P. D., and M. L. Banner, Modeling Wave-Enhanced Turbulence in the Ocean Surface Layer, *J. Phys. Oceanogr.*, *24*(12), 2546–2559, doi:10.1175/1520-0485(1994)024<2546:MWETIT>2.0.CO;2, 1994.

Craik, A. D., and S. Leibovich, A rational model for Langmuir circulations, *J. Fluid Mech.*, *73*(3), 401–426, doi:10.1017/S0022112076001420, 1976.

Cronin, M. F., OCS Papa mooring in-situ hourly data, accessed 28 November 2019, `https://www.pmel.noaa.gov/ocs/data/disdel/` and `https://www.pmel.noaa.gov/ocs/data/fluxdisdel/`, 2007, updated daily.

Crow, S., Turbulent Rayleigh shear flow, *J. Fluid Mech.*, *32*(1), 113–130, doi:10.1017/S0022112068000613, 1968.

D'Alessio, S. J. D., K. Abdella, and N. A. Mcfarlane, A New Second-Order Turbulence Closure Scheme for Modeling the Oceanic Mixed Layer, *J. Phys. Oceanogr.*, *28*(8), 1624–1641, doi:10.1175/1520-0485(1998)028<1624:ANSOTC>2.0.CO;2, 1998.

D'Asaro, E., Surface wave measurements from subsurface floats, *J. Atmos. Ocean. Technol.*, *32*(4), 816–827, doi:10.1175/JTECH-D-14-00180.1, 2015.

D'Asaro, E. A., The Energy Flux from the Wind to Near-Inertial Motions in the Surface Mixed Layer, *J. Phys. Oceanogr.*, *15*(8), 1043–1059, doi:10.1175/1520-0485(1985)015<1043:TEFFTW>2.0.CO;2, 1985.

D'Asaro, E. A., Turbulent Vertical Kinetic Energy in the Ocean Mixed Layer, *J. Phys. Oceanogr.*, *31*(12), 3530–3537, doi:10.1175/1520-0485(2002)031<3530:TVKEIT>2.0.CO;2, 2001.

D'Asaro, E. A., Performance of Autonomous Lagrangian Floats, *J. Atmos. Ocean. Technol.*, *20*(6), 896–911, doi:10.1175/1520-0426(2003)020<0896:POALF>2.0.CO;2, 2003a.

D'Asaro, E. A., The Ocean Boundary Layer below Hurricane Dennis, *J. Phys. Oceanogr.*, *33*(3), 561–579, doi:10.1175/1520-0485(2003)033<0561:TOBLBH>2.0.CO;2, 2003b.

D'Asaro, E. A., Air–Sea Heat Flux Measurements from Nearly Neutrally Buoyant Floats, *J. Atmos. Ocean. Technol.*, *21*(7), 1086–1094, doi:10.1175/1520-0426(2004)021<1086:AHFMFN>2.0.CO;2, 2004.

D'Asaro, E. A., USAF-C130 Lagrangian Float Data, accessed 01 Jul 2023, https://doi.org/10.26023/1N5N-TM39-0T0A, 2012.

D'Asaro, E. A., Turbulence in the Upper-Ocean Mixed Layer, *Ann. Rev. Mar. Sci.*, *6*(1), 101–115, doi:10.1146/annurev-marine-010213-135138, 2014.

D'Asaro, E. A., D. M. Farmer, J. T. Osse, and G. T. Dairiki, A Lagrangian Float, *J. Atmos. Ocean. Technol.*, *13*(6), 1230–1246, doi:10.1175/1520-0426(1996)013<1230:ALF>2.0.CO;2, 1996.

D'Asaro, E. A., J. Thomson, A. Y. Shcherbina, R. R. Harcourt, M. F. Cronin, M. A. Hemer, and B. Fox-Kemper, Quantifying upper ocean turbulence driven by surface waves, *Geophys. Res. Lett.*, *41*(1), 102–107, doi:10.1002/2013GL058193, 2014a.

D'Asaro, E. A., et al., Impact of typhoons on the ocean in the pacific, *Bull. Am. Meteorol. Soc.*, *95*(9), 1405–1418, doi:10.1175/BAMS-D-12-00104.1, 2014b.

de Boyer Montégut, C., G. Madec, A. S. Fischer, A. Lazar, and D. Iudicone, Mixed layer depth over the global ocean: An examination of profile data and a profile-based climatology, *J. Geophys. Res. Ocean.*, *109*(12), 1–20, doi:10.1029/2004JC002378, 2004.

Deardorff, J. W., Convective Velocity and Temperature Scales for the Unstable Planetary Boundary Layer and for Rayleigh Convection, *J. Atmos. Sci.*, *27*(8), 1211–1213, doi:10.1175/1520-0469(1970)027<1211:CVATSF>2.0.CO;2, 1970.

Dijkstra, H. A., and G. Burgers, Fluid dynamics of El Niño variability, *Annu. Rev. Fluid Mech.*, *34*(1), 531–558, doi:10.1146/annurev.fluid.34.090501.144936, 2002.

Domaradzki, J. A., and R. W. Metcalfe, Direct numerical simulations of the effects of shear on turbulent Rayleigh-Bénard convection, *J. Fluid Mech.*, *193*(-1), 499, doi:10.1017/S002211208800223X, 1988.

Drennan, W. M., K. K. Kahma, E. A. Terray, M. A. Donelan, and S. A. Kitaigorodskii, Observations of the Enhancement of Kinetic Energy Dissipation Beneath Breaking Wind Waves, in *Breaking Waves*, edited by M. L. Banner and R. H. J. Grimshaw, pp. 95–101, Springer Berlin Heidelberg, Berlin, Heidelberg, 1992.

Drennan, W. M., M. A. Donelan, E. A. Terray, and K. B. Katsaros, Oceanic Turbulence Dissipation Measurements in SWADE, *J. Phys. Oceanogr.*, *26*(5), 808–815, doi:10.1175/1520-0485(1996)026<0808:OTDMIS>2.0.CO;2, 1996.

Duncan, J. H., An experimental investigation of breaking waves produced by a towed hydrofoil, *Proc. R. Soc. London. A. Math. Phys. Sci.*, *377*(1770), 331–348, doi:10.1098/rspa.1981.0127, 1981.

Edson, J. B., C. J. Zappa, J. A. Ware, W. R. McGillis, and J. E. Hare, Scalar flux profile relationships over the open ocean, *J. Geophys. Res. Ocean.*, *109*(C8), doi:10.1029/2003JC001960, 2004.

Emanuel, K., Tropical Cyclones, *Annu. Rev. Earth Planet. Sci.*, *31*(1), 75–104, doi:10.1146/annurev.earth.31.100901.141259, 2003.

Fairall, C. W., E. F. Bradley, D. P. Rogers, J. B. Edson, and G. S. Young, Bulk parameterization of air-sea fluxes for tropical oceanglobal atmosphere coupled-ocean atmosphere response experiment, *J. Geophys. Res. Ocean.*, *101*(C2), 3747–3764, doi:10.1029/95JC03205, 1996.

Fairall, C. W., E. F. Bradley, J. E. Hare, A. A. Grachev, and J. B. Edson, Bulk Parameterization of Air-Sea Fluxes: Updates and Verification for the COARE Algorithm, *J. Clim.*, *16*(4), 571–591, doi:10.1175/1520-0442(2003)016<0571:BPOASF>2.0.CO;2, 2003.

Farrar, J. T., WHOI mooring CTD, surface flux and meteorological data for the SPURS-1 N. Atlantic field campaign, version 1, accessed 18 June 2019, https://doi.org/10.5067/SPUR1-MOOR1, 2015.

Farrar, J. T., et al., Salinity and Temperature Balances at the SPURS Central Mooring During Fall and Winter, *Oceanography*, *28*(1), 56–65, 2015.

Feddersen, F., J. H. Trowbridge, and A. J. Williams, Vertical Structure of Dissipation in the Nearshore, *J. Phys. Oceanogr.*, *37*(7), 1764–1777, doi:10.1175/JPO3098.1, 2007.

Ferrari, R., and C. Wunsch, Ocean circulation kinetic energy: Reservoirs, sources, and sinks, *Annual Review of Fluid Mechanics*, *41*(1), 253–282, doi:10.1146/annurev.fluid.40.111406.102139, 2009.

Foken, T., 50 years of the Monin-Obukhov similarity theory, *Boundary-Layer Meteorol.*, *119*(3), 431–447, doi:10.1007/s10546-006-9048-6, 2006.

Fox-Kemper, B., L. Johnson, and F. Qiao, Chapter 4 - ocean near-surface layers, in *Ocean Mixing*, edited by M. Meredith and A. Garabato, pp. 65–94, Elsevier, doi:10.1016/B978-0-12-821512-8.00011-6, 2022.

Garanaik, A., F. Pereira, K. Smith, R. Robey, Q. Li, B. Pearson, and L. V. Roekel, A new hybrid mass-flux/ high-order turbulence closure for ocean vertical mixing, 2022.

Gargett, A. E., and C. E. Grosch, Turbulence Process Domination under the Combined Forcings of Wind Stress, the Langmuir Vortex Force, and Surface Cooling, *J. Phys. Oceanogr.*, *44*(1), 44–67, doi:10.1175/JPO-D-13-021.1, 2014.

Gargett, A. E., and J. R. Wells, Langmuir turbulence in shallow water. Part 1. Observations, *J. Fluid Mech.*, *576*, 27–61, doi:10.1017/S0022112006004575, 2007.

Garratt, J., *The Atmospheric Boundary Layer*, Cambridge Atmospheric and Space Science Series, 316 pp., Cambridge University Press, 1992.

Garwood, R. W., S. M. Isakari, and P. C. Gallacher, Thermobaric Convection, pp. 199–209, doi:10.1029/gm085p0199, 1994.

Gerbi, G. P., J. H. Trowbridge, J. B. Edson, A. J. Plueddemann, E. A. Terray, and J. J. Fredericks, Measurements of momentum and heat transfer across the air-sea interface, *J. Phys. Oceanogr.*, *38*(5), 1054–1072, doi:10.1175/2007JPO3739.1, 2008.

Gerbi, G. P., J. H. Trowbridge, E. A. Terray, A. J. Plueddemann, and T. Kukulka, Observations of Turbulence in the Ocean Surface Boundary Layer: Energetics and Transport, *J. Phys. Oceanogr.*, *39*(5), 1077–1096, doi:10.1175/2008JPO4044.1, 2009.

Giordani, H., R. Bourdallé-Badie, and G. Madec, An Eddy-Diffusivity Mass-Flux Parameterization for Modeling Oceanic Convection, *J. Adv. Model. Earth Syst.*, *12*(9), doi:10.1029/2020MS002078, 2020.

Grachev, A. A., E. L. Andreas, C. W. Fairall, P. S. Guest, and P. O. G. Persson, The Critical Richardson Number and Limits of Applicability of Local Similarity Theory in the Stable Boundary Layer, *Boundary-Layer Meteorol.*, *147*(1), 51–82, doi:10.1007/s10546-012-9771-0, 2013.

Grachev, A. A., E. L. Andreas, C. W. Fairall, P. S. Guest, and P. O. G. Persson, Similarity theory based on the Dougherty-Ozmidov length scale, *Q. J. R. Meteorol. Soc.*, *141*(690), 1845–1856, doi:10.1002/qj.2488, 2015.

Grant, A. L., and S. E. Belcher, Characteristics of Langmuir turbulence in the ocean mixed layer, *J. Phys. Oceanogr.*, *39*(8), 1871–1887, doi:10.1175/2009JPO4119.1, 2009.

Griffies, S. M., M. Levy, A. J. Adcroft, G. Danabasoglu, R. W. Hallberg, D. Jacobsen, W. Large, and T. Ringler, Theory and numerics of the Community Ocean Vertical Mixing (CVMix) project, *Tech. rep.*, 2015.

Gryanik, V. M., and J. Hartmann, A turbulence closure for the convective boundary layer based on a two-scale mass-flux approach, *J. Atmos. Sci.*, *59*(18), 2729–2744, doi:10.1175/1520-0469(2002)059<2729:ATCFTC>2.0.CO;2, 2002.

Harcourt, R. R., A second-moment closure model of Langmuir turbulence, *J. Phys. Oceanogr.*, *43*(4), 673–697, doi:10.1175/JPO-D-12-0105.1, 2013.

Harcourt, R. R., An improved second-moment closure model of Langmuir turbulence, *J. Phys. Oceanogr.*, *45*(1), 84–103, doi:10.1175/JPO-D-14-0046.1, 2015.

Harcourt, R. R., and E. A. D'Asaro, Large-eddy simulation of Langmuir turbulence in pure wind seas, *J. Phys. Oceanogr.*, *38*(7), 1542–1562, doi:10.1175/2007JPO3842.1, 2008.

Harcourt, R. R., and E. A. D'Asaro, Measurement of vertical kinetic energy and vertical velocity skewness in oceanic boundary layers by imperfectly lagrangian floats, *J. Atmos. Ocean. Technol.*, *27*(11), 1918–1935, doi:10.1175/2010JTECHO731.1, 2010.

Hersbach, H., et al., The ERA5 global reanalysis, *Q. J. R. Meteorol. Soc.*, *146*(730), 1999–2049, doi:10.1002/QJ.3803, 2020.

Högström, U., Review of some basic characteristics of the atmospheric surface layer, *Boundary-Layer Meteorol.*, *78*(3-4), 215–246, doi:10.1007/BF00120937, 1996.

Hsu, J. Y., R. C. Lien, E. A. D'Asaro, and T. B. Sanford, Estimates of surface wind stress and drag coefficients in Typhoon Megi, *J. Phys. Oceanogr.*, *47*(3), 545–565, doi:10.1175/JPO-D-16-0069.1, 2017.

Hsu, J. Y., R. C. Lien, E. A. D'Asaro, and T. B. Sanford, Scaling of Drag Coefficients Under Five Tropical Cyclones, *Geophys. Res. Lett.*, *46*(6), 3349–3358, doi:10.1029/2018GL081574, 2019.

Jerlov, N., *Marine Optics*, *Elsevier Oceanography Series*, vol. 14, 230 pp., Elsevier Scientific Publishing Company, 1976.

Kantha, L., H. U. Lass, and H. Prandke, A note on Stokes production of turbulence kinetic energy in the oceanic mixed layer: Observations in the Baltic Sea, *Ocean Dyn.*, *60*(1), 171–180, doi:10.1007/s10236-009-0257-7, 2010.

Kantha, L. H., and C. A. Clayson, An improved mixed layer model for geophysical applications, *J. Geophys. Res. Ocean.*, *99*(C12), 25,235, doi:10.1029/94JC02257, 1994.

Kantha, L. H., and C. A. Clayson, On the effect of surface gravity waves on mixing in the oceanic mixed layer, *Ocean Model.*, *6*(2), 101–124, doi:10.1016/S1463-5003(02)00062-8, 2004.

Kenyon, K. E., Stokes drift for random gravity waves, *J. Geophys. Res.*, *74*(28), 6991–6994, doi:10.1029/JC074i028p06991, 1969.

Kierzenka, J., and L. F. Shampine, A BVP Solver Based on Residual Control and the MATLAB PSE, *ACM Trans. Math. Softw.*, *27*(3), 299–316, doi:10.1145/502800.502801, 2001.

Kolmogorov, A., The Local Structure of Turbulence in Incompressible Viscous Fluid for Very Large Reynolds Numbers, *Dokl. Akad. Nauk SSSR*, *30*, 301–305, 1941.

Kukulka, T., and R. R. Harcourt, Influence of stokes drift decay scale on langmuir turbulence, *J. Phys. Oceanogr.*, *47*(7), 1637–1656, doi:10.1175/JPO-D-16-0244.1, 2017.

Kukulka, T., A. J. Plueddemann, J. H. Trowbridge, and P. P. Sullivan, Rapid mixed layer deepening by the combination of langmuir and shear instabilities: A case study, *J. Phys. Oceanogr.*, *40*(11), 2381–2400, doi:10.1175/2010JPO4403.1, 2010.

Kukulka, T., A. J. Plueddemann, and P. P. Sullivan, Nonlocal transport due to Langmuir circulation in a coastal ocean, *J. Geophys. Res. Ocean.*, *117*(C12), doi:10.1029/2012JC008340, 2012.

Kukulka, T., A. J. Plueddemann, and P. P. Sullivan, Inhibited upper ocean restratification in nonequilibrium swell conditions, *Geophys. Res. Lett.*, *40*(14), 3672–3676, doi:10.1002/grl.50708, 2013.

Langmuir, I., Surface motion of water induced by wind, *Science*, *87*(2250), 119–123, doi:10.1126/science.87.2250.119, 1938.

Large, W. G., J. C. McWilliams, and S. C. Doney, Oceanic vertical mixing: A review and a model with a nonlocal boundary layer parameterization, *Rev. Geophys.*, *32*(4), 363–403, doi:10.1029/94RG01872, 1994.

Large, W. G., E. G. Patton, A. K. Duvivier, P. P. Sullivan, and L. Romero, Similarity theory in the surface layer of large-eddy simulations of the wind-, wave-, and buoyancy-forced southern ocean, *J. Phys. Oceanogr.*, *49*(8), 2165–2187, doi:10.1175/JPO-D-18-0066.1, 2019.

Launder, B. E., On the effects of a gravitational field on the turbulent transport of heat and momentum, *J. Fluid Mech.*, *67*(3), 569–581, doi:10.1017/S002211207500047X, 1975.

LeMone, M. A., et al., 100 Years of Progress in Boundary Layer Meteorology, *Meteorol. Monogr.*, *59*, 9.1–9.85, doi:10.1175/amsmonographs-d-18-0013.1, 2019.

Lenain, L., and N. Pizzo, The contribution of high-frequency wind-generated surface waves to the stokes drift, *J. Phys. Oceanogr.*, *50*(12), 3455–3465, doi:10.1175/JPO-D-20-0116.1, 2020.

Lenschow, D. H., J. C. Wyngaard, and W. T. Pennell, Mean-Field and Second-Moment Budgets in a Baroclinic, Convective Boundary Layer, *J. Atmos. Sci.*, *37*(6), 1313–1326, doi:10.1175/1520-0469(1980)037<1313:MFASMB>2.0.CO;2, 1980.

Lenschow, D. H., J. Mann, and L. Kristensen, How Long Is Long Enough When Measuring Fluxes and Other Turbulence Statistics?, *J. Atmos. Ocean. Technol.*, *11*(3), 661–673, doi:10.1175/1520-0426(1994)011<0661:HLILEW>2.0.CO;2, 1994.

Lenschow, D. H., M. Lothon, S. D. Mayor, P. P. Sullivan, and G. Canut, A Comparison of Higher-Order Vertical Velocity Moments in the Convective Boundary Layer from Lidar with In Situ Measurements and Large-Eddy Simulation, *Boundary-Layer Meteorol.*, *143*(1), 107–123, doi:10.1007/s10546-011-9615-3, 2012.

Li, M., C. Garrett, and E. Skyllingstad, A regime diagram for classifying turbulent large eddies in the upper ocean, *Deep Sea Res. Part I Oceanogr. Res. Pap.*, *52*(2), 259–278, doi:10.1016/J.DSR.2004.09.004, 2005.

Li, Q., and B. Fox-Kemper, Assessing the effects of Langmuir turbulence on the entrainment buoyancy flux in the ocean surface boundary layer, *J. Phys. Oceanogr.*, *47*(12), 2863–2886, doi:10.1175/JPO-D-17-0085.1, 2017.

Li, Q., A. Webb, B. Fox-Kemper, A. Craig, G. Danabasoglu, W. G. Large, and M. Vertenstein, Langmuir mixing effects on global climate: WAVEWATCH III in CESM, *Ocean Model.*, *103*, 145–160, doi:10.1016/j.ocemod.2015.07.020, 2016.

Li, Q., et al., Comparing Ocean Surface Boundary Vertical Mixing Schemes Including Langmuir Turbulence, *J. Adv. Model. Earth Syst.*, *11*(11), 3545–3592, doi:10.1029/2019MS001810, 2019.

Lien, R. C., E. A. D'Asaro, and G. T. Dairiki, Lagrangian frequency spectra of vertical velocity and vorticity in high-Reynolds-number oceanic turbulence, *J. Fluid Mech.*, *362*, 177–198, doi:10.1017/S0022112098008787, 1998.

Lin, I. I., et al., An ocean coupling potential intensity index for tropical cyclones, *Geophys. Res. Lett.*, *40*(9), 1878–1882, doi:10.1002/grl.50091, 2013.

Lindstrom, E., F. Bryan, and R. Schmitt, SPURS: Salinity Processes in the Upper-ocean Regional Study — The North Atlantic Experiment, *Oceanography*, *28*(1), 14–19, doi:10.5670/oceanog.2015.01, 2015.

Lombardo, C. P., and M. C. Gregg, Similarity scaling of viscous and thermal dissipation in a convecting surface boundary layer, *J. Geophys. Res.*, *94*(C5), 6273, doi:10.1029/jc094ic05p06273, 1989.

Mahrt, L., Stably Stratified Atmospheric Boundary Layers, *Annu. Rev. Fluid Mech.*, *46*(1), 23–45, doi:10.1146/annurev-fluid-010313-141354, 2014.

Maronga, B., and J. Reuder, On the formulation and universality of monin–obukhov similarity functions for mean gradients and standard deviations in the unstable surface layer: Results from surface-layer-resolving large-eddy simulations, *Journal of the Atmospheric Sciences*, *74*(4), 989 – 1010, doi:10.1175/JAS-D-16-0186.1, 2017.

Marshall, J., et al., The Labrador Sea Deep Convection Experiment, *Bull. Am. Meteorol. Soc.*, *79*(10), 2033–2058, doi:10.1175/1520-0477(1998)079<2033:tlsdce>2.0.co;2, 1998.

Maxworthy, T., Convection into domains with open boundaries, *Annu. Rev. Fluid Mech.*, *29*, 327–371, doi:10.1146/annurev.fluid.29.1.327, 1997.

McWilliams, J. C., and P. P. Sullivan, Vertical Mixing by Langmuir Circulations, *Spill Sci. Technol. Bull.*, *6*(3-4), 225–237, doi:10.1016/S1353-2561(01)00041-X, 2000.

McWilliams, J. C., P. P. Sullivan, and C.-H. Moeng, Langmuir turbulence in the ocean, *J. Fluid Mech.*, *334*, 1–30, doi:10.1017/S0022112096004375, 1997.

McWilliams, J. C., E. Huckle, J. H. Liang, and P. P. Sullivan, The wavy ekman layer: Langmuir circulations, breaking waves, and reynolds stress, *J. Phys. Oceanogr.*, *42*(11), 1793–1816, doi:10.1175/JPO-D-12-07.1, 2012.

Mellor, G. L., Analytic Prediction of the Properties of Stratified Planetary Surface Layers, *J. Atmos. Sci.*, *30*(6), 1061–1069, doi:10.1175/1520-0469(1973)030<1061:apotpo>2.0.co;2, 1973.

Mellor, G. L., and T. Yamada, Development of a turbulence closure model for geophysical fluid problems, doi:10.1029/RG020i004p00851, 1982.

Mironov, D. V., V. M. Gryanik, C. H. Moeng, D. J. Olbers, and T. H. Warncke, Vertical turbulence structure and second-moment budgets in convection with rotation: A large-eddy simulation study, *Q. J. R. Meteorol. Soc.*, *126*(563), 477–515, doi:10.1002/qj.49712656306, 2000.

Moeng, C.-H., and J. C. Wyngaard, An Analysis of Closures for Pressure-Scalar Covariances in the Convective Boundary Layer, *J. Atmos. Sci.*, *43*(21), 2499–2513, doi:10.1175/1520-0469(1986)043<2499:AAOCFP>2.0.CO;2, 1986.

Monin, A., and A. Yaglom, *Statistical Fluid Mechanics: Mechanics of Turbulence*, vol. 1, 769 pp., MIT Press, 1971.

Monin, A. S., and A. M. Obukhov, Basic laws of turbulent mixing in the surface layer of the atmosphere, *Contrib. Geophys. Inst. Acad. Sci. USSR*, *24*(151), 163–187, 1954.

Nieuwstadt, F. T. M., The Turbulent Structure of the Stable, Nocturnal Boundary Layer, *J. Atmos. Sci.*, *41*(14), 2202–2216, doi:10.1175/1520-0469(1984)041<2202:TTSOTS>2.0.CO;2, 1984.

Obukhov, A. M., Turbulence in thermally inhomogeneous atmosphere, *Tr. Inst. Teoret. Geofiz. Akad. Nauk SSSR*, *1*, 95–115, 1946.

Panofsky, H. A., Determination of stress from wind and temperature measurements, *Q. J. R. Meteorol. Soc.*, *89*(379), 85–94, doi:10.1002/qj.49708937906, 1963.

Panofsky, H. A., H. Tennekes, D. H. Lenschow, and J. C. Wyngaard, The characteristics of turbulent velocity components in the surface layer under convective conditions, *Boundary-Layer Meteorol.*, *11*(3), 355–361, doi:10.1007/BF02186086, 1977.

Paulson, C. A., and J. J. Simpson, Irradiance Measurements in the Upper Ocean, *J. Phys. Oceanogr.*, *7*(6), 952–956, doi:10.1175/1520-0485(1977)007<0952:IMITUO>2.0.CO;2, 1977.

Pearson, B. C., A. L. Grant, J. A. Polton, and S. E. Belcher, Langmuir turbulence and surface heating in the ocean surface boundary layer, *J. Phys. Oceanogr.*, *45*(12), 2897–2911, doi:10.1175/JPO-D-15-0018.1, 2015.

Pearson, B. C., A. L. Grant, and J. A. Polton, Pressure-strain terms in Langmuir turbulence, *J. Fluid Mech.*, *880*, 5–31, doi:10.1017/jfm.2019.701, 2019.

Polton, J. A., and S. E. Belcher, Langmuir turbulence and deeply penetrating jets in an unstratified mixed layer, *J. Geophys. Res. Ocean.*, *112*(9), 9020, doi:10.1029/2007JC004205, 2007.

Powell, M. J. D., A FORTRAN Subroutine for Solving Systems of Nonlinear Algebraic Equations, in *Numerical Methods for Nonlinear Algebraic Equations*, edited by P. Rabinowitz, pp. 115–162, Gordon and Breach Science Publishers, 1970.

Prandtl, L., Bericht über Untersuchungen zur ausgebildeten Turbulenz, *Z. Angew. Math. Mech.*, *5*(2), 136–139, doi:10.1002/zamm.19250050212, 1925.

Reichl, B. G., and R. Hallberg, A simplified energetics based planetary boundary layer (ePBL) approach for ocean climate simulations., *Ocean Model.*, *132*, 112–129, doi:10.1016/j.ocemod.2018.10.004, 2018.

Reichl, B. G., D. Wang, T. Hara, I. Ginis, and T. Kukulka, Langmuir Turbulence Parameterization in Tropical Cyclone Conditions, *J. Phys. Oceanogr.*, *46*(3), 863–886, doi:10.1175/JPO-D-15-0106.1, 2016.

Renfrew, I. A., et al., An evaluation of surface meteorology and fluxes over the Iceland and Greenland Seas in ERA5 reanalysis: The impact of sea ice distribution, *Q. J. R. Meteorol. Soc.*, *147*(734), 691–712, doi:10.1002/qj.3941, 2021.

Rodi, W., Examples of calculation methods for flow and mixing in stratified fluids, *J. Geophys. Res. Ocean.*, *92*(C5), 5305–5328, doi:10.1029/JC092iC05p05305, 1987.

Rotta, J., Statistische Theorie nichthomogener Turbulenz, *Zeitschrift für Phys.*, *129*(6), 547–572, doi:10.1007/BF01330059, 1951.

Sallée, J. B., E. Shuckburgh, N. Bruneau, A. J. Meijers, T. J. Bracegirdle, and Z. Wang, Assessment of Southern Ocean mixed-layer depths in CMIP5 models: Historical bias and forcing response, *J. Geophys. Res. Ocean.*, *118*(4), 1845–1862, doi:10.1002/jgrc.20157, 2013.

Sanford, T. B., J. F. Price, and J. B. Girton, Upper-ocean response to hurricane frances (2004) observed by profiling EM-APEX floats, *J. Phys. Oceanogr.*, *41*(6), 1041–1056, doi:10.1175/2010JPO4313.1, 2011.

Shay, T. J., and M. C. Gregg, Convectively Driven Turbulent Mixing in the Upper Ocean, *J. Phys. Oceanogr.*, *16*(11), 1777–1798, doi:10.1175/1520-0485(1986)016<1777:CDTMIT>2.0.CO;2, 1986.

Simonot, J.-Y., and H. Le Treut, A climatological field of mean optical properties of the world ocean, *J. Geophys. Res. Ocean.*, *91*(C5), 6642, doi:10.1029/jc091ic05p06642, 1986.

Sinha, N., A. E. Tejada-Martínez, C. Akan, and C. E. Grosch, Toward a K-Profile Parameterization of Langmuir Turbulence in Shallow Coastal Shelves, *J. Phys. Oceanogr.*, *45*(12), 2869–2895, doi:10.1175/JPO-D-14-0158.1, 2015.

Skyllingstad, E. D., and D. W. Denbo, An ocean large-eddy simulation of Langmuir circulations and convection in the surface mixed layer, *J. Geophys. Res.*, *100*(C5), 8501, doi:10.1029/94jc03202, 1995.

Sorbjan, Z., On similarity in the atmospheric boundary layer, *Boundary-Layer Meteorol.*, *34*(4), 377–397, doi:10.1007/BF00120989, 1986.

Sroka, S., and K. Emanuel, A Review of Parameterizations for Enthalpy and Momentum Fluxes from Sea Spray in Tropical Cyclones, *J. Phys. Oceanogr.*, *51*(10), 3053–3069, doi:10.1175/JPO-D-21-0023.1, 2021.

Steffen, E. L., and E. A. D'Asaro, Deep convection in the Labrador Sea as observed by Lagrangian floats, *J. Phys. Oceanogr.*, *32*(2), 475–492, doi:10.1175/1520-0485(2002)032<0475:DCITLS>2.0.CO;2, 2002.

Steffen, E. L., and E. A. D'Asaro, Meso- and Submesoscale Structure of a Convecting Field, *J. Phys. Oceanogr.*, *34*(1), 44–60, doi:10.1175/1520-0485(2004)034<0044:MASSOA>2.0.CO;2, 2004.

Sullivan, P. P., and J. C. McWilliams, Dynamics of Winds and Currents Coupled to Surface Waves, *Annu. Rev. Fluid Mech.*, *42*(1), 19–42, doi:10.1146/annurev-fluid-121108-145541, 2010.

Sullivan, P. P., J. C. McWilliams, and W. K. Melville, Surface gravity wave effects in the oceanic boundary layer: large-eddy simulation with vortex force and stochastic breakers, *J. Fluid Mech.*, *593*, 405–452, doi:10.1017/S002211200700897X, 2007.

Sullivan, P. P., L. Romero, J. C. Mcwilliams, and W. Kendall Melville, Transient Evolution of Langmuir Turbulence in Ocean Boundary Layers Driven by Hurricane Winds and Waves, *J. Phys. Oceanogr.*, *42*(11), 1959–1980, doi:10.1175/JPO-D-12-025.1, 2012.

Suzuki, N., and B. Fox-Kemper, Understanding Stokes forces in the wave-averaged equations, *J. Geophys. Res. Ocean.*, *121*(5), 3579–3596, doi:10.1002/2015JC011566, 2016.

Taylor, G., Eddy motion in the atmosphere, *Philos. Trans. R. Soc. London*, *215*(523-537), 1–26, doi:10.1098/rsta.1915.0001, 1915.

Tejada-Martínez, A. E., and C. E. Grosch, Langmuir turbulence in shallow water. Part 2. Large-eddy simulation, *J. Fluid Mech.*, *576*, 63–108, doi:10.1017/S0022112006004587, 2007.

Terray, E., M. Donelan, Y. Agrawal, W. Drennan, K. Kahma, A. Williams, P. Hwang, and S. Kitaigorodskii, Estimates of Kinetic Energy Dissipation under Breaking Waves, *J. Phys. Oceanogr.*, *26*(5), 792–807, doi:10.1175/1520-0485(1996)026<0792:EOKEDU>2.0.CO;2, 1996.

Thomson, J., Directional wave and sea surface temperature measurements collected in situ by Datawell Waverider buoys located near OCEAN STATION PAPA from 2010/06/16 to 2019/12/14, version 1, accessed 14 Februray 2020, http://cdip.ucsd.edu/themes/cdip?pb=1&u2=s:166:st:1&d2=p70, 2019.

Thorpe, S. A., The effect of Langmuir circulation on the distribution of submerged bubbles caused by breaking wind waves, *J. Fluid Mech.*, *142*(C7), 151–170, doi:10.1017/S0022112084001038, 1984.

Thorpe, S. A., *The Turbulent Ocean*, Cambridge University Press, doi:10.1017/CBO9780511819933, 2005.

Tseng, R.-S., and E. A. D'Asaro, Measurements of Turbulent Vertical Kinetic Energy in the Ocean Mixed Layer from Lagrangian Floats, *J. Phys. Oceanogr.*, *34*(9), 1984–1990, doi:10.1175/1520-0485(2004)034<1984:MOTVKE>2.0.CO;2, 2004.

Van Roekel, L., et al., The KPP Boundary Layer Scheme for the Ocean: Revisiting Its Formulation and Benchmarking One-Dimensional Simulations Relative to LES, *J. Adv. Model. Earth Syst.*, *10*(11), 2647–2685, doi:10.1029/2018MS001336, 2018.

Van Roekel, L. P., B. Fox-Kemper, P. P. Sullivan, P. E. Hamlington, and S. R. Haney, The form and orientation of Langmuir cells for misaligned winds and waves, *J. Geophys. Res. Ocean.*, *117*(5), doi:10.1029/2011JC007516, 2012.

von Kármán, T., Mechanische Ähnlichkeit und Turbulenz, in *Proc. Third Internat. Congr. Appl. Mech.*, vol. 1, pp. 85–93, Stockholm, Sweden, 1931.

Wilson, J. D., Monin-Obukhov Functions for Standard Deviations of Velocity, *Boundary-Layer Meteorol.*, *129*(3), 353–369, doi:10.1007/s10546-008-9319-5, 2008.

Wyngaard, J. C., A Physical Mechanism for the Asymmetry in Top-Down and Bottom-Up Diffusion, *J. Atmos. Sci.*, *44*(7), 1083–1087, doi:10.1175/1520-0469(1987)044<1083:APMFTA>2.0.CO;2, 1987.

Wyngaard, J. C., *Turbulence in the Atmosphere*, 393 pp., Cambridge University Press, 2010.

Wyngaard, J. C., and O. R. Coté, Cospectral similarity in the atmospheric surface layer, *Q. J. R. Meteorol. Soc.*, *98*(417), 590–603, doi:10.1002/qj.49709841708, 1972.

Wyngaard, J. C., O. R. Coté, and Y. Izumi, Local Free Convection, Similarity, and the Budgets of Shear Stress and Heat Flux, *J. Atmos. Sci.*, *28*(7), 1171–1182, doi:10.1175/1520-0469(1971)028<1171:LFCSAT>2.0.CO;2, 1971.

Yang, D., B. Chen, M. Chamecki, and C. Meneveau, Oil plumes and dispersion in Langmuir, upper-ocean turbulence: Large-eddy simulations and K-profile parameterization, *J. Geophys. Res. Ocean.*, *120*(7), 4729–4759, doi:10.1002/2014JC010542, 2015.

Zedel, L., and D. Farmer, Organized structures in subsurface bubble clouds: Langmuir circulation in the open ocean, *J. Geophys. Res.*, *96*(C5), 8889, doi:10.1029/91jc00189, 1991.

Zhang, C., Madden-Julian Oscillation, *Rev. Geophys.*, *43*(2), 1–36, doi:10.1029/2004RG000158, 2005.

Zhou, B., S. Sun, J. Sun, and K. Zhu, The universality of the normalized vertical velocity variance in contrast to the horizontal velocity variance in the convective boundary layer, *J. Atmos. Sci.*, *76*(5), 1437–1456, doi:10.1175/JAS-D-18-0325.1, 2019.

Zhou, X., T. Hara, I. Ginis, E. D'asaro, J. Y. Hsu, and B. G. Reichl, Drag Coefficient and Its Sea State Dependence under Tropical Cyclones, *J. Phys. Oceanogr.*, *52*(7), 1447–1470, doi:10.1175/JPO-D-21-0246.1, 2022.

Zippel, S. F., J. Thomson, and G. Farquharson, Turbulence from breaking surface waves at a River mouth, *J. Phys. Oceanogr.*, *48*(2), 435–453, doi:10.1175/jpo-d-17-0122.1, 2018.